# Compatible Finite Elements for Wave and Fluid Models: Application to Plasma Physics

Mustafa Gaja

**Technische Universität München**

FAKULTÄT FÜR MATHEMATIK

LEHRSTUHL FÜR NUMERISCHEN METHODEN DER
PLASMAPHYSIK

**Max Planck Institut für Plasmaphysik**

# Compatible Finite Elements for Wave and Fluid Models: Application to Plasma Physics

**Mustafa Gaja**

Vollständiger Abdruck der von der Fakultät für Mathematik der Technischen Universität München zur Erlangung des akademischen Grades eines

**Doktors der Naturwissenschaften (dr. rer. nat.)**

GENEHMIGTEN DISSERTATION.

*Vorsitzender:*             Prof. Dr. Daniel Matthes

*Prüfende der Dissertation:*    1. Prof. Dr. Eric Sonnendrücker

                               2. Prof. Dr. Philippe Helluy

*Die Dissertation wurde am 13.11.2019 bei der Technischen Universität München eingereicht und durch die Fakultät für Mathematik am 29.01.2020 angenommen*

**Max Planck Institut für Plasmaphysik**

Abteilung Numerischen Methoden der Plasmaphysik

Technische Universität München

# Compatible Finite Elements for Wave and Fluid Models: Application to Plasma Physics

*Author:*  Mustafa Gaja

*Supervisor:*  Prof. Dr. Eric Sonnendrücker

*Advisor:*  Dr. Emmanuel Franck

# Abstract

Magnetohydrodynamic models are pivotal to fusion plasmas and accurate numerical schemes are needed in order to ensure the preservation of fundamental physical laws like the energy conservation and the divergence-free condition. In this work, we explore using compatible discretizations for linear MHD with an energy-preserving splitting. The work elaborates on devising an ad-hoc preconditioner through the theory of Generalized Locally Toeplitz Matrices applied to elliptic problems.

# Zusammenfassung

Zentraler Bestandteil in der physikalischen Beschreibung von Fusionsplasmen sind magnetohydrodynamische Modelle. Die Genauigkeit der numerischen Lösungsverfahren garantiert hierbei die Wahrung physikalischer Gesetzmäßigkeiten wie Energieerhaltung und Divergenzfreiheit. In dieser Arbeit untersuchen wir kompatible Diskretisierungen für lineare Magnetohydrodynamik mit energieerhaltender Aufteilung. Über die Theorie generalisierter lokaler Toeplitz Matrizen leiten wir einen ad-hoc preconditioner her, welcher auf elliptische Differentialgleichungsprobleme angewandt wird.

# Acknowledgements

First and foremost, I would like to thank my supervisor, Eric Sonnendrücker for giving me the opportunity to conduct this work and provide such an environment that allowed me to explore this research field. I am thankful for the open door policy where I felt comfortable knocking at his door with any scientific questions and concerns that I have when I felt that things were not working well. The opportunity that was offered to me was not confined only to conducting my work just within the office, but I was able to go to a number of conferences and research visits abroad that gave me the chance to obtain a wider appreciation of how research is conducted in different environments. I am also very grateful for the numerous times that Eric has read the thesis and all the support that he provided while writing in order to reach this stage.

There are a large number of people that were pivotal for my work in these past four year; I would like to thank Anneliese Grassmann for helping to ease-up anything to do with the bureaucracy, Ahmed Ratnani for providing the Jorek-Django framework that this work has been built on, Jalal Lakhlili for never being short in giving me support for the first two years with anything to do with Django or software development in general, Mariarossa Mazza for explaining the GLT theory to me, Florian for listening and his precious advises. Thank you Laura for taking the time and the effort to help me with a coding phase that was crucial for this work.

If I were to mention one person without whom this work would not have been possible, it would be my advisor, Emmanuel Franck. I am forever thankful for having him standing on my side when things were not working out, for the support that he offered and for his constant availability despite being in different countries, even when he was on holidays to make sure that I was progressing with my work. I wish you all the best for your research career that I am sure would be nothing less of a stellar one.

# Contents

# List of Figures

# *Dedication*

There are so many people who touched my life in these last 4 years, and I wont be able to include everyone here, but if I were to give it a shot, then I would like to thank my fellow PhD students and support group: Eduardo, Anna, Lorenzo and Camilla, with whom I shared this journey with its downs and hmm downs.

Thank you Eduardo for being my companion in the last months of writing, those long days at the library will not be forgotten; the bitte schön, the daily Cesar salad, the confusion, the complaining and the autistic conversations, I do not know how I would have endured those months without sharing the path with you.

Lorenzo, you have been my partner in crime from day one, I will be missing our 10:30 espresso-fredo, the endless and sometimes, pointless lunch discussions that spills over to further coffee breaks. Thank you for being my friend and showing support when needed and for your honesty even when it is not what I wanted to hear. I am grateful to have shared those years with you and looking forward to more years to come in our new home town, Munich.

Thank you Ala for always having open ears and being available to hear my rants, for the caring that you show and never being short of advises. For Emma and Gagan, my Improv soul mates, with whom I managed to regain my forgotten silly side and to be me again. To my little brother, Gagan, who pushed me to get on the stage and made me discover the joys of performing and introducing me to Stand Up Comedy. I am forever grateful for this joy that you brought into my life and cannot wait to see how we grow together as comedians. Thank you Laura for listening and offering your experience when the times were difficult.

To my two strong pillars in life, Mohammed and Rzoga, despite us, as we predicted 7 years ago, living in three different continents, you are still the two people that I escape to when I need to vent and elevate my mood. Thank you for being there and always saying the right things.

To Jagata for entering the scene and shifting everything to the background, it made everything lighter and more beautiful. Thank you.

I guess it wont be me without dedicating this work also to myself. There were so many defining moments and memories in these past four years. If I were to pick one, that will be engraved in my mind, is that I was checking for the bold symbols and the dot products in my manuscript while my sister was packing the bags and going with my nephews to my parents place for fear of bombardment. The dichotomy of that moment, hunted me for most of the months of writing and shed a light on how helpless one could be faced with the realities of life.

إلى أحلى أب و أم يمكن لأحد أن يتخيل. إلى بابا من وفر لي كل ما احتجت له لكي ادرس و أعطاني وسعة الحرية في خياراتي من دون ضغوط و أعطاني القدرة على أن اؤمن في نفسي. إلى ماما من أعطتني القيود المنيعة في صغري حتى طورت أجنحتي الطليقة، من أعطتني المجال لأجرب و اؤمن بأحلامي. إلى أخي الكبير لواء، الذي أعطاني الخيال والذي أعرف أنه في جانبي لاى شيء كبير في حياتي. إلي أختي و صديقتي لمياء، الجاهزة دائما لحمايتي من نسمة الريح و من تحبني من دون قيود. أحبكم حبا لا غطاء له، لكم جزيل شكري إلى ما وفرتم إلي لكي أصل إلى هنا. مشتاق دائما.

إلي القرود الصغيرة، علي، امو، لوكي، محمود و عبدو. أتمنى لكم السعادة و الهناء و راحة البال ما حييتم، لا خوف عليكم و و أنتم تحت يدي لمياء و لواء. أحبكم و أفكر فيكم.

And at the end, this is for the one and only, the one who gave without expecting a return, who made everything possible and protected me from breezes. The one who taught me how to live and be alive regardless of the circumstances, how to get joy with what you have and create life with the little things, who engraved in me the belief that everything will be OK at some point. This is to you.

# Chapter 1

# Physical and Mathematical Context

## 1.1 Physical Introduction

It is expected that in the coming decades, more demand for energy cannot be avoided. Considering that the world population nowadays is 7 billion people with a daily energy consumption that is more than a million terajoules [43], we can only imagine how this daily consumption will be growing given that it is projected that the world population would reach 10 billion people by 2050, see Fig. (1.1). Not forgetting the rapid urbanization taking place and the increase in standards of living in fast growing parts of the developing world, large scale electricity generation will be required.
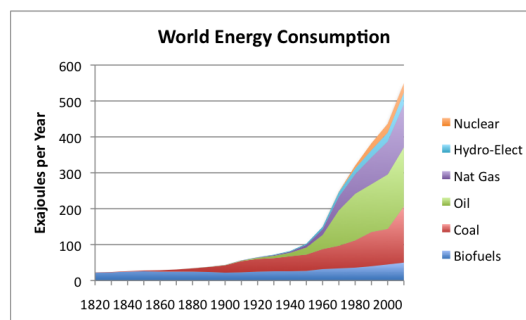


FIGURE 1.1: World energy consumption through time. *Source: Finland Futures Research Center*

From an environmental point of view, the increase in carbon dioxide emissions correlates with the increase in the average temperature of the globe, which could lead to catastrophic effects on the environment [7]. That said, even if we find ways

1

to limit the climate change in terms of using more energy efficient mechanisms and being more conscious about our influence on the environment, we will also need to find sustainable energy sources that could fulfill the ever increasing world demand of energy [50]. **Plasma fusion** offers such a possibility as a clean and infinite source of energy that is comparatively safe. For more details on this argument, please refer to [50] as it offers not only a qualitative argument for the case of fusion energy, but also a quantitative one.

Scientists have been inspired by the inner workings of the sun. **Fusion** is the process which powers the sun and the stars. The process requires very high temperatures in order to 'fuse' two light atoms, such as hydrogen. In the case of the sun this temperature is up to 15 million °C. At these high temperatures, matter turns into **plasma**. The sun is made of hydrogen plasma, which is considered to be the fourth state of matter along with solid, liquid and gas.

**Plasma** can be described as a 'soup' of electrically charged particles. The separation between the positively charged ions and the negatively charged electrons is so strong, such that the collective behaviour of the interactions within the whole ensemble overshadows that of the interactions between the individual particles [19]. Plasma is rarely found naturally on earth, that said, it is estimated that more than 99% of the matter in the universe is made of plasma, see Fig. (1.2).



FIGURE 1.2: Examples of plasma in nature: Left: Thunder, which is in the state of plasma. Right: The Sun, which is made up of plasma. *Source: Wikipedia*

Fusion reactions as a physical process is not a new discovery, the first fusion reaction on earth was carried out in 1951. The question is how we can utilize these reactions such that we can generate energy for our purposes.

The most probable fusion reaction is the **Deuterium-Tritium (D-T)** reaction [5] as can be seen in Fig. (1.3). Deuterium can be extracted from water, whereas Tritium is produced during the fusion process. The result of the reaction is a helium nucleus that has an energy of 3.56 MeV and a neutron with an energy of

14.03 MeV. The reason why the D-T reaction is chosen by the fusion community, is due to the fact that the reaction rate of D-T is larger than the rate of other possible fusion reactions, see Fig. (1.4).
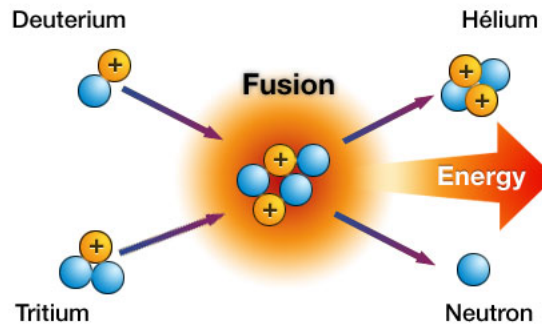


FIGURE 1.3: Deuterium-Tritium fusion reaction. *Source: Stanford University.*

However, the diagram presented in Fig. (1.4) shows that the D-T matter has to be heated up to 10 keV ($\approx$ 100 million degrees) to make this reaction probable. The reason is because the two nuclei are positively charged and hence have to overcome the repulsive Coulomb barrier before fusing. This could be achieved if the ions collide with each other with a high enough energy, that is why such high temperatures are needed at this stage.
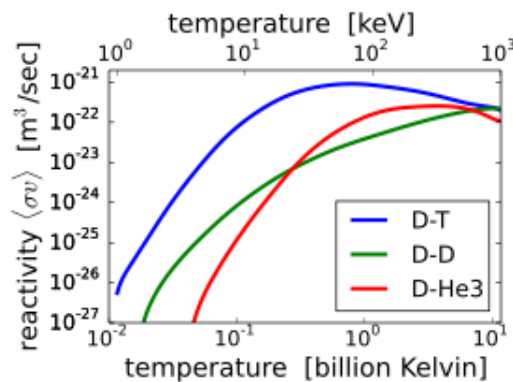


FIGURE 1.4: Reactivities for different fusion reactions. *Source: Wikipedia.*

In principle, the idea is simple, but the question poses itself to how could we have such high temperatures in order to produce and sustain a plasma without having an interaction with the surroundings which would lead to a drop in the temperatures and hence to the halting of the fusion reactions? The idea is to use

the fact that the plasma is a mixture of charged particles and try to confine it by using the electrical conductivity of the plasma to contain it with magnetic fields. This resulted in what is known as **Magnetic Confinement Fusion** [54], where magnetic fields are used to trap the charged particles, and keeping them away from the container. The basic concept can be thought of in terms of individual particles spiralling along magnetic field lines. **Magnetic confinement** is one of two major branches of fusion energy research, the other being **inertial confinement fusion** [15]. The magnetic approach has seen the majority of development whereas inertial confinement fusion is less favourable for research due to its potential intersectionality with weapons research. Magnetic confinement fusion is also usually considered more promising for practical power production. Currently, there are two ways to realize magnetic fusion confinement: **Tokamaks and Stellarators**. Tokamaks, a Russian word for a torus shaped magnetic chamber, is based on the idea that the magnetic fields used to confine the plasma are partly produced by external coils, and partly by the plasma current [53]. Whereas for Stellarators, the magnetic field is solely produced externally by coils [63]. A schematic view of Tokamaks and Stellarators can be seen in Fig. (1.5).
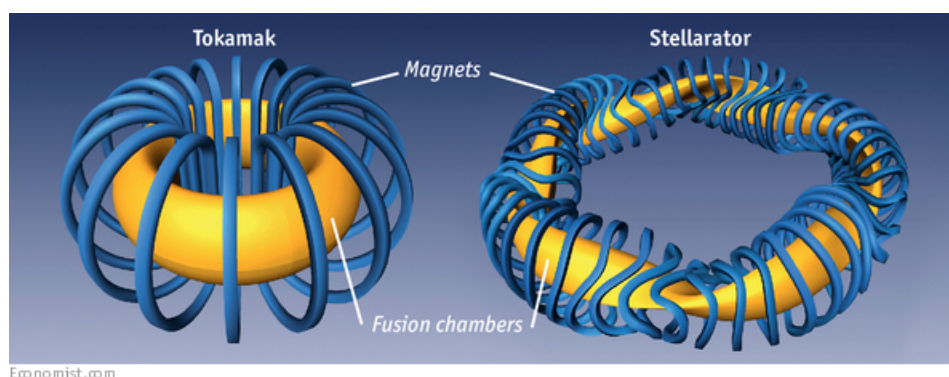


FIGURE 1.5: Schematic view: Tokamaks vs. Stellarators. *Source: The Economist.*

Tokamaks rely on strong magnetic coils that produces powerful magnetic fields in order to confine the plasma in the shape of a torus. The idea of Tokamaks came during the 1950s and is pioneered by soviet physicists Igor Tamm and Andrei Sakharov. In 1997, scientists at the Joint European Torus (JET) facilities in the UK produced 16 megawatts of fusion power. An important concept that guided the development of different Tokamaks is what is called the fusion energy gain factor **Q**. Which is basically the ratio of the output power to the input power. In this regard, the obtained fusion gain factor for JET in 1997 was **Q** = 0.63.

**ITER (International Thermonuclear Experimental Reactor)** is an international nuclear fusion research and engineering project, which upon completion, will be the largest magnetic confinement fusion plasma experiment in the world. ITER is designed as such to have a thermal output power of 500 MW while 50 MW of thermal power is supplied to the Tokamak, which translates to $\mathbf{Q} = 10$. As $\mathbf{Q} > 1$, this means that ITER aims to produce more energy than that supplied, making it the first fusion experiment to do so in the world [45]. The project is financed and administered by the EU, India, China, South Korea, Japan and the United States. A schematic diagram of ITER could be seen in Fig. (1.6).
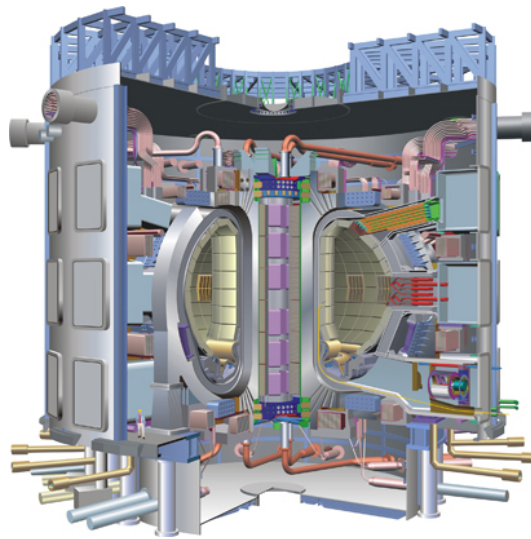


FIGURE 1.6: Schematic diagram of ITER. *Source: IPP.*

The goal of ITER is to demonstrate the scientific and technological feasibility of fusion energy and not to actually produce energy that could be utilized.

## 1.2   Mathematical Introduction

During the operation of fusion devices, it is common to experience the onset of disruptive instabilities [55][68] that are deemed detrimental to the confinement vessel. Such situations call for physical modelling to try to understand the underlying phenomena that give rise to such events and devise a way to avoid them in future scenarios. In this context, the Magnetohydrodynamic (MHD) model is used to predict such operational limits in fusion devices. The MHD model is a system of coupled partial differential equations (PDEs) that cannot be solved analytically except for a few simple limits that do not serve the purpose of predicting

the disruptive instabilities. For that purpose, numerical simulations offer a solution to this problem. Numerical algorithms for the solution of partial differential equations are an essential tool of the design of aircrafts, prediction of climate and a tool to understand the physical world around us. Given a PDE problem, a numerical algorithm approximates the solution by the solution of a finite dimensional problem which can be implemented and solved on a computer. The main discretization schemes are Finite Difference (FD), Finite Volume (FV) and Finite Element Methods (FEM), for an extensive introduction on discretization methods, one can refer to [57]. In this work, we are concerned with the FEM. Although FEM has a myriad of applications and is successful across many fields, in certain cases, the classical choice of the subspaces where the test and trial functions live in could lead to undesirable approximation and stability properties. A newly developed theory, Finite Element Exterior Calculus aims at finding finite element approximations with good approximation properties, which provide structure-preserving discretizations that lead to holding fundamental physical invariants like the energy preservation or the preservation of $\operatorname{div} \operatorname{curl} = 0$ and $\operatorname{curl} \operatorname{grad} = 0$ at the discrete level.

## 1.3    Structure of the Manuscript

Chapter (2) introduces the main mathematical and numerical tools which are used in the implementation of the numerical schemes carried out in this manuscript; starting with an introduction to FEM and then we give the definition of B-splines and their properties and how they are used in the context of Isogeometric Analysis (IgA). The chapter ends with a discussion on compatible discretizations and introduces the de Rham sequences in 2D. In Chapter (3), we derive the linear MHD model in the context of Tokamaks and introduce a three step energy preserving splitting. We detail each step; the acoustic step, the magnetic step and the convection-diffusion step in terms of the choice of compatible discretizations and the associated numerical results. We end the chapter with two test cases for the linear MHD, considering the three steps splitting. In Chapter (4) we introduce the Generalized Locally Toeplitz (GLT) theory and we devise an ad-hoc preconditioner applied to elliptic problems and use the GLT theory as a spectral analysis tool applied to the anisotropic diffusion problem. We end the manuscript with Chapter (4.7), where we draw conclusions and discuss future perspectives.

# Chapter 2

# Mathematical and Numerical Background

In this chapter, we give various mathematical definitions and introduce concepts which are used later on in this work. We start by including a short introduction to FEM and give a brief overview of B-splines, and subsequently how to construct B-spline curves and surfaces. After that, we introduce the technique known as IgA based on B-splines, and how in turn IgA is different from classical FEM. Then we move to speaking about compatible discretizations where we present some spaces that will be necessary in order to introduce our discretization techniques, which culminates by presenting the commuting de Rham sequences in 2D. We end the chapter by presenting Maxwell's equations in 2D and include relevant results to solving Maxwell's equations and the usage of the de Rham sequence and commuting projections.

## 2.1 Finite Element Method

The finite element method is based on what is called weak or variational formulation, where a boundary value problem is not required to hold absolutely, but rather its integral with respect to certain test functions in some function space. The weak formulation is reduced then to a finite dimensional problem defined on a subspace of the original function space. For a detailed introduction to FEM, one can refer to [33][47]. As an example, if we let $V$ be a Banach space, we consider deriving the weak formulation for Poisson's equation:

$$-\nabla^2 u = f, \quad \Omega \subset \mathbb{R}^d$$

with $u = 0$ on the boundary $\partial\Omega$, where $u \in V$ and so we take $V = H_0^1(\Omega)$. We define the $L^2$ scalar product:

$$(u, v) = \int_\Omega uv dx.$$

Then, multiplying by a test function $v \in V$, we get

$$-\int_\Omega (\nabla^2 u) v dx = \int_\Omega f v dx.$$

We integrate the left hand side by parts using Green's identity and assuming that $v = 0$ on $\partial\Omega$: $\int_\Omega \nabla u \cdot \nabla v dx = \int_\Omega f v dx$. We obtain the generic form by assigning:

$$a(u, v) = \int_\Omega \nabla u \cdot \nabla v dx, \quad and \quad f(v) = \int_\Omega f v dx$$

Hence, the weak formulation reads: Find $u \in V$, such that:

$$a(u, v) = f(v), \quad \forall v \in V.$$

To discretize, we replace the infinite dimensional linear problem with a finite dimensional version. Find $u_h \in V_h$, such that:

$$a(u_h, v_h) = f(v_h), \quad \forall v_h \in V_h \subset V$$

and we choose $V_h$ to be a space of piecewise polynomial functions. We identify a basis for $V_h$ considering that the space consists of continuous piecewise affine functions which are zero on the boundary. Let $\phi^h$ be a continuous piecewise affine function. The set of functions $\{\phi_i^h : i = 1, \ldots, N\}$ forms a basis for $V_h$. The discrete equation can now be written explicitly as:

Find $u_h = \sum_{j=1}^N u_j^h \phi_j^h$ such that:

$$a(u_h, \phi_i^h) = F(\phi_i^h), \quad \forall i = 1, \cdots, N.$$

Where $\{\phi_i^h : i = 1, \ldots, N\}$ are the set of test functions. This leads to the following system of equations for the coefficients $u_j^h$:

$$\sum_{j=1}^N a(\phi_j^h, \phi_i^h) u_j^h = F(\phi_i^h), \quad \forall i = 1, \cdots, N.$$

If we define an $N \times N$ matrix $A^h$ via:

$$A^h_{ij} = a(\phi^h_j, \phi^h_i)$$

and vectors $\boldsymbol{U}^h = (u^h_1, \cdots, u^h_N)^T$ and $\boldsymbol{F}^h = (F(\phi^h_1), \cdots, F(\phi^h_N))^T$, then the discrete equation is equivalent to the linear system:

$$A^h \boldsymbol{U}^h = \boldsymbol{F}^h.$$

Solving this linear system results in determining the coefficients of $u_h$ in the basis $\{\phi^k_i\}$, which in turn allows the representation of the unknown field. In this work, we will construct a variant of FEM based on B-splines which has some interesting properties that will become apparent in what follows. We start by providing a brief overview of B-splines that is intended to fix the notation and present the main definitions. We rely on the material presented in [65].

**Definition 2.1** (B-spline Series)**.** To create a family of B-splines, we need a non-decreasing sequence of knots $T = (t_i)_{1 \leqslant i \leqslant N+k}$, also called a knot vector, with $k = p + 1$. Each set of knots $T_j = \{t_j, \cdots, t_{j+p}\}$ will generate a B-spline $N_j$. The j-th B-spline of order $k$ is defined by the recurrence relation:

$$N^k_j = w^k_j N^{k-1}_j + (1 - w^k_{j+1}) N^{k-1}_{j+1}$$

where

$$w^k_j(x) = \frac{x - t_j}{t_{j+k-1} - t_j} \qquad\qquad N^1_j(x) = \chi_{[t_j, t_{j+1}[}(x)$$

for $k \geq 1$ and $1 \leq j \leq N$.

B-splines can be evaluated quickly as they consist of polynomials and they are flexible, because of their piecewise definition. Furthermore, the continuity of the function can be prescribed. Fig. (2.1) shows an example of such B-splines.
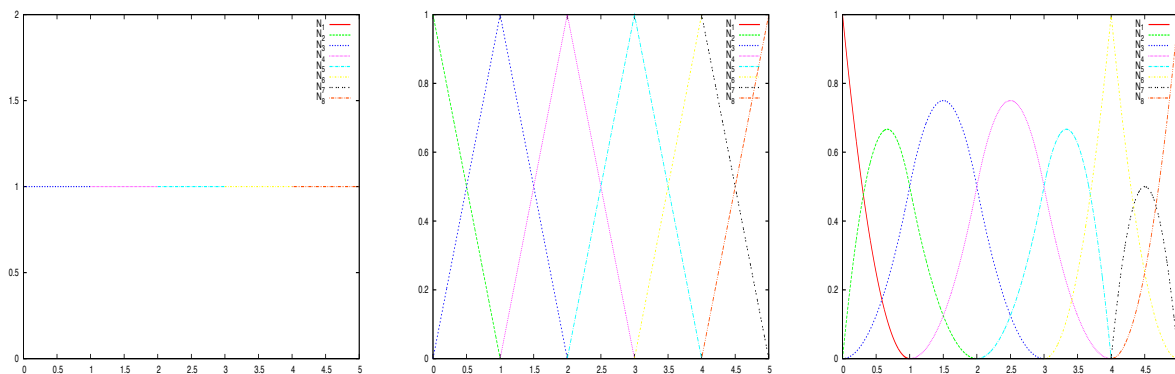
FIGURE 2.1: B-splines functions associated to the knot vector $T = \{000\ 1\ 2\ 3\ 44\ 555\}$, of order $k = 1, 2, 3$

We note some important properties of B-splines:

- B-splines are piecewise polynomials of degree $p = k - 1$,

- When $n = k$, B-splines are exactly the Bernstein polynomials,

- Compact support; the support of $N_j^k$ is contained in $[t_j, t_{j+k}]$,

- If $x \in ]t_j, t_{j+1}[$, then only the *B-splines* $\{N_{j-k+1}^k, \cdots, N_j^k\}$ are non vanishing at $x$,

- Positivity: $\forall j \in \{1, \cdots, n\}\ \ N_j(x) > 0, \ \ \forall x \in ]t_j, t_{j+k}[$,

- Partition of unity : $\sum_{i=0}^{n-1} N_i^k(x) = 1, \forall x \in \mathbb{R}$,

- Local linear independence,

- $\forall i, \ p + 1 \le i \le m - p$, the regularity of the B-spline is $\mathcal{C}^{(p-1)}$ at $t_i$,

- Interpolation: $N_1(a) = 1$ and $N_n(b) = 1$.

- The B-spline derivative is given by:

$$\frac{dN_i^p}{dx} = p\left(\frac{N_i^{p-1}(x)}{t_{i+p} - t_i} - \frac{N_{i+1}^{p-1}(x)}{t_{i+p+1} - t_{i+1}}\right).$$

Relying on the previous definition of B-spline series, we extend the definition to B-spline curves which have the ability to interpolate or approximate a set of given data points.

**Definition 2.2** (B-spline curve)**.** The B-spline curve in $\mathbb{R}^d$ associated to knot vector $T = (t_i)_{1 \leq i \leq N+k}$ and control points $(P_i)_{1 \leq i \leq N}$ is defined by:

$$C(t) = \sum_{i=1}^{N} N_i^k(t) P_i$$

We have the following properties for a B-spline curve:

- If $N = k$, then C is just a Bezier-curve,

- C is a piecewise polynomial curve,

- The curve interpolates its extremes if the associated multiplicity of the first and the last knots are maximum,

- Invariance with respect to affine transformations,

- Local modification: moving $\mathbf{P}_i$ affects C(t), only in the interval $[t_i, t_{i+k}]$,

- The control polygon approaches the behavior of the curve.

The surface analogue of the B-spline curve is the B-spline surface.

**Definition 2.3** (B-spline surface)**.** The B-spline surface of order k associated to the knot vectors $\{T^{(1)}, T^{(2)}\}$ and the control points $(\mathbf{P}_{i,j})_{1 \leq i \leq N_1, 1 \leq j \leq N_2}$, is defined by

$$\mathbf{M}(t^{(1)}, t^{(2)}) = \sum_{i=1}^{N_1} \sum_{j=1}^{N_2} N_{i,j}(t^{(1)}, t^{(2)}) \mathbf{P}_{i,j},$$

with $N_{i,j}(t^{(1)}, t^{(2)}) = N_i^{(1)}(t^{(1)}) N_j^{(2)}(t^{(2)})$.

B-splines functions, curves and surfaces enable the creation and management of complex shapes and geometries which have various applications such as in computer aided design.

## 2.2 Isogeometric Analysis

Is a novel methodology for the discretization of PDEs. It was introduced by T. Hughes and co-authors in [44]. It is designed to improve the connection between numerical simulations of physical phenomena and computer aided design systems. The goal is to reduce the approximation of the computational domain by using an exact geometry directly on the coarsest level of discretization. This is achieved

via the usage of B-splines or Non Uniform Rational B-splines (NURBS) for the geometry description as well as the representation of the unknown fields. Beside the fact that one can treat efficiently very general geometries by B-splines and NURBS parametrizations, these functions are very interesting since they easily allow for a high order smoothness, as can be seen in [36] [30] [8] [4].
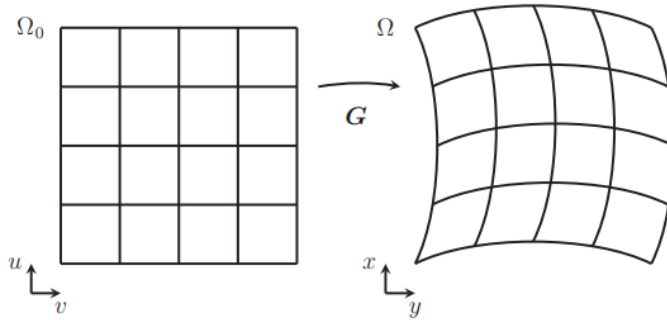


FIGURE 2.2:  Geometry mapping between the parameter and physical domains.

Therefore, our point of departure is a spline parameterization:

$$\boldsymbol{G} : \Omega_0 \longrightarrow \Omega, \quad \boldsymbol{G}(\boldsymbol{u}) = \sum_i N_i(\boldsymbol{u})\boldsymbol{P}_i, \qquad (2.2.1)$$

with control points $\boldsymbol{P}_i$ and with respect to a basis $N_i$, which maps from the parametric space $\Omega_0$ onto the computational domain $\Omega$. The basic idea is to formulate the finite dimensional variational formulation:

$$a(u_h, v_h) = (l_h, v_h) \quad \forall v_h \in V_h,$$

with respect to basis functions defined on the parameter domain $\Omega_0$ and to use the geometry mapping $\boldsymbol{G}$ from Eq. (2.2.1) as a global push-forward operator to map these functions to the physical domain $\Omega$. We can identify the following main components:

- a set of basis functions $N_k$,

- an isogeometric mesh $\mathcal{T}$,

- a geometric mapping $\boldsymbol{G} : \Omega_0 \longrightarrow \Omega$.

The most obvious difference between isogeometric analysis and FEM is the choice of the basis functions. Instead of Lagrange or Hermite polynomials we employ B-splines or NURBS which are the same as those used to define $\boldsymbol{G}$. One can see that

the advantages of using this approach are numerous: IgA allows the description of complex geometry without an introduction of approximation error, which is quite different to the classical triangular mesh approach. We also note that the regularity of the basis functions can be elevated easily via increasing the B-spline degree.

## 2.3 Compatible Discretizations

In this section we quote the key concepts that we will be using for the purposes of the numerical implementation conducted in this work. These results are obtained from literature aiming at having a fundamental understanding for pivotal mathematical structures which lays the foundations to achieve a good approximation for the MHD model at the discrete level.

Compatible FE discretizations are a fundamental tool for devising structure-preserving discretizations [40][41][39], where a unifying framework is proposed. After that, many authors have underlined the central role of the de Rham diagram and its discrete version for the successful derivation of solvers based on compatible FEs. For having a better understanding of discrete de Rham sequence based on B-splines, check [14]. The general theory of Finite Element Exterior Calculus (FEEC) for general applications was presented by Arnold, Falk and Whinter in [2]. Although the formulation in this work could be written in the context of differential forms as is the case in [1][40] for FE approximations, we refrain from following this line and maintain a classical approach as is the case in [52].

Defining $rot\boldsymbol{F} = -\partial_y F_x + \partial_x F_y$ and $\nabla F = (\partial_x F, \ \partial_y F)^T$, for any function $w \in H^1(\Omega)$ it holds that $rot \ (\nabla w) = -\partial_y \partial_x w + \partial_x \partial_y w = 0$, thus it is clear that $\nabla w \in H(rot; \Omega)$. Moreover, since the domain $\Omega$ is simply connected, we also know that the range of the gradient operator is equal to the kernel of the rot operator, namely $Im(\nabla) = ker(rot)$. Let $\Omega \in \mathbb{R}^2$ be a bounded Lipschitz domain, we define the following Sobolev spaces:

$$H^1(\Omega) = \{v \in L^2(\Omega); \nabla v \in (L^2(\Omega))^2\}$$

$$H(rot, \Omega) = \{\boldsymbol{v} \in (L^2(\Omega))^2; rot\boldsymbol{v} \in L^2(\Omega)\}$$

$$H(div, \Omega) = \{\boldsymbol{u} \in (L^2(\Omega))^2; \nabla \cdot \boldsymbol{u} \in L^2(\Omega)\}$$

$$L^2(\Omega) = \{f : \mathbb{R} \to \Omega, \int_\Omega f^2 < \infty\},$$

The previous points are summarized in the following de Rham diagram:

de Rham Sequence 1

$$\mathbb{R} \quad \xrightarrow{\phantom{xx}} \quad H^1(\Omega) \quad \xrightarrow{\nabla} \quad H(rot, \Omega) \quad \xrightarrow{rot} \quad L^2(\Omega) \quad \xrightarrow{\phantom{xx}} 0$$

In order to discretize continuous problems where the variable fields belong to the above mentioned Sobolev spaces, it is indispensable to construct finite dimensional spaces $V_0 \subset H^1(\Omega)$, $V_1 \subset H(rot;\Omega)$ and $V_3 \subset L^2(\Omega)$ maintaining the same relationships of the continuous spaces given (we reserve the space designation $V_2$ for the finite dimensional space belonging to $H(div;\Omega)$, as will become clear later on). The first step is to construct suitable discretizations of the spaces. We note that the space of B-splines in 1D spanned by the basis functions $N_i^p$ will be denoted by $S^p := span\{N_i^p\}_{i=1}^n$. The definition of the B-splines space is extended easily to 2D in the following manner. Let us associate to the two knot vectors $T^1$ and $T^2$, the p-degree univariate B-splines basis functions $N_i^{p_1}$ and $N_j^{p_2}$, then we define the tensor product B-spline basis functions as:

$$N_{ij}^{p_1 p_2}(x,y) := N_i^{p_1}(x) N_j^{p_2}(y), \quad i = 1, \ldots, N_x, \quad j = 1, \ldots, N_y.$$

Then the tensor product B-spline space is defined as the space spanned by these basis functions, namely:

$$S^{p_1, p_2} := S^{p_1} \otimes S^{p_2} = span\{N_{ij}^{p_1, p_2}\}_{i=1, j=1}^{N_x, N_y}.$$

We recall that the derivatives of functions in $S_\alpha^p$ are splines as well:

$$\frac{d}{dx} v : v \in S^p \equiv S^{p-1}.$$

It follows that the gradient of a function living in $\mathcal{S}^{p,p}$ belongs to $\begin{pmatrix} \mathcal{S}^{p-1,p} \\ \mathcal{S}^{p,p-1} \end{pmatrix}$ and the rot of fields living in this last space belong to $\mathcal{S}^{p-1,p-1}$. We denote by:

$$\psi_{i,j}^0 = N_i^p(x) N_j^p(y)$$

$$\boldsymbol{\psi}_{i,j}^{1,1} = \begin{pmatrix} N_i^{p-1}(x) N_j^p(y) \\ 0 \end{pmatrix}, \quad \boldsymbol{\psi}_{i,j}^{1,2} = \begin{pmatrix} 0 \\ N_i^p(x) N_j^{p-1}(y) \end{pmatrix}$$

$$\psi_{i,j}^3 = N_i^{p-1}(x)N_j^{p-1}(y)$$

And hence the discrete spaces are defined in the following way:

$$V_0 = span\{\psi_{i,j}^0, \ 1 \le i \le N_x, \ 1 \le j \le N_y\}$$

$$V_1 = span\{\boldsymbol{\psi}_{i,j}^{1,1}, \boldsymbol{\psi}_{i,j}^{1,2}, \ 1 \le i \le N_x, \ 1 \le j \le N_y\}$$

$$V_3 = span\{\psi_{i,j}^3, \ 1 \le i \le N_x, \ 1 \le j \le N_y\}$$

The above mentioned discrete spaces verify the same exact properties as the spaces they approximate [13]. For instance, taking the gradient of the basis functions defined on $V_0$ leads to:

$$\nabla\psi_{i,j}^0 = \nabla(N_i^p(x)N_j^p(y)) = \begin{pmatrix} \alpha N_i^{p-1}(x)N_j^p(y) - \beta N_{i+1}^{p-1}(x)N_j^p(y) \\ \alpha N_i^p(x)N_j^{p-1}(y) - \beta N_i^p(x)N_{j+1}^{p-1}(y) \end{pmatrix}$$
$$= \begin{pmatrix} \alpha\boldsymbol{\psi}_{i,j}^{1,1} - \beta\boldsymbol{\psi}_{i+1,j}^{1,1} \\ \alpha\boldsymbol{\psi}_{i,j}^{1,2} - \beta\boldsymbol{\psi}_{i,j+1}^{1,2} \end{pmatrix} \subset V_1$$

which are basically the basis functions that define the $V_1$ space, where $\alpha = \frac{p}{t_{i+p}-t_i}$ and $\beta = \frac{p}{t_{i+p+1}-t_{i+1}}$, assuming the same knot vector for each direction. Taking the rot of these basis functions leads to:

$$rot(\nabla\psi_{i,j}^0) = -\partial_y(\alpha N_i^{p-1}(x)N_j^p(y) - \beta N_{i+1}^{p-1}(x)N_j^p(y))$$
$$+ \partial_x(\alpha N_i^p(x)N_j^{p-1}(y) - \beta N_i^p(x)N_{j+1}^{p-1}(y))$$

$$rot(\nabla\psi_{i,j}^0) = -\alpha(\alpha N_i^{p-1}(x)N_j^{p-1}(y) - \beta N_i^{p-1}(x)N_{j+1}^{p-1}(y))$$
$$+ \beta(\alpha N_{i+1}^{p-1}(x)N_j^{p-1}(y) - \beta N_{i+1}^{p-1}(x)N_{j+1}^{p-1}(y))$$
$$+ \alpha(\alpha N_i^{p-1}(x)N_j^{p-1}(y) - \beta N_{i+1}^{p-1}(x)N_j^{p-1}(y))$$
$$- \beta(\alpha N_i^{p-1}(x)N_{j+1}^{p-1}(y) - \beta N_{i+1}^{p-1}(x)N_{j+1}^{p-1}(y))$$

$$rot(\nabla\psi_{i,j}^0) = -\alpha(\alpha\psi_{i,j}^3 - \beta\psi_{i+1,j}^3) + \beta(\alpha\psi_{i,j+1}^3 - \beta\psi_{i+1,j+1}^3)$$
$$+ \alpha(\alpha\psi_{i,j}^3 - \beta\psi_{i+1,j}^3) - \beta(\alpha\psi_{i,j+1}^3 - \beta\psi_{i+1,j+1}^3) = 0$$

which confirms that $rot(\nabla) = 0$ at the discrete level as in the continuous level. At this point, we define the multi-index $\boldsymbol{i} = \{i_1, i_2\}$ and introduce a single index notation for the basis functions defined on $V_0$, $V_1$ and $V_3$, which we will be using

later on:

$$\phi_{\boldsymbol{i}}^0 = \psi_{i_1,i_2}^0, \quad \boldsymbol{\phi}_{\boldsymbol{i}}^1 = \begin{pmatrix} \boldsymbol{\psi}_{i_1,i_2}^{1,1} \\ \boldsymbol{\psi}_{i_1,i_2}^{1,2} \end{pmatrix}, \quad \phi_{\boldsymbol{i}}^3 = \psi_{i_1,i_2}^3.$$

We can summarize these points in the following de Rham sequence:

de Rham Sequence 1

$$
\begin{array}{ccccc}
& \nabla & & rot & \\
H^1(\Omega) & \longrightarrow & H(rot,\Omega) & \longrightarrow & L^2(\Omega) \\
& & & & \\
\Pi_0\downarrow & & \Pi_1\downarrow & & \Pi_3\downarrow \\
& \nabla & & rot & \\
V_0 & \longrightarrow & V_1 & \longrightarrow & V_3 \\
& & & & \\
\mathcal{S}^{p,p} & & \begin{pmatrix} \mathcal{S}^{p-1,p} \\ \mathcal{S}^{p,p-1} \end{pmatrix} & & \mathcal{S}^{p-1,p-1}
\end{array}
$$

The commuting relations are essential to mimetic methods. Essentially they state that operations at the continuous level are mimicked by equivalent relations at the discrete level [13]. In this case, it makes no difference whether we take the derivative and then convert to discrete variables or first map to discrete variables and then take the discrete derivative [56]. $\Pi_0$ will be defined as the 2D spline interpolation at a set of points matching the dimension of $V_0$. The projectors $\Pi_1$ and $\Pi_3$ then follow from the commuting diagram property. We quote in the following the formal definitions of the commuting projectors $\Pi_0$, $\Pi_1$ and $\Pi_3$. Take the domain $\Omega = [0,1] \times [0,1]$ and let the sequence $\{x_0 \dots x_{Nx}\}$ be a set of points associated to the 1D spline space in the $x$ direction. We also denote the sequence $\{y_0 \dots y_{Ny}\}$ to be a set of points in the $y$ direction. Let $\mathcal{V}$ be the set of vertices, where $\mathcal{V}_v = \{(x_i, y_j)\}$, $\mathcal{E}$ the set of edges, where $\mathcal{E} = \{([x_i, x_{i+1}], y_j), (x_i, [y_j, y_{j+1}])\}$ and $\mathcal{Q}$ be the set of all elements, where $\mathcal{Q} = \{([x_i, x_{i+1}], [y_j, y_{j+1}])\}$. Then the projectors referred to in the de Rham sequence are defined as:

- For $\Pi_0$:

$$\Pi_0 : H^1 \longrightarrow V_0, \quad \text{such that} \quad \Pi_0 u(v_k) = u(v_k), \forall v_k \in \mathcal{V}$$

- For $\Pi_1$:

$$\Pi_1 : H(rot;\Omega) \longrightarrow V_1, \quad \text{such that} \quad \int_{e_k} \Pi_1 \boldsymbol{u} \cdot \boldsymbol{t} \, de_k := \int_{e_k} \boldsymbol{u} \cdot \boldsymbol{t} \, de_k, \forall e_k \in \mathcal{E}$$

  where $\boldsymbol{t}$ is the tangential unit vector along the edge $e_k$.

- For $\Pi_3$:

$$\Pi_3 : L^2(\Omega) \longrightarrow V_3, \quad \text{such that} \quad \int_{s_k} \Pi_3 u \, ds_k = \int_{s_k} u \, ds_k, \forall s_k \in \mathcal{Q}$$

The optimal interpolation points for splines are the Greville points defined as the mean location of $p-1$ consecutive knots in the knot vector for each basis spline function of order $p$: given a knot vector $T = (t_i)_{1 \leqslant i \leqslant N+p+1}$, then the Greville point is defined as

$$\gamma_i = \frac{t_{i+1} + \cdots + t_{i+p}}{p}.$$

Contrary to the case of 3D, we have a second de Rham sequence in the case of 2D. We follow similar steps to those taken to arrive to the first sequence. For any function $w \in H^1(\Omega)$, with $\nabla^\perp$ denoting the curl operator ($\nabla^\perp F = (\partial_y F, \ -\partial_x F)^T$) and $\nabla \cdot$ denoting the divergence operator ($\nabla \cdot \boldsymbol{F} = \partial_x F_x + \partial_y F_y$), it holds that $\nabla \cdot (\nabla^\perp w) = 0$ ($\partial_x \partial_y F - \partial_y \partial_x F = 0$), thus it is clear that $\nabla^\perp w \in H(div;\Omega)$ and since the domain $\Omega$ is simply connected, we also know that the range of the curl operator is equal to the kernel of the divergence operator, namely $Im(\nabla^\perp) = ker(\nabla \cdot)$. This is summarized in the de Rham diagram:

de Rham Diagram 2

$$\mathbb{R} \quad \xrightarrow{\phantom{xx}} \quad H^1(\Omega) \quad \xrightarrow{\nabla^\perp} \quad H(div, \Omega) \quad \xrightarrow{\nabla \cdot} \quad L^2(\Omega) \quad \longrightarrow 0$$

Where the Sobolev spaces have been defined earlier. In order to discretize continuous problems where the variable fields belong to the above mentioned Sobolev spaces, it is indispensable to construct finite dimensional spaces $V_0 \subset H^1(\Omega)$, $V_2 \subset H(div;\Omega)$ and $V_3 \subset L^2(\Omega)$, maintaining the same relationships of the continuous spaces given. The first step is to construct suitable discretizations of the spaces. We note that the curl of a function living in $\mathcal{S}^{p,p}$ belongs to $\begin{pmatrix} \mathcal{S}^{p,p-1} \\ \mathcal{S}^{p-1,p} \end{pmatrix}$ and the divergence of fields living in this last space belong to $\mathcal{S}^{p-1,p-1}$. To define the

discrete space belonging to $H(div; \Omega)$, we first denote by:

$$\boldsymbol{\psi}_{i,j}^{2,1} = \begin{pmatrix} N_i^p(x)N_j^{p-1}(y) \\ 0 \end{pmatrix}, \quad \boldsymbol{\psi}_{i,j}^{2,2} = \begin{pmatrix} 0 \\ N_i^{p-1}(x)N_j^p(y) \end{pmatrix}.$$

And in turn the discrete space $V_2$ is defined as:

$$V_2 = span\{\boldsymbol{\psi}_i^{2,1}, \boldsymbol{\psi}_j^{2,2}, \ 1 \leq i \leq N_x, \ 1 \leq j \leq N_y\}.$$

To confirm the statement above about the preservation of the diagram at the discrete level, we take the curl $(\nabla^\perp)$ of the basis functions defined on $V_0$:

$$\nabla^\perp \psi_{i,j}^0 = \nabla^\perp (N_i^p(x)N_j^p(y)) = \begin{pmatrix} \alpha N_i^p(x)N_j^{p-1}(y) - \beta N_i^p(x)N_{j+1}^{p-1}(y) \\ -\alpha N_i^{p-1}(x)N_j^p(y) + \beta N_{i+1}^{p-1}(x)N_j^p(y) \end{pmatrix}$$

$$= \begin{pmatrix} \alpha \boldsymbol{\psi}_{i,j}^{2,1} - \beta \boldsymbol{\psi}_{i,j+1}^{2,1} \\ -\alpha \boldsymbol{\psi}_{i,j}^{2,2} + \beta \boldsymbol{\psi}_{i+1,j}^{2,2} \end{pmatrix} \subset V_2,$$

which are the basis functions defining the $V_2$ space up to a constant. Now, if we take the divergence $(\nabla \cdot)$ of these basis functions, we get:

$$\nabla \cdot \nabla^\perp \psi_{i,j}^0 = \partial_x (\alpha N_i^p(x)N_j^{p-1}(y) - \beta N_i^p(x)N_{j+1}^{p-1}(y))$$
$$+ \partial_y (-\alpha N_i^{p-1}(x)N_j^p(y) + \beta N_{i+1}^{p-1}(x)N_j^p(y))$$

$$\nabla \cdot \nabla^\perp \psi_{i,j}^0 = \alpha(\alpha N_i^{p-1}(x)N_j^{p-1}(y) - \beta N_{i+1}^{p-1}(x)N_j^{p-1}(y))$$
$$- \beta(\alpha N_i^{p-1}(x)N_{j+1}^{p-1}(y) - \beta N_{i+1}^{p-1}(x)N_{j+1}^{p-1}(y))$$
$$- \alpha(\alpha N_i^{p-1}(x)N_j^{p-1}(y) - \beta N_i^{p-1}(x)N_{j+1}^{p-1}(y))$$
$$+ \beta(\alpha N_{i+1}^{p-1}(x)N_j^{p-1}(y) - \beta N_{i+1}^{p-1}(x)N_{j+1}^{p-1}(y))$$

$$\nabla \cdot \nabla^\perp \psi_{i,j}^0 = \alpha(\alpha \psi_{i,j}^3 - \beta \psi_{i+1,j}^3) - \beta(\alpha \psi_{i,j+1}^3 - \beta \psi_{i+1,j+1}^3)$$
$$- \alpha(\alpha \psi_{i,j}^3 - \beta \psi_{i,j+1}^3) + \beta(\alpha \psi_{i+1,j}^3 - \beta \psi_{i+1,j+1}^3) = 0.$$

Hence, the diagram is preserved at the discrete level. We define here also the single index notation for the basis functions defined on $V_2$ to be used later on:

$$\boldsymbol{\phi}_{\boldsymbol{i}}^2 = \begin{pmatrix} \boldsymbol{\psi}_{i_1,i_2}^{2,1} \\ \boldsymbol{\psi}_{i_1,i_2}^{2,2} \end{pmatrix}.$$

The main points of the second de Rham sequence are summarized as:

$$
\begin{array}{ccccc}
& \nabla^\perp & & \nabla \cdot & \\
H^1(\Omega) & \longrightarrow & H(div, \Omega) & \longrightarrow & L^2(\Omega) \\
\\
\Pi_0\downarrow & & \Pi_2\downarrow & & \Pi_3\downarrow \\
& \nabla^\perp & & \nabla \cdot & \\
V_0 & \longrightarrow & V_2 & \longrightarrow & V_3 \\
\\
\mathcal{S}^{p,p} & & \begin{pmatrix} \mathcal{S}^{p,p-1} \\ \mathcal{S}^{p-1,p} \end{pmatrix} & & \mathcal{S}^{p-1,p-1}
\end{array}
$$

de Rham Sequence 2

where the commuting projector $\Pi_2$ is defined as:

$$
\Pi_2 : H(div; \Omega) \longrightarrow V_2, \quad \text{such that} \quad \int_{e_k} \Pi_2 \boldsymbol{u} \cdot \boldsymbol{n} := \int_{e_k} \boldsymbol{u} \cdot \boldsymbol{n} \, de_k, \forall e_k \in \mathcal{E}
$$

Where $\boldsymbol{n}$ is the normal unit vector to the edge $e_k$. There is a large amount of work on the numerical analysis of the commuting diagram involving the projections from the continuous de Rham diagram to its discrete counterpart [24][25].

## 2.4 Discrete Differential Operators

Thanks to the commuting de Rham sequence, we can solve equations in the strong form (on the B-splines coefficients level). To do that, we will need to define appropriate discrete differential operators in 2D, corresponding to the divergence operator ($\nabla \cdot$), the rot operator (rot), the curl operator ($\nabla^\perp$) and the gradient operator ($\nabla$), in the following manner:

- The Discrete Curl:

$$
\mathcal{C} = \begin{pmatrix} \mathbb{I} \otimes \mathbb{D} \\ -\mathbb{D} \otimes \mathbb{I} \end{pmatrix}
$$

- The Discrete Divergence:

$$
\mathcal{D} = \begin{pmatrix} \mathbb{D} \otimes \mathbb{I} & \mathbb{I} \otimes \mathbb{D} \end{pmatrix}
$$

- The Discrete Gradient:

$$\mathcal{G} = \begin{pmatrix} \mathbb{D} \otimes \mathbb{I} \\ \mathbb{I} \otimes \mathbb{D} \end{pmatrix}$$

- The Discrete Rot:

$$\mathcal{R} = \begin{pmatrix} -\mathbb{I} \otimes \mathbb{D} & \mathbb{D} \otimes \mathbb{I} \end{pmatrix}$$

where $\mathbb{D}$ is the difference (incidence) matrix (the first order finite differences operator) coming from the derivative formula for a spline, defined in the case of vanishing boundary conditions as:

$$\mathbb{D} = \underbrace{\begin{pmatrix} -1 & 1 & 0 & \dots & 0 \\ 0 & -1 & 1 & \dots & 0 \\ \vdots & \vdots & \vdots & \ddots & \vdots \\ 0 & \dots & \dots & -1 & 1 \end{pmatrix}}_{\mathbf{n+p}} \left.\vphantom{\begin{pmatrix} -1 \\ 0 \\ \vdots \\ 0 \end{pmatrix}}\right\} \mathbf{n+p-1}$$

where n is the number of elements in each direction and p is the B-spline degree. $\mathbb{I}$ is the identity matrix of dimensions $(n + p - 1) \times (n + p - 1)$

## 2.5 Maxwell's Equations in 2D:

In the following, we aim to demonstrate how using compatible spaces is advantageous by applying the tools outlined above to Maxwell's equations. The model for Maxwell's equations in 2D defined on $\Omega = [0,1] \times [0,1]$, $t \in [0,T]$, where t is the time and T is the final time, at the continuous level is given by:

$$\begin{cases} -\partial_t \boldsymbol{E} + \nabla^\perp B = \boldsymbol{J} & \text{Ampere's Law} \\ \partial_t B + rot\boldsymbol{E} = 0 & \text{Faraday's Law} \end{cases} \tag{2.5.2}$$

with adequate boundary conditions which are defined later on. Where $\boldsymbol{E}$ is the electric field (vector field), $B$ is the magnetic field (scalar field) and $\boldsymbol{J}$ is the current density. $rot\boldsymbol{E} = -\partial_y E_x + \partial_x E_y$ and $\nabla^\perp B = (\partial_y B, \; -\partial_x B)^T$.

The issue of long time stability for Maxwell's solvers is strongly related to the preservation of the divergence constrains ($\nabla \cdot \boldsymbol{B} = 0$ and Gauss law) at the discrete level [17]. The adherence to this condition leads us to an additional criterion to couple the current density with the charge density, which is formulated as a discrete version of the continuity equation $\partial_t \rho + \nabla \cdot \boldsymbol{J} = 0$ (where $\rho$ is the charge density),

since this is the relation that guarantees the preservation of Gauss's law for the exact solutions to the Faraday and Ampere equations.

Classically, one resorts to correction techniques of the Maxwell's equations [28][33][38] in order to remedy this lack of discrete charge conservation. That said, such methods (divergence cleaning methods, projection methods, etc) introduce artificial non locality in the numerical scheme which blows up the solution. An example in the field of laser plasma interactions where these non localities could give rise to an instability before the laser hits the plasma can be found in [17]. The work conducted here aims at reproducing the results reached in [16][17], which postulates that part of the numerical artifacts which are often designated as a lack of charge conservation is due to using discretizations of the Maxwell equations which do not preserve Gauss's law, as can be seen in [46]. We present in this section that choice of discretization that we use for Maxwell equations and present the associated numerical results. The invariant that we want to preserve:

> **Invariant property**
>
> The charge conservation: $\partial_t(\rho - \nabla \cdot E) = 0$, where $\rho$ is the charge density.

**Remark 2.5.1.** To get the charge conservation, we start with Ampere's Law:

$$- \partial_t \boldsymbol{E} + \nabla^\perp B = \boldsymbol{J} \tag{2.5.3}$$

We apply the divergence to Eq. (2.5.3) and obtain:

$$- \partial_t \nabla \cdot \boldsymbol{E} = \nabla \cdot \boldsymbol{J} \tag{2.5.4}$$

Where we have used $\nabla \cdot (\nabla^\perp B) = 0$. Substituting for $\nabla \cdot \boldsymbol{J}$ in the mass conservation equation:

$$\partial_t \rho + \nabla \cdot \boldsymbol{J} = 0 \tag{2.5.5}$$

Thus:

$$\partial_t(\rho - \nabla \cdot \boldsymbol{E}) = 0 \tag{2.5.6}$$

where $\nabla \cdot \boldsymbol{E} = \partial_x E_x + \partial_y E_y$, which means that $\nabla \cdot \boldsymbol{E} = \rho$ for all times provided that $\nabla \cdot \boldsymbol{E}_0 = \rho_0$.

## 2.5.1 The Spatial Discretization and the associated de Rham Sequence

In order to choose the correct spaces for model (2.5.2) that ensures the exact preservation of the invariant quantity, we refer to the 2D de Rham sequence introduced earlier in Section [2.3]. We start by taking $B \in H^1(\Omega)$, and as we apply the curl operator, $\nabla^\perp$, on the magnetic field, this leads to having $\boldsymbol{E} \in H(div; \Omega)$, as we aim to solving Ampere's law strongly. Such a choice of spaces, dictates that the current density, $\boldsymbol{J}$, to be defined in $H(div; \Omega)$ and we apply the commuting projector $\Pi_2$ to Ampere's Law:

$$-\partial_t \Pi_2 \boldsymbol{E} + \Pi_2 \nabla^\perp B = \Pi_2 \boldsymbol{J} \tag{2.5.7}$$

and from the commuting diagram, we have $\Pi_2 \nabla^\perp B = \nabla^\perp \Pi_0 B$, so:

$$-\partial_t \Pi_2 \boldsymbol{E} + \nabla^\perp \Pi_0 B = \Pi_2 \boldsymbol{J}. \tag{2.5.8}$$

We define $\boldsymbol{E}_h = \Pi_2 \boldsymbol{E}, B_h = \Pi_0 B$ and $\boldsymbol{J}_h = \Pi_2 \boldsymbol{J}$, hence $\boldsymbol{E}_h \in V_2, B_h \in V_0$ and $\boldsymbol{J}_h \in V_2$, so the discrete Ampere's law writes:

$$-\partial_t \boldsymbol{E}_h + \nabla^\perp B_h = \boldsymbol{J}_h. \tag{2.5.9}$$

The choice of having $\boldsymbol{E} \in H(div; \Omega)$ is not compatible with Faraday's law at the strong level, hence we consider the weak form of Faraday's law and use integration by parts. Now we choose a test function $u \in H^1(\Omega)$ and take the dot product with Faraday's equation and integrate by parts over the domain $\Omega$:

$$\partial_t \int_\Omega Bu + \int_\Omega (rot\boldsymbol{E})u = 0. \tag{2.5.10}$$

We integrate by parts the term $\int_\Omega (rot\boldsymbol{E})u$, using Green's formula which reads:

$$\int_\Omega (rotG)\boldsymbol{F}dX = \int_\Omega G(rot\boldsymbol{F})dX - \int_\Gamma G(\boldsymbol{F} \cdot \boldsymbol{n}^\perp)dS, \forall \boldsymbol{F} \in H(rot; \Omega), \forall G \in H^1(\Omega). \tag{2.5.11}$$

Hence,

$$\int_\Omega (rot\boldsymbol{E})u = \int_\Omega \boldsymbol{E} \cdot \nabla^\perp u - \int_\Gamma (\boldsymbol{E} \cdot \boldsymbol{n}^\perp)u. \tag{2.5.12}$$

For simplicity we set $\boldsymbol{E} \cdot \boldsymbol{n}^\perp |_\Gamma = 0$. We discretize the weak form by using the discrete counterparts of: $\boldsymbol{E} \in H(div; \Omega), B \in H^1(\Omega), u \in H^1(\Omega)$, that is $\boldsymbol{E}_h \in$

$V_2, B_h \in V_0, u_h \in V_0$. Hence, the discrete weak form of Faraday's law reads: Find $B_h \in V_0$ such that:

$$\partial_t \int_\Omega B_h u_h + \int_\Omega \boldsymbol{E}_h \cdot \nabla^\perp u_h = 0, \quad \forall u_h \in V_0. \tag{2.5.13}$$

We summarize the spatial discretization in the following box:

---

**Spatial Discretization of Maxwell's Equations in 2D**

Find $B_h \in V_0, \boldsymbol{E}_h \in V_2$, such that:

$$\partial_t \int_\Omega B_h u_h + \int_\Omega \boldsymbol{E}_h \cdot \nabla^\perp u_h = 0, \quad \forall u_h \in V_0$$

and

$$-\partial_t \boldsymbol{E_h} + \nabla^\perp B_h = \boldsymbol{J}_h$$

where $\boldsymbol{J}_h = \Pi_2 \boldsymbol{J} \in V_2$.

---

This spatial discretization holds true for (2.5.2) provided taking $\rho_h = \Pi_3 \rho$ and applying the commuting diagram to $\frac{\partial \rho}{\partial t} + \nabla \cdot \boldsymbol{J} = 0$, as will be verified later on.

## 2.5.2 Discretization in time

We apply the general $\theta$-scheme to the previously derived spatially discretized Maxwell's model. We start with Ampere's Law that is taken in the strong form thanks to the commuting projectors:

$$\boldsymbol{E}_h^{n+1} - \boldsymbol{E}_h^n - \theta \Delta t \nabla^\perp B_h^{n+1} - (1-\theta)\Delta t \nabla^\perp B_h^n = -\theta \Delta t \boldsymbol{J}_h^{n+1} - (1-\theta)\Delta t \boldsymbol{J}_h^n. \tag{2.5.14}$$

We apply the time discretization to Faraday's law as well:

$$\int_\Omega B_h^{n+1} u_h - \int_\Omega B_h^n u_h + \theta \Delta t \int_\Omega \boldsymbol{E}_h^{n+1} \cdot \nabla^\perp u_h + (1-\theta)\Delta t \int_\Omega \boldsymbol{E}_h^n \cdot \nabla^\perp u_h = 0. \tag{2.5.15}$$

We substitute for $\boldsymbol{E}_h^{n+1}$ in Eq. (2.5.15) from Eq. (2.5.14) and get the following numerical scheme to solve:

> **Maxwell's Equations Discretized in Space and Time**
>
> We first solve for $B_h^{n+1} \in V_0$, such that $\boldsymbol{E}_h \in V_2$ and $\boldsymbol{J}_h \in V_2$, such that:
>
> $$\begin{cases} \int_\Omega B_h^{n+1} u_h + \theta^2 \Delta t^2 \int_\Omega \nabla^\perp B_h^{n+1} \cdot \nabla^\perp u_h - \Delta t^2 \theta^2 \int_\Omega \boldsymbol{J}_h^{n+1} \cdot \nabla^\perp u_h \\[2ex] = \int_\Omega B_h^n u - \Delta t \int_\Omega \boldsymbol{E}_h^n \cdot \nabla^\perp u_h - \theta(1-\theta)\Delta t^2 \int_\Omega \nabla^\perp B_h^n \cdot \nabla^\perp u_h \\[2ex] + \theta(1-\theta)\Delta t^2 \int_\Omega \boldsymbol{J}_h^n \cdot \nabla^\perp u_h, \quad \forall u_h \in V_0 \end{cases}$$
>
> $$(2.5.16)$$
>
> Once $B_h^{n+1}$ has been obtained from Eq. (2.5.16), we get directly $\boldsymbol{E}_h^{n+1}$ in strong form via:
>
> $$\begin{cases} \boldsymbol{E}_h^{n+1} - \boldsymbol{E}_h^n - \theta \Delta t \nabla^\perp B_h^{n+1} - (1-\theta)\Delta t \nabla^\perp B_h^n = -\theta \Delta t \boldsymbol{J}_h^{n+1} \\[2ex] -(1-\theta)\Delta t \boldsymbol{J}_h^n \end{cases}$$
>
> $$(2.5.17)$$

This numerical scheme can also be written in the matrix form, this translates to:

> **Matrix Form**
>
> $$\begin{cases} (M_0 + \theta^2 \Delta t^2 \mathcal{C}^T M_2 \mathcal{C})\boldsymbol{B}^{n+1} - \Delta t^2 \theta^2 \mathcal{C}^T M_2 \boldsymbol{J}^{n+1} = \\[2ex] (M_0 - \theta(1-\theta)\Delta t^2 \mathcal{C}^T M_2 \mathcal{C})\boldsymbol{B}^n - \Delta t \mathcal{C}^T M_2 \boldsymbol{\mathcal{E}}^n + \theta(1-\theta)\Delta t^2 \mathcal{C}^T M_2 \boldsymbol{J}^n \end{cases}$$
>
> $$(2.5.18)$$
>
> $$\begin{cases} \boldsymbol{\mathcal{E}}^{n+1} - \boldsymbol{\mathcal{E}}^n - \theta \Delta t \mathcal{C} \boldsymbol{B}^{n+1} - (1-\theta)\Delta t \mathcal{C} \boldsymbol{B}^n = -\theta \Delta t \Pi_2 \boldsymbol{J}^{n+1} \\[2ex] -(1-\theta)\Delta t \Pi_2 \boldsymbol{J}^n \end{cases}$$
>
> $$(2.5.19)$$
>
> where $M_2 = ((\int_\Omega \boldsymbol{\phi}_i^2 \cdot \boldsymbol{\phi}_j^2 d\boldsymbol{x}))_{i,j}$ is the mass matrix in $V_2$ and $M_0 = ((\int_\Omega \phi_i^0 \phi_j^0 d\boldsymbol{x}))_{i,j}$ is the mass matrix in $V_0$. $\boldsymbol{B}$, $\boldsymbol{\mathcal{E}}$ and $\boldsymbol{J}$ are the vectors of spline coefficients. $\mathcal{C}$ is the discrete curl operator.

### 2.5.3 Test Case: Issautier 2D

We use the analytical current source proposed in [21][59] to study the charge conservation properties. The Issautier 2D solution:

- The Current Density:

$$\boldsymbol{J}(t, x, y) = (\cos(t) - 1) \begin{pmatrix} \pi \cos(\pi y) + \pi^2 y \sin(\pi x) \\ \pi \cos(\pi x) + \pi^2 x \sin(\pi y) \end{pmatrix} - \cos(t) \begin{pmatrix} x \sin(\pi y) \\ y \sin(\pi x) \end{pmatrix} \tag{2.5.20}$$

- The Electric Field:

$$\boldsymbol{E}(t, x, y) = \sin(t) \begin{pmatrix} x \sin(2\pi y) \\ y \sin(2\pi x) \end{pmatrix} \tag{2.5.21}$$

- The Magnetic Field:

$$B(t) = (\cos(t) - 1)(\pi y \cos(2\pi y) - \pi x \cos(2\pi y)) \tag{2.5.22}$$

- The Charge Density:

$$\rho(t, x, y) = \cos(t)(\sin(2\pi x) + \sin(2\pi y)) \tag{2.5.23}$$

Fig.(2.3) shows the convergence rates for running the Issautier test case, we can see that the solutions for the magnetic and electric fields are convergent at second order as expected.



(A) B     (B) $E_x$     (C) $E_y$
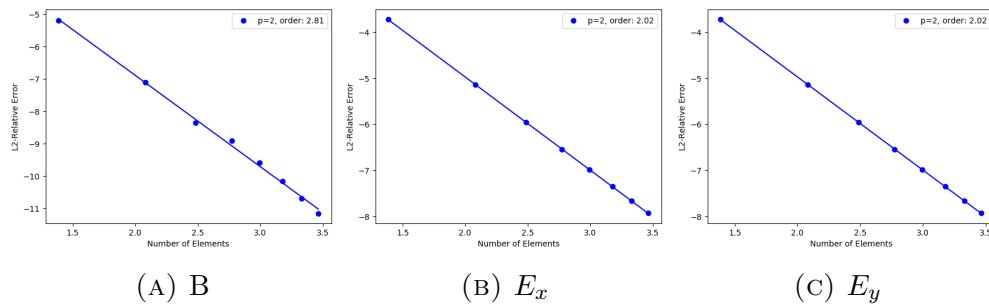
FIGURE 2.3: Log-Log plot showing the convergence orders for the Maxwell's equations in 2D for the scalar magnetic field and the electric vector field.

For the computation of the charge density numerically, we start by applying the commuting projector $\Pi_3$ to the continuity equation:

$$\partial_t \Pi_3 \rho + \Pi_3 \nabla \cdot \boldsymbol{J} = 0, \tag{2.5.24}$$

then we use that $\Pi_3 \nabla \cdot = \nabla \cdot \Pi_2$, and define the discrete fields $\rho_h = \Pi_3 \rho$ and $\boldsymbol{J}_h = \Pi_2 \boldsymbol{J}$, so the spatially discrete continuity equation writes:

$$\partial_t \rho_h + \nabla \cdot \boldsymbol{J}_h = 0. \tag{2.5.25}$$

We then discretize Eq. (2.5.25) in time:

$$\rho_h^{n+1} - \rho_h^n + \Delta t \nabla \cdot \boldsymbol{J}_h^n = 0, \tag{2.5.26}$$

where we define: $\boldsymbol{J}_h^n = \frac{1}{\Delta t} \int_{t_n}^{t_{n+1}} \Pi_2 \boldsymbol{J} dt$. Then we refer back to Eq. (2.5.4):

$$-\partial_t \nabla \cdot \boldsymbol{E} = \nabla \cdot \boldsymbol{J}. \tag{2.5.27}$$

We apply $\Pi_3$ to Eq. (2.5.27) and use that $\Pi_3 \nabla \cdot = \nabla \cdot \Pi_2$ and discretize in time:

$$-\nabla \cdot (\boldsymbol{E}_h^{n+1} - \boldsymbol{E}_h^n) = \Delta t \nabla \cdot \boldsymbol{J}_h^n, \tag{2.5.28}$$

and we substitute for $\Delta t \nabla \cdot \boldsymbol{J}_h^n$ in Eq. (2.5.28) from Eq. (2.5.26):

$$\nabla \cdot (\boldsymbol{E}_h^{n+1} - \boldsymbol{E}_h^n) = \rho_h^{n+1} - \rho_h^n \tag{2.5.29}$$

$$\nabla \cdot \boldsymbol{E}_h^{n+1} - \rho_h^{n+1} = \nabla \cdot \boldsymbol{E}_h^n - \rho_h^n, \tag{2.5.30}$$

and as $\nabla \cdot \boldsymbol{E}_h^0 - \rho_h^0 = 0$, then the discrete charge conservation quantity that we investigate written in the matrix form is:

$$\mathcal{D}\boldsymbol{\mathcal{E}}^{n+1} - \boldsymbol{\mathcal{P}}^{n+1} = 0, \tag{2.5.31}$$

where $\boldsymbol{\mathcal{E}}$ and $\boldsymbol{\mathcal{P}}$ are the vectors of spline coefficients, and $\mathcal{D}$ is the discrete divergence operator.

We proved here that thanks to the commuting diagram property, we have exactly $\nabla \cdot \boldsymbol{E}_h^n = \rho^n$ at all times. This is not the case in general. In Fig. (2.4), we can see that in the case of using the commuting projection, the charge density is preserved in time up to $10^{-14}$ over 10000 time steps, whereas in the case of using the $L^2$ projection, we lose the charge conservation.

(A) Commuting Projection
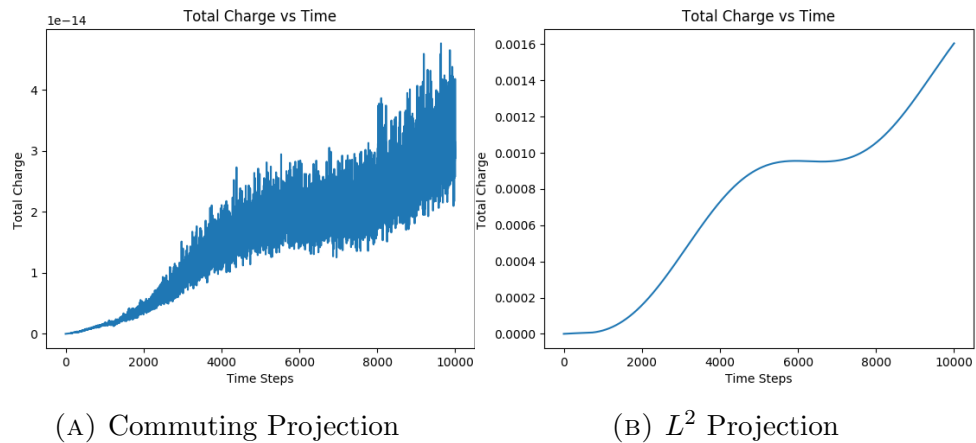
(B) $L^2$ Projection

FIGURE 2.4: Plot of the L2 norm of $\nabla \cdot \boldsymbol{E}_h^n - \rho_h^n$ over time. The plot on the left shows the evolution using the commuting projection for the current density, whereas the plot on the right shows the evolution using the classical $L^2$ projection.

As stated above, using compatible spaces for FEM allows to preserve the invariant properties of the equations at question, where this is the charge conservation in the case of the Maxwell's equations. It also gives the possibility to use directly the strong form in certain cases, whereas in the framework of classical FEM, one needs to use the weak form. For example, we have solved Ampere's equation strongly, which allowed us to avoid inverting a mass matrix in order to compute $\boldsymbol{E}$, which would have been the case, had we used the classical FE formulation.

# Chapter 3

# Linear MHD and Numerics

In this Chapter we present the linear MHD Model which is sufficient in order to tackle some difficulties present at the numerical level like the multiscale problem in time and space, and we present the associated numerical results. We start by outlining the MHD models in general and their relevance to fusion research [62]. In section (3.1.2) we speak about the importance of the divergence free condition in the context of computational MHD. We then introduce the normalization, linearization and analyse the associated waves of the linear MHD model under consideration, in sections (3.1.3), (3.1.4) and (3.1.5), respectively. At that point, we lay the ground for an energy preserving splitting, as can be seen in section (3.2) and introduce a time scheme based on that.

The splitting introduced in section (3.2) leads to three separate steps: The linear acoustic step, this is covered in section (3.3), the linear magnetic step, this is covered in section (3.4), and the linear convection-diffusion step, this is covered in section (3.5). For the acoustic step, we present in section (3.3.2) the strategy that we use for discretizing the acoustic step spatially, and we supplement that with the time discretization outlined in section (3.3.3). We present the numerical results associated with the acoustic step in section (3.3.5), whereas in section (3.3.5.1) we include the results for an exact solution on the closed system. Section (3.3.5.3) derives the case of manufactured solution, and the numerical results for a time dependent case are presented in section (3.3.5.4). The magnetic step, section (3.4) and the convection-diffusion step, section (3.5) follow a structure similar to the acoustic step.

Finally, we present the numerical results for the linear MHD as a full system in section (3.6) and end the chapter with the Conclusions in section (3.7).

# 3.1 MHD and Simplified Models:

## 3.1.1 Introduction

Magnetohydrodynamics (MHD) is a fluid model that describes the evolution of fluids which conduct electricity under the presence of a magnetic field and analyses their stability properties and equilibrium states. The MHD model has wide applicability that transcends astrophysical and laboratory plasmas, due to its ability to describe different physical systems and phenomena [58].

For the purposes of fusion devices, MHD is used to predict different operational limits which are associated with the triggering of instabilities that could hinder the plasma confinement and pose danger on the confinement vessel. Hence, one could say that one of the purposes of MHD simulations in fusion plasmas is to shed a light into the regimes that lead to disruptive instabilities, and in turn, how to either suppress or avoid the onset of such events. [34].

That said, the attractiveness of using the MHD model for such studies doesn't come at no cost; the MHD model is not easy to tackle and performing numerical simulations on it is not an easy task. The MHD model in 3D has 8 independent variables (three components each for the velocity and the magnetic field, one for each of the density and pressure) plus the added complexity of the non-linearity. The model gives rise to three different types of waves operating in different scales that makes solving the system numerically a complex task. We start with the visco-resistive MHD model in 3D, and then move to performing respective simplifications and approximations which fit the purposes of this work.

We begin by outlining the viscous-resistive MHD fluid model in 3D which is a simplification of a two fluid model, what is also known as extended MHD [37]. The spatial variable is $\boldsymbol{x} \in \mathbb{R}^3$. The evolution of the plasma can be described, as

can be found in [64], by the following model:

$$
\begin{cases}
\partial_t \rho + \nabla \cdot (\rho \boldsymbol{u}) = 0 \\[2mm]
\rho \partial_t \boldsymbol{u} + \rho \boldsymbol{u} \cdot \nabla \boldsymbol{u} + \nabla p = \boldsymbol{J} \times \boldsymbol{B} + \nabla \cdot \overline{\overline{\boldsymbol{\Pi}}} \\[2mm]
\rho \partial_t T + \rho \boldsymbol{u} \cdot \nabla T + (\gamma - 1)\rho T \nabla \cdot \boldsymbol{u} = \nabla \cdot \boldsymbol{q} \\[2mm]
\partial_t \boldsymbol{B} - \nabla \times (\boldsymbol{u} \times \boldsymbol{B}) = -\eta \nabla \times \boldsymbol{J} \\[2mm]
\mu_0 \boldsymbol{J} = \nabla \times \boldsymbol{B}, \quad \nabla \cdot \boldsymbol{B} = 0
\end{cases}
\tag{3.1.1}
$$

Where $\rho$ is the density, $\boldsymbol{u}$ is the velocity, $T$ is the temperature, $p = \rho T$ is the isotropic pressure, $\overline{\overline{\boldsymbol{\Pi}}}$ is the stress tensor, $\boldsymbol{B}$ is the magnetic flux, $\boldsymbol{J}$ is the current density and $\boldsymbol{q}$ is the flux density of heat carried by particles of a given species. $\eta$ is the coefficient of resistivity. The resistive term is the result of the collision between the two species; electrons and ions of the plasma. $\mu_0$ is the permeability of free space and $\gamma$ is the ratio of specific heats for an adiabatic equation of state. In this work we will use the mono-atomic ideal gas value $\gamma = 5/3$. In the real MHD problem the heat flux $\boldsymbol{q}$ and the stress tensor $\overline{\overline{\boldsymbol{\Pi}}}$ depend on the magnetic flux and we obtain a diffusion process which depends on the direction of the magnetic field [31]. Since in this work we want to avoid treating the anisotropic problem imposed by the magnetic field and initially study a simpler dependency of these quantities, we propose to choose these quantities such that they give the classical diffusion of Navier-Stokes [20]:

$$
\nabla \cdot \overline{\overline{\boldsymbol{\Pi}}} = (\nu \Delta \boldsymbol{u} + (\nu + \lambda)\nabla(\nabla \cdot \boldsymbol{u})), \quad \boldsymbol{q} = \nabla \cdot (\zeta \nabla T)
\tag{3.1.2}
$$

where $\nu$ is the viscosity coefficient, and we have considered it as a constant for simplicity, whereas in reality it is a temperature-dependent factor whose gradient might not be negligible, $\lambda$ the second coefficient of viscosity [37] and $\zeta$ is the thermal conductivity. The differential operators are defined in the following way: $\nabla \cdot \boldsymbol{F} = \partial_x F_x + \partial_y F_y + \partial_z F_z$, $\nabla F = (\partial_x F, \partial_y F, \partial_z F)^T$, $\nabla \times \boldsymbol{F} = (\partial_y F_z - \partial_z F_y, \partial_z F_x - \partial_x F_z, \partial_x F_y - \partial_y F_x)^T$.

### 3.1.2 The Divergence-Free Condition

The divergence-free condition is one of the fundamental laws of physics which prohibits the existence of monopoles in nature. But holding such a condition at the discrete level proves to be a complicated task. The violation of this basic law of nature, the divergence-free condition, at the discrete level could result in the triggering of nonphysical processes. One example of such processes in the context of fusion devices is the onset of a fictitious plasma transport orthogonal to the magnetic field lines. This in turn violates the conservation of momentum and energy [12] and could result in the triggering of numerical instabilities [11]. For more details into the importance of the divergence-free condition at the discrete level for MHD modelling, one could refer to [12] [11] [29] [22] [67]. Considering how intricate of a model the MHD system is, plus the added complexity of finding ways to conserve the divergence free condition, it is of a paramount importance to devise numerical schemes which are accurate and physically and numerically stable. Several methods are found in literature that aims to reach this target for the different forms of MHD models; divergence-cleaning methods, constrained transport methods, divergence-free bases, etc. For more details on the subject matter and detailed analysis of such methods, one could refer to [67][23][6]. For the purposes of this work, we rely on well established mathematical formulations and numerical methods for solving the linear MHD model. These tools are based on discrete differential forms and finite element exterior calculus, which guarantees the preservation of the divergence-free condition at the discrete level. For details, see [10][40][1][2].

### 3.1.3 Normalization

We now proceed to scale the unknown variables ($\boldsymbol{u}$, $\boldsymbol{B}$, $p$, $\rho$). To recast the equations into a useful form, the usual procedure is to write them in dimensionless form by scaling every variable by a characteristic value, this has the advantage of rendering the numerical solution valid for different cases which could be reproduced via recasting the variables by the characteristic value. We propose such normalization in order to obtain a set of dimensionless equations which allow us to distinguish between the different scales and regimes. Here, in an equivalent manner, we consider introducing $\rho_0$ as the characteristic density and $u_0$ is the flow velocity. For the mass conservation, we use the normalization $\rho = \rho^{'} \rho_0$ and

likewise $\boldsymbol{u} = \boldsymbol{u}' u_0$. This leads to the mass conservation to be rewritten as:

$$\partial_t \rho' + \left[\frac{t_0 u_0}{L}\right] \nabla \cdot (\rho' \boldsymbol{u}') = 0. \tag{3.1.3}$$

Note here that the quantities $\rho'$ *and* $\boldsymbol{u}'$ are dimensionless, whereas $u_0$ has the dimension of the velocity and $\rho_0$ has the dimension of the density. In a similar manner, we also used that $t = t' t_0$ and $L = L' L_0$, where $t_0$ is the characteristic time and $L_0$ is the characteristic length.

Using the same strategy for the rest of the equations of system (3.1.1), we introduce: $B_0$ is the characteristic magnetic field and $J_0$ is the characteristic current density, $T_0$ is the characteristic temperature and $p_0$ is the characteristic pressure. We also make use of the isotropic pressure relationship $p = \rho T$. We drop the superscript for simplicity, keeping in mind that the unknown quantities ($\boldsymbol{u}$, $\boldsymbol{B}$, $p$, $\rho$) are dimensionless:

$$
\begin{cases}
\partial_t \rho + \left[\dfrac{t_0 u_0}{L}\right] \nabla \cdot (\rho \boldsymbol{u}) = 0 \\[2ex]
\rho \partial_t \boldsymbol{u} + \left[\dfrac{t_0 u_0}{L}\right] \rho \boldsymbol{u} \cdot \nabla \boldsymbol{u} + \left[\dfrac{t_0 p_0}{\rho_0 u_0 L}\right] \nabla p = \left[\dfrac{t_0 J_0 B_0}{\rho_0}\right] \boldsymbol{J} \times \boldsymbol{B} + \left[\dfrac{t_0 \nu}{L^2 \rho_0}\right] \Delta \boldsymbol{u} \\[1ex]
+ \left[\dfrac{t_0 (\nu + \lambda)}{L^2 \rho_0}\right] \nabla (\nabla \cdot \boldsymbol{u}) \\[2ex]
\rho \partial_t T + \left[\dfrac{t_0 u_0}{L}\right] \rho \boldsymbol{u} \cdot \nabla T + \left[\dfrac{(\gamma - 1) t_0 u_0}{L}\right] \rho T \nabla \cdot \boldsymbol{u} = \left[\dfrac{(\gamma - 1) t_0 \eta T_0}{p_0 L^2}\right] \nabla \cdot (\zeta \nabla T) \\[2ex]
\partial_t \boldsymbol{B} - \left[\dfrac{t_0 u_0}{L}\right] \nabla \times (\boldsymbol{u} \times \boldsymbol{B}) = -\eta \left[\dfrac{t_0 J_0}{B_0 L}\right] \nabla \times \boldsymbol{J} \\[2ex]
\mu_0 \boldsymbol{J} = \left[\dfrac{B_0}{J_0 L}\right] \nabla \times \boldsymbol{B}, \quad \nabla \cdot \boldsymbol{B} = 0
\end{cases}
\tag{3.1.4}
$$

We define $V = \frac{t_0}{L}$ to be the characteristic velocity. We define also the Mach Number $M = \frac{u_0}{c}$ with $c$ the sound speed defined as $c^2 = \gamma \frac{p_0}{\rho_0}$, the Reynolds number (defined as the ratio of inertial forces to viscous forces within the fluid) $R_e = \frac{L \rho_0 u_0}{\nu}$, the magnetic Reynolds number (defined as the ratio of the advection due to the magnetic field to the magnetic diffusion) $R_m = \frac{L V \mu_0}{\eta}$, the Prandlt number (defined as the ratio of momentum diffusivity to thermal diffusivity) $P_r = \frac{\nu c_p}{\zeta}$.

**Remark 3.1.1.** There are two general types of behaviour for the magnetic field depending upon the value of $R_m$. If $R_m << 1$, then the magnetic diffusion is

important and the magnetic field will diffuse away, and inhomogeneities in the field will be smoothed out, as in the flow of a fluid smoothing out. If $R_m >> 1$, then there is no diffusion present, and the magnetic field lines tend to remain frozen into the plasma, moving along with the plasma flow [48].

We also define the $\beta$ - number (the ratio of the plasma pressure to the magnetic pressure) $\beta = \frac{c^2}{V_A^2}$ with $V_A$ the Alfven velocity defined by $V_A^2 = \frac{B_0^2}{\rho_0 \mu_0}$ (The Alfven velocity is the group velocity of the Alfven waves which are the basic solutions of the MHD equations.) and $k = \frac{\nu + \lambda}{\nu}$. By definition $J_0 = \frac{B_0}{L \mu_0}$. Using these relations we obtain the following system:

$$
\begin{cases}
\partial_t \rho + \left[\frac{u_0}{V}\right] \nabla \cdot (\rho \boldsymbol{u}) = 0 \\[2mm]
\rho \partial_t \boldsymbol{u} + \left[\frac{u_0}{V}\right] \rho \boldsymbol{u} \cdot \nabla \boldsymbol{u} + \left[\frac{c}{\gamma V M}\right] \nabla p = \left[\frac{V_A^2}{V u_0}\right] \boldsymbol{J} \times \boldsymbol{B} + \left[\frac{u_0}{V} \frac{1}{R_e}\right] \Delta \boldsymbol{u} \\[2mm]
\quad + \left[\frac{u_0}{V} \frac{1}{R_e}\right] k \nabla (\nabla \cdot \boldsymbol{u}) \\[2mm]
\rho \partial_t T + \left[\frac{u_0}{V}\right] \rho \boldsymbol{u} \cdot \nabla T + \left[\frac{(\gamma - 1) M c}{V}\right] \rho T \nabla \cdot \boldsymbol{u} = \left[\frac{(\gamma - 1) t_0 \eta T_0}{p_0 L^2}\right] \nabla \cdot (\zeta \nabla T) \\[2mm]
\partial_t \boldsymbol{B} - \left[\frac{u_0}{V}\right] \nabla \times (\boldsymbol{u} \times \boldsymbol{B}) = - \left[\frac{1}{R_m}\right] \nabla \times \boldsymbol{J} \\[2mm]
\boldsymbol{J} = \nabla \times \boldsymbol{B}, \quad \nabla \cdot \boldsymbol{B} = 0
\end{cases}
$$

$$(3.1.5)$$

Now we choose to define $V = \frac{u_0}{M^p \beta^q}$, where the choice of the powers p and q determines the regimes to operate within. If $p = q = 0$, then we have $V = u_0$, which is the characteristic velocity corresponding to the material velocity . If $p = 1$ and $q = 0$, then we have $V = c$, which is the sound speed. If $p = 1$ and $q = 0.5$

we have $V = V_A$. Using this we obtain:

$$
\begin{cases}
\partial_t \rho + M^p \beta^q \nabla \cdot (\rho \boldsymbol{u}) = 0 \\[2ex]
\rho \partial_t \boldsymbol{u} + M^p \beta^q \rho \boldsymbol{u} \cdot \nabla \boldsymbol{u} + \dfrac{\beta^q}{\gamma M^{2-p}} \nabla p = \dfrac{1}{M^{2-p} \beta^{1-q}} \boldsymbol{J} \times \boldsymbol{B} \\[1ex]
\quad + \dfrac{M^p \beta^q}{R_e} \left( \Delta \boldsymbol{u} + k \nabla (\nabla \cdot \boldsymbol{u}) \right) \\[2ex]
\rho \partial_t T + M^p \beta^q \rho \boldsymbol{u} \cdot \nabla T + (\gamma - 1) M^p \beta^q \rho T \nabla \cdot \boldsymbol{u} = \dfrac{(\gamma - 1) M^p \beta^q}{R_e P_r} \nabla \cdot (\nabla T) \\[2ex]
\partial_t \boldsymbol{B} - M^p \beta^q \nabla \times (\boldsymbol{u} \times \boldsymbol{B}) = -\dfrac{1}{R_m} \nabla \times \boldsymbol{J} \\[2ex]
\boldsymbol{J} = \nabla \times \boldsymbol{B}, \quad \nabla \cdot \boldsymbol{B} = 0
\end{cases}
$$

$$(3.1.6)$$

### 3.1.4 Linearization of the Model

We linearize the system (3.1.6) in order to reduce the complexity of the model. The linear model is sufficient to understand the multiscale problem and also manages to avoid some other difficulties that might occur in the nonlinear model like shock waves. We assume:

$$\boldsymbol{u} = \boldsymbol{a} + \delta \boldsymbol{u}, \quad \rho = \rho_0 + \delta \rho$$

$$T = T_0 + \delta T, \quad \boldsymbol{B} = \mathbf{b} + \delta \boldsymbol{B}$$

where the background magnetic equilibrium field is $\mathbf{b}$, $\rho_0$ is a reference density, $\boldsymbol{a}$ is the reference advection velocity and $T_0$ is a reference temperature, and we linearize

around these quantities. Using the above mentioned assumptions we obtain:

$$
\begin{cases}
\partial_t \delta\rho + M^p\beta^q \boldsymbol{a} \cdot \nabla\delta\rho + M^p\beta^q \nabla \cdot \delta\boldsymbol{u} = 0 \\[2ex]
\partial_t \delta\boldsymbol{u} + M^p\beta^q \boldsymbol{a} \cdot \nabla\delta\boldsymbol{u} + \dfrac{\beta^q}{\gamma M^{2-p}}(\nabla\delta\rho + \nabla\delta T) = \dfrac{1}{M^{2-p}\beta^{1-q}}((\nabla \times (\delta\boldsymbol{B})) \times \mathbf{b} \\[1ex]
+ \boldsymbol{J}_0 \times \delta\boldsymbol{B}) + \dfrac{M^p\beta^q}{R_e}(\Delta\delta\boldsymbol{u} + k\nabla(\nabla \cdot \delta\boldsymbol{u})) \\[2ex]
\partial_t \delta T + M^p\beta^q \boldsymbol{a} \cdot \nabla\delta T + (\gamma-1)M^p\beta^q \nabla \cdot \delta\boldsymbol{u} = \dfrac{(\gamma-1)M^p\beta^q}{R_e P_r}\nabla \cdot (\nabla\delta T) \\[2ex]
\partial_t \delta\boldsymbol{B} - M^p\beta^q \nabla \times (\boldsymbol{a} \times \delta\boldsymbol{B}) - M^p\beta^q \nabla \times (\delta\boldsymbol{u} \times \mathbf{b}) = -\dfrac{1}{R_m}\nabla \times \delta\boldsymbol{J} \\[2ex]
\delta\boldsymbol{J} = \nabla \times \delta\boldsymbol{B}, \quad \nabla \cdot \delta\boldsymbol{B} = 0
\end{cases}
\tag{3.1.7}
$$

We sum the first and the third equations of system (3.1.7), and define that $\delta p = \delta T + \delta\rho$. This leads to:

$$
\begin{cases}
\partial_t \delta p + M^p\beta^q \boldsymbol{a} \cdot \nabla\delta p + \gamma M^p\beta^q \nabla \cdot \delta\boldsymbol{u} = \dfrac{(\gamma-1)M^p\beta^q}{R_e P_r}\nabla \cdot (\nabla\delta T) \\[2ex]
\partial_t \delta\boldsymbol{u} + M^p\beta^q \boldsymbol{a} \cdot \nabla\delta\boldsymbol{u} + \dfrac{\beta^q}{\gamma M^{2-p}}\nabla\delta p = \dfrac{1}{M^{2-p}\beta^{1-q}}((\nabla \times (\delta\boldsymbol{B})) \times \mathbf{b} \\[1ex]
+ \boldsymbol{j} \times \boldsymbol{B}) + \dfrac{M^p\beta^q}{R_e}(\Delta\delta\boldsymbol{u} + k\nabla(\nabla \cdot \delta\boldsymbol{u})) \\[2ex]
\partial_t \delta\boldsymbol{B} - M^p\beta^q \nabla \times (\boldsymbol{a} \times \delta\boldsymbol{B}) - M^p\beta^q \nabla \times (\delta\boldsymbol{u} \times \mathbf{b}) = -\dfrac{1}{R_m}\nabla \times \delta\boldsymbol{J} \\[2ex]
\delta\boldsymbol{J} = \nabla \times \delta\boldsymbol{B}, \quad \nabla \cdot \delta\boldsymbol{B} = 0
\end{cases}
\tag{3.1.8}
$$

We remove the $\delta$ to simplify the notation. For the purposes of this work, we also reduce model (3.1.8) from a 3D model to a 2D model. We end up with:

$$
\begin{cases}
\partial_t p + M^p \beta^q \boldsymbol{a} \cdot \nabla p + \gamma M^p \beta^q \nabla \cdot \boldsymbol{u} = \dfrac{(\gamma - 1)M^p \beta^q}{R_e P_r} \nabla \cdot (\nabla p) \\[2em]
\partial_t \boldsymbol{u} + M^p \beta^q \boldsymbol{a} \cdot \nabla \boldsymbol{u} + \dfrac{\beta^q}{\gamma M^{2-p}} \nabla p = \dfrac{1}{M^{2-p}\beta^{1-q}} \left( (rot\boldsymbol{B}) \cdot \mathbf{b}^\perp - j \boldsymbol{B}^\perp \right) \\
+ \frac{M^p \beta^q}{R_e} \left( \Delta \boldsymbol{u} + k\nabla(\nabla \cdot \boldsymbol{u}) \right) \\[2em]
\partial_t \boldsymbol{B} + M^p \beta^q \nabla^\perp(\boldsymbol{a} \cdot \boldsymbol{B}^\perp) + M^p \beta^q \nabla^\perp(\boldsymbol{u} \cdot \mathbf{b}^\perp) = -\dfrac{1}{R_m} \nabla^\perp (rot\boldsymbol{B}) \\[2em]
\nabla \cdot \boldsymbol{B} = 0
\end{cases}
\tag{3.1.9}
$$

Note that we have used $\nabla^\perp(\boldsymbol{a} \cdot \boldsymbol{B}^\perp) + \boldsymbol{a}\nabla \cdot \boldsymbol{B} = \boldsymbol{a} \cdot \nabla\boldsymbol{B}$ and we define: $\mathbf{b}^\perp = (-b_2, b_1)^T$, $\boldsymbol{B}^\perp = (-B_2, B_1)^T$ and the current density in 2D is $j = rot\boldsymbol{B}$. The operators used in system (3.1.9) have the following definitions:

$$
rot\boldsymbol{F} = \partial_x F_y - \partial_y F_x, \quad \nabla^\perp F = (\partial_y F, \ -\partial_x F)^T
$$

$$
\nabla F = (\partial_x F, \ \partial_y F)^T, \quad \nabla \cdot \boldsymbol{F} = \partial_x F_x + \partial_y F_y
$$

we will be considering model (3.1.9) for the purposes of the work to be conducted in the following sections.

### 3.1.5  Waves in Linear MHD

The MHD equations as all hyperbolic PDEs propagate some nonlinear waves at different speeds. The Jacobian of model (3.1.9) has real eigenvalues and a complete set of eigenvectors. However, it is not a strictly hyperbolic system since some eigenvalues may coincide. In what follows, we calculate the eigenvalues of model (3.1.9) and look at the different scales we are dealing with. In order to do so, we compute the wave speeds through the calculation of the eigenvalues of the Jacobian in the direction of the normal vector $\boldsymbol{\theta}$.

The Jacobian in the direction $\boldsymbol{\theta}$, ignoring the viscosity is:

$$
\hat{T} = \begin{pmatrix}
\beta^q M^p (\boldsymbol{a} \cdot \boldsymbol{\theta}) & \gamma \beta^q M^p \theta_1 & \gamma \beta^q M^p \theta_2 & 0 & 0 \\
\dfrac{\beta^q}{\gamma M^{2-p}} \theta_1 & \beta^q M^p (\boldsymbol{a} \cdot \boldsymbol{\theta}) & 0 & -\dfrac{1}{M^{2-p}\beta^{1-q}} b_2 \theta_2 & \dfrac{1}{M^{2-p}\beta^{1-q}} b_2 \theta_1 \\
\dfrac{\beta^q}{\gamma M^{2-p}} \theta_2 & 0 & \beta^\alpha M (\boldsymbol{a} \cdot \boldsymbol{\theta}) & \dfrac{1}{M^{2-p}\beta^{1-q}} b_1 \theta_2 & -\dfrac{1}{M^{2-p}\beta^{1-q}} b_1 \theta_1 \\
0 & -\beta^q M^p b_2 \theta_2 & \beta^q M^p b_2 \theta_1 & \beta^q M^p (\boldsymbol{a} \cdot \boldsymbol{\theta}) & 0 \\
0 & \beta^q M^p b_1 \theta_2 & -\beta^q M^p b_1 \theta_1 & 0 & \beta^q M^p (\boldsymbol{a} \cdot \boldsymbol{\theta})
\end{pmatrix}
$$

We find the eigenvalues of the matrix $\hat{T}$:

- The matter wave: $\lambda_0 = u_0$
- The magnetosonic wave, which in part, is split into two groups:
  - The slow waves: $\lambda_s = u_0 \pm \left( \frac{1}{2}(V_a^2 + c^2) - V_{ac} \right)^{\frac{1}{2}}$
  - The fast waves: $\lambda_f = u_0 \pm \left( \frac{1}{2}(V_a^2 + c^2) + V_{ac} \right)^{\frac{1}{2}}$

Where: the speed of the matter wave $u_0 = M^p \beta^q (\boldsymbol{a} \cdot \boldsymbol{\theta})$, the sound speed $c^2 = M^{2p-2}\beta^{2q} \mid \boldsymbol{\theta} \mid^2$, the Alfven speed $V_a$ defined as: $V_a^2 = M^{2p-2}\beta^{2q-1}(\boldsymbol{\theta} \cdot \mathbf{b})^2$ and:

$$
V_{ac}^2 = \frac{1}{4}(V_a^2 + c^2)^2 - M^{4p-4}\beta^{4q-1}(V_a^2 c^2)
$$

In Tokamaks, the Mach number is usually in the range $]0, 1]$ whereas $\beta$ is usually in the range $[0.001, 0.2]$. A natural characteristic velocity in Tokamaks is the thermal velocity which is close to the sound velocity. Looking back at the definition of the characteristic velocity $V = \frac{u_0}{M^p \beta^q}$, this case corresponds to having $p = 1, q = 0$. To have a comparison of the scales of the eigenvalues present in the linear MHD model, we have in the case of $p = 1, q = 0$: the speed of the matter wave $u_0 = M(\boldsymbol{a} \cdot \boldsymbol{\theta})$, the sound speed $c^2 = \mid \boldsymbol{\theta} \mid^2$, the Alfven wave $V_a^2 = \frac{(\boldsymbol{\theta} \cdot \mathbf{b})^2}{\beta}$ and:

$$
V_{ac}^2 = \frac{1}{4}(\frac{(\boldsymbol{\theta} \cdot \mathbf{b})^2}{\beta} + \mid \boldsymbol{\theta}^2 \mid)^2 - \frac{(\boldsymbol{\theta} \cdot \mathbf{b})^2 \mid \boldsymbol{\theta}^2 \mid}{\beta^2}
$$

Considering the ranges of $M$ and $\beta$, we identify the following cases:

- $\beta = 0.2$ and $M = 1$: in this case, the eigenvalues are:

$$
\lambda_0 = (\boldsymbol{a} \cdot \boldsymbol{\theta})
$$

$$
\lambda_s = (\boldsymbol{a} \cdot \boldsymbol{\theta}) \pm \left( \frac{1}{2}(5(\boldsymbol{\theta} \cdot \mathbf{b}) + \mid \boldsymbol{\theta} \mid^2) - \sqrt{\frac{1}{4}(5(\boldsymbol{\theta} \cdot \mathbf{b})^2 + \mid \boldsymbol{\theta}^2 \mid)^2 - 25(\boldsymbol{\theta} \cdot \mathbf{b})^2 \mid \boldsymbol{\theta}^2 \mid} \right)^{\frac{1}{2}}
$$

$$\lambda_f = (\boldsymbol{a} \cdot \boldsymbol{\theta}) \pm \left( \frac{1}{2}(5(\boldsymbol{\theta} \cdot \mathbf{b})+ \mid \boldsymbol{\theta} \mid^2) + \sqrt{\frac{1}{4}(5(\boldsymbol{\theta} \cdot \mathbf{b})^2+ \mid \boldsymbol{\theta}^2 \mid)^2 - 25(\boldsymbol{\theta} \cdot \mathbf{b})^2 \mid \boldsymbol{\theta}^2 \mid} \right)^{\frac{1}{2}}$$

Assuming that $(\boldsymbol{a} \cdot \boldsymbol{\theta})$, $(\boldsymbol{\theta} \cdot \mathbf{b})$ and $\mid \boldsymbol{\theta}^2 \mid$, the condition number in this case, which is defined as $\lambda_{max}/\lambda_{min}$ is 3.16.

- $\beta = 0.05$ and $M = 0.05$: in this case, the eigenvalues are:

$$\lambda_0 = 0.05(\boldsymbol{a} \cdot \boldsymbol{\theta})$$

$$\lambda_s = 0.05(\boldsymbol{a} \cdot \boldsymbol{\theta}) \pm \left( \frac{1}{2}(20(\boldsymbol{\theta} \cdot \mathbf{b})+ \mid \boldsymbol{\theta} \mid^2) - \sqrt{\frac{1}{4}(20(\boldsymbol{\theta} \cdot \mathbf{b})^2+ \mid \boldsymbol{\theta}^2 \mid)^2 - 400(\boldsymbol{\theta} \cdot \mathbf{b})^2 \mid \boldsymbol{\theta}^2 \mid} \right)^{\frac{1}{2}}$$

$$\lambda_f = 0.05(\boldsymbol{a} \cdot \boldsymbol{\theta}) \pm \left( \frac{1}{2}(20(\boldsymbol{\theta} \cdot \mathbf{b})+ \mid \boldsymbol{\theta} \mid^2) + \sqrt{\frac{1}{4}(20(\boldsymbol{\theta} \cdot \mathbf{b})^2+ \mid \boldsymbol{\theta}^2 \mid)^2 - 400(\boldsymbol{\theta} \cdot \mathbf{b})^2 \mid \boldsymbol{\theta}^2 \mid} \right)^{\frac{1}{2}}$$

With the same assumption as before, the condition number in this case is 90.31.

- $\beta = 0.001$ and $M = 0.001$: in this case, the eigenvalues are:

$$\lambda_0 = 10^{-3}(\boldsymbol{a} \cdot \boldsymbol{\theta})$$

$$\lambda_s = 10^{-3}(\boldsymbol{a} \cdot \boldsymbol{\theta}) \pm \left( \frac{1}{2}(10^3(\boldsymbol{\theta} \cdot \mathbf{b})+ \mid \boldsymbol{\theta} \mid^2) - \sqrt{\frac{1}{4}(10^3(\boldsymbol{\theta} \cdot \mathbf{b})^2+ \mid \boldsymbol{\theta}^2 \mid)^2 - 10^6(\boldsymbol{\theta} \cdot \mathbf{b})^2 \mid \boldsymbol{\theta}^2 \mid} \right)^{\frac{1}{2}}$$

$$\lambda_f = 10^{-3}(\boldsymbol{a} \cdot \boldsymbol{\theta}) \pm \left( \frac{1}{2}(10^3(\boldsymbol{\theta} \cdot \mathbf{b})+ \mid \boldsymbol{\theta} \mid^2) + \sqrt{\frac{1}{4}(10^3(\boldsymbol{\theta} \cdot \mathbf{b})^2+ \mid \boldsymbol{\theta}^2 \mid)^2 - 10^6(\boldsymbol{\theta} \cdot \mathbf{b})^2 \mid \boldsymbol{\theta}^2 \mid} \right)^{\frac{1}{2}}$$

The condition number in this case is $3.1 \times 10^4$.

From the above calculation, we see that the condition number becomes larger when we are considering multiple scales as in the last case. A higher condition number deteriorates the accuracy of the iterative solver and hence the quality of the numerical solution. The fast and slow magnetosonic waves are the equivalent of acoustic waves in fluid dynamics. Actually, in the direction orthogonal to the magnetic field, the speed of propagation of the slow magnetosonic waves is zero and only the fast magnetosonic waves survive. We can see that the existence of these different waves introduces the problem of having different scales to deal with. This leads to a complexity in performing numerical simulations on model (3.1.9) as it is a difficult task to resolve the different scales [18]. Generally speaking, the MHD is solved with an implicit or semi-implicit solver in order to avoid the CFL

condition arising due to the faster scales. We suggest a solution for this issue in the next section.

## 3.2 Energy Preserving Splitting

Implicit time schemes are known to be stable without a restriction on the time step, however this type of result is valid for stable physical dynamics [9]. In this section we propose an energy preserving splitting which would allow us to decouple the different scales found in section (3.1.5) and reduce the problem of the conditioning number of the implicit scheme. We split system (3.1.9) into three parts: one with the convection-diffusion part, which deals with the slower time scales in the low Mach and low $\beta$ regimes, one with the acoustic part and one with the magnetic part, which deals with a faster time scales in the low $\beta$ regime. Note that the different contributions to the waves present in the full model (3.1.9) are being mitigated to each of the sub models, which explains the choice of the splitting. The splitting is done in the following way:

> **Three Stage Splitting**
>
> - First stage: **Convection Diffusion Step**
>
> $$\begin{cases} \partial_t p + M^p \beta^q \boldsymbol{a} \cdot \nabla p = \dfrac{(\gamma - 1)M^p\beta^q}{R_e P_r} \nabla \cdot (\nabla p) \\[3mm] \partial_t \boldsymbol{u} + M^p \beta^q \boldsymbol{a} \cdot \nabla \boldsymbol{u} = \dfrac{M^p\beta^q}{R_e}\left(\Delta \boldsymbol{u} + k\nabla(\nabla \cdot \boldsymbol{u})\right) \\[3mm] \partial_t \boldsymbol{B} + M^p \beta^q \nabla^{\perp}(\boldsymbol{a} \cdot \boldsymbol{B}^{\perp}) = -\dfrac{1}{R_m}\nabla^{\perp}(rot\boldsymbol{B}) \end{cases}$$
>
> - Second stage: **Acoustic Step**
>
> $$\begin{cases} \partial_t p + \gamma M^p \beta^q \nabla \cdot \boldsymbol{u} = 0 \\[3mm] \partial_t \boldsymbol{u} + \dfrac{\beta^q}{\gamma M^{2-p}}\nabla p = 0 \end{cases}$$
>
> - Third stage: **Magnetic Step**
>
> $$\begin{cases} \partial_t \boldsymbol{u} - \dfrac{1}{M^{2-p}\beta^{1-q}}(rot\boldsymbol{B})\mathbf{b}^{\perp} = -\dfrac{1}{M^{2-p}\beta^{1-q}}j\boldsymbol{B}^{\perp} \\[3mm] \partial_t \boldsymbol{B} + M^p \beta^q \nabla^{\perp}(\boldsymbol{u} \cdot \mathbf{b}^{\perp}) = 0 \end{cases}$$

**Remark 3.2.1.** The above mentioned splitting preserves the divergence free condition for the magnetic field at each step ($\nabla \cdot \boldsymbol{B} = 0$), given that $\nabla \cdot \boldsymbol{B} = 0$ is enforced at $t = 0$:

- For the convection-diffusion step: we see that applying the $\nabla \cdot$ (divergence) operator to the magnetic equation verifies that $\partial_t \nabla \cdot \boldsymbol{B} = 0$, keeping in mind that $\nabla \cdot (\nabla^{\perp}(rot\boldsymbol{B})) = 0$ and $\nabla \cdot (\nabla^{\perp}(\boldsymbol{a} \cdot \boldsymbol{B}^{\perp})) = 0$

- For the acoustic step: this is trivially verified.

- For the magnetic step: we apply the $\nabla \cdot$ operator to the magnetic equation, and we see that indeed $\nabla \cdot \boldsymbol{B} = 0$, as $\nabla \cdot (\nabla^{\perp}(\boldsymbol{u} \cdot \mathbf{b}^{\perp})) = 0$

In what follows, we speak about the energy conservation or dissipation in the context of model (3.1.9). The conservation of energy has an important value to

improve the stability of numerical schemes. Hence, we specify the total energy and provide the associated proof.

**Lemma 3.1.** *The energy $E$ of the system in the case of $j = 0$ and $\boldsymbol{a} = 0$ is bounded and verifies:*

$$\frac{dE}{dt} = -\frac{(\gamma - 1)M^p\beta^q}{\gamma^2 R_e P_r} \int_\Omega |\nabla p|^2 - \frac{M^{p+2}\beta^q}{R_e} \int_\Omega (|\nabla\boldsymbol{u}|^2 + k|\nabla\cdot\boldsymbol{u}|^2) - \frac{1}{\beta R_m} \int_\Omega |rot\boldsymbol{B}|^2$$

*In the case of the diffusion part is zero, which takes place if $R_e >> 1$ and $R_m >> 1$, then the energy is conserved ($\frac{dE}{dt} = 0$) and the total energy of the system is defined as:*

$$E = \int_\Omega \frac{p^2}{2\gamma^2} + \int_\Omega M^2\frac{|\boldsymbol{u}|^2}{2} + \int_\Omega \frac{|\boldsymbol{B}|^2}{2\beta}. \tag{3.2.10}$$

*Which is true assuming that $\boldsymbol{u}\cdot\boldsymbol{n}\mid_\Gamma = 0$, $\nabla\boldsymbol{u}\cdot\boldsymbol{n}\mid_\Gamma = 0$, $\boldsymbol{B}\cdot\boldsymbol{n}^\perp\mid_\Gamma = 0$ and $p\mid_\Gamma = 0$*

*Proof.* **Linear MHD:**

$$\begin{cases} \partial_t p + M^p\beta^q\boldsymbol{a}\cdot\nabla p + \gamma M^p\beta^q\nabla\cdot\boldsymbol{u} = \dfrac{(\gamma-1)M^p\beta^q}{R_e P_r}\nabla\cdot(\nabla p) \\[3mm] \partial_t\boldsymbol{u} + M^p\beta^q\boldsymbol{a}\cdot\nabla\boldsymbol{u} + \dfrac{\beta^q}{\gamma M^{2-p}}\nabla p = -\dfrac{1}{M^{2-p}\beta^{1-q}}(rot\boldsymbol{B})\mathbf{b}^\perp \\[2mm] +\frac{M^p\beta^q}{R_e}\left(\Delta\boldsymbol{u} + k\nabla(\nabla\cdot\boldsymbol{u})\right) \\[3mm] \partial_t\boldsymbol{B} + M^p\beta^q\boldsymbol{a}\cdot\nabla\boldsymbol{B} + M^p\beta^q\nabla^\perp(\boldsymbol{u}\cdot\mathbf{b}^\perp) = -\dfrac{1}{R_m}\nabla^\perp(rot\boldsymbol{B}) \end{cases} \tag{3.2.11}$$

We multiply the first equation by $\frac{p}{\gamma^2}$, the second by $M^2\boldsymbol{u}$ and the third by $\frac{\boldsymbol{B}}{\beta}$ and integrate over the domain $\Omega$:

$$\begin{cases} \partial_t \displaystyle\int_\Omega \frac{p^2}{\gamma^2} + \int_\Omega \frac{M^p\beta^q}{\gamma^2}\boldsymbol{a}\cdot\nabla p\, p + \int_\Omega \frac{M^p\beta^q}{\gamma}\nabla\cdot\boldsymbol{u}\, p = \int_\Omega \frac{(\gamma-1)M^p\beta^q}{\gamma^2 R_e P_r}\nabla\cdot(\nabla p)p \\[4mm] \partial_t \displaystyle\int_\Omega M^2\frac{\boldsymbol{u}^2}{2} + \int_\Omega M^{p+2}\beta^q(\boldsymbol{a}\cdot\nabla\boldsymbol{u})\cdot\boldsymbol{u} + \int_\Omega \frac{M^p\beta^q}{\gamma}\nabla p\cdot\boldsymbol{u} = \\[2mm] -\displaystyle\int_\Omega \frac{M^p}{\beta^{1-q}}(rot\boldsymbol{B})\mathbf{b}^\perp\cdot\boldsymbol{u} + \frac{M^{p+2}\beta^q}{R_e}\int_\Omega (\Delta\boldsymbol{u} + k\nabla(\nabla\cdot\boldsymbol{u}))\cdot\boldsymbol{u} \\[4mm] \partial_t \displaystyle\int_\Omega \frac{\boldsymbol{B}^2}{2\beta} + \int_\Omega M^p\beta^{q-1}(\boldsymbol{a}\cdot\nabla\boldsymbol{B})\cdot\boldsymbol{B} + \int_\Omega M^p\beta^{q-1}\nabla^\perp(\boldsymbol{u}\cdot\mathbf{b}^\perp)\cdot\boldsymbol{B} = \\[2mm] -\displaystyle\int_\Omega \frac{1}{R_m\beta}\nabla^\perp(rot\boldsymbol{B})\cdot\boldsymbol{B} \end{cases}$$

$$\tag{3.2.12}$$

Setting the advection component to zero ($\boldsymbol{a} = 0$) leads to:

$$
\begin{cases}
\partial_t \int_\Omega \dfrac{p^2}{\gamma^2} + \int_\Omega \dfrac{M^p \beta^q}{\gamma} \nabla \cdot \boldsymbol{u} \, p = \int_\Omega \dfrac{(\gamma-1)M^p \beta^q}{\gamma^2 R_e P_r} \nabla \cdot (\nabla p) p \\[3mm]
\partial_t \int_\Omega M^2 \dfrac{\boldsymbol{u}^2}{2} + \int_\Omega \dfrac{M^p \beta^q}{\gamma} \nabla p \cdot \boldsymbol{u} = - \int_\Omega \dfrac{M^p}{\beta^{1-q}} (rot\boldsymbol{B}) \mathbf{b}^\perp \cdot \boldsymbol{u} \\[1mm]
\quad + \dfrac{M^{p+2} \beta^q}{R_e} \int_\Omega (\Delta \boldsymbol{u} + k \nabla(\nabla \cdot \boldsymbol{u})) \cdot \boldsymbol{u} \\[4mm]
\partial_t \int_\Omega \dfrac{\boldsymbol{B}^2}{2\beta} + \int_\Omega M^p \beta^{q-1} \nabla^\perp (\boldsymbol{u} \cdot \mathbf{b}^\perp) \cdot \boldsymbol{B} = - \int_\Omega \dfrac{1}{R_m \beta} \nabla^\perp (rot\boldsymbol{B}) \cdot \boldsymbol{B}
\end{cases}
\tag{3.2.13}
$$

Using the definition of the total energy:

$$
E = \int_\Omega \frac{p^2}{2\gamma^2} + \int_\Omega M^2 \frac{|\boldsymbol{u}|^2}{2} + \int_\Omega \frac{|\boldsymbol{B}|^2}{2\beta}
\tag{3.2.14}
$$

Using (3.2.13), we write :

$$
\begin{aligned}
\frac{dE}{dt} = & - \int_\Omega \frac{M^p \beta^q}{\gamma} \nabla \cdot \boldsymbol{u} \, p - \int_\Omega \frac{M^p \beta^q}{\gamma} \nabla p \cdot \boldsymbol{u} - \int_\Omega \frac{M^p}{\beta^{1-q}} (rot\boldsymbol{B}) \mathbf{b}^\perp \cdot \boldsymbol{u} \\
& - \int_\Omega M^p \beta^{q-1} \nabla^\perp (\boldsymbol{u} \cdot \mathbf{b}^\perp) \cdot \boldsymbol{B} + \frac{(\gamma-1)M^p \beta^q}{\gamma^2 R_e P_r} \nabla \cdot (\nabla p) p \\
& + \int_\Omega \frac{M^{p+2} \beta^q}{R_e} \int_\Omega (\Delta \boldsymbol{u} + k \nabla(\nabla \cdot \boldsymbol{u})) \cdot \boldsymbol{u} - \int_\Omega \frac{1}{R_m \beta} \nabla^\perp (rot\boldsymbol{B}) \cdot \boldsymbol{B}
\end{aligned}
\tag{3.2.15}
$$

Using integration by parts for the first and the third terms of Eq. (3.2.15):

- The first term:

$$
- \int_\Omega \frac{M^p \beta^q}{\gamma} \nabla \cdot \boldsymbol{u} \, p = \int_\Omega \frac{M^p \beta^q}{\gamma} \nabla p \cdot \boldsymbol{u} - \int_\Gamma \frac{M^p \beta^q}{\gamma} p (\boldsymbol{u} \cdot \boldsymbol{n})
\tag{3.2.16}
$$

- The third term:

$$
\int_\Omega M^p \beta^{q-1} \nabla^\perp (\boldsymbol{u} \cdot \mathbf{b}^\perp) \cdot \boldsymbol{B} = \int_\Omega M^p \beta^{1-q} (rot\boldsymbol{B}) \mathbf{b}^\perp \cdot \boldsymbol{u} - \int_\Gamma M^p \beta^{q-1} (\boldsymbol{u} \cdot \mathbf{b}^\perp)(\boldsymbol{B} \cdot \boldsymbol{n}^\perp)
\tag{3.2.17}
$$

Where $\Gamma$ is the boundary of $\Omega$. $\boldsymbol{n}$ is the outward unit vector normal to $\Gamma$. We assume that $\boldsymbol{u} \cdot \boldsymbol{n}\mid_\Gamma = 0$ and $\boldsymbol{B} \cdot \boldsymbol{n}^\perp \mid_\Gamma = 0$. Using the above mentioned remarks,

we get:

$$\frac{dE}{dt} = \frac{(\gamma - 1)M^p \beta^q}{\gamma^2 R_e P_r} \int_\Omega \nabla \cdot (\nabla p)p + \frac{M^{p+2}\beta^q}{R_e} \int_\Omega (\Delta \boldsymbol{u} + k\nabla(\nabla \cdot \boldsymbol{u})) \cdot \boldsymbol{u}$$
$$- \frac{1}{R_m \beta} \int_\Omega \nabla^\perp (rot\boldsymbol{B}) \cdot \boldsymbol{B} \tag{3.2.18}$$

We use integration by parts for each term of Eq (3.2.18) in the following manner:

- The first term:

$$\frac{(\gamma - 1)M^p \beta^q}{\gamma^2 R_e P_r} \int_\Omega \nabla \cdot (\nabla p)p = -\frac{(\gamma - 1)M^p \beta^q}{\gamma^2 R_e P_r} \int_\Omega (\nabla p)^2$$
$$+ \frac{(\gamma - 1)M^p \beta^q}{\gamma^2 R_e P_r} \int_\Gamma (\nabla p \cdot \boldsymbol{n})p \tag{3.2.19}$$

- The second term:

$$\frac{M^{p+2}\beta^q}{R_e} \int_\Omega (\Delta \boldsymbol{u} + k\nabla(\nabla \cdot \boldsymbol{u}))\boldsymbol{u} = -\frac{M^{p+2}\beta^q}{R_e} \int_\Omega (|\nabla \boldsymbol{u}|^2 + k|\nabla \cdot \boldsymbol{u}|^2)$$
$$+ \frac{M^{p+2}\beta^q}{R_e} \int_\Gamma (\nabla \boldsymbol{u}(\nabla \boldsymbol{u} \cdot \boldsymbol{n}) + k(\nabla \cdot \boldsymbol{u})(\boldsymbol{u} \cdot \boldsymbol{n})) \tag{3.2.20}$$

- The third term:

$$-\frac{1}{R_m \beta} \int_\Omega \nabla^\perp (rot\boldsymbol{B})\boldsymbol{B} = -\frac{1}{\beta R_m} \int_\Omega |rot\boldsymbol{B}|^2 + \frac{1}{\beta R_m} \int_\Gamma rot\boldsymbol{B}(\boldsymbol{B} \cdot \boldsymbol{n}^\perp) \tag{3.2.21}$$

Using the previous assumptions: $\boldsymbol{u} \cdot \boldsymbol{n}\mid_\Gamma = 0$, $\nabla \boldsymbol{u} \cdot \boldsymbol{n}\mid_\Gamma = 0$, $\boldsymbol{B} \cdot \boldsymbol{n}^\perp \mid_\Gamma = 0$ and also $p\mid_\Gamma = 0$, we obtain:

$$\frac{dE}{dt} = -\frac{(\gamma - 1)M^p \beta^q}{\gamma^2 R_e P_r} \int_\Omega |\nabla p|^2 - \frac{M^{p+2}\beta^q}{R_e} \int_\Omega (|\nabla \boldsymbol{u}|^2 + k|\nabla \cdot \boldsymbol{u}|^2) - \frac{1}{\beta R_m} \int_\Omega |rot\boldsymbol{B}|^2 \tag{3.2.22}$$

This result also proves that the physical energy associated with the linear MHD model (3.1.9) is conserved in the ideal case $\eta = \nu = 0$, which corresponds to infinite Reynolds numbers ($R_m$ and $R_e$), which corresponds to no diffusion. $\square$

In the following, we study each step of the energy preserving splitting, namely, the linear acoustic step, the linear magnetic step and the convection-diffusion step with no diffusion for the velocity. For each step, we present the relevant invariants and detail the spatial and temporal discretization schemes that we use.

We end each substep with numerical results obtained through the implementation of appropriate test cases.

## 3.3 Linear Acoustic Step with Constant Coefficients

The model for the acoustic part which is a hyperbolic system used to describe the acoustic waves linked to the hydrodynamic pressure defined on $\Omega = [0,1] \times [0,1]$, $t \in [0,T]$, where t is the time and T is the final time, at the continuous level is given by:

$$
\begin{cases}
\partial_t p + \gamma M^p \beta^q \nabla \cdot \boldsymbol{u} = 0, & \Omega \times [0,T] \\[4mm]
\partial_t \boldsymbol{u} + \dfrac{\beta^q}{\gamma M^{2-p}} \nabla p = 0, & \Omega \times [0,T]
\end{cases}
\tag{3.3.23}
$$

with adequate boundary conditions which are defined later on. $\boldsymbol{u}$ is the velocity field and $p$ is the pressure. The constants were defined in detail in section (3.1.3). The divergence operator is defined as: $\nabla \cdot \boldsymbol{u} = \partial_x u_x + \partial_y u_y$ and the gradient operator is defined as: $\nabla p = (\partial_x p, \ \partial_y p)^T$. The system conserves energy as specified in the following lemma:

**Lemma 3.2.** *The total energy of system (3.3.23) is conserved and is given by:*

$$
E = \int_\Omega \left( \frac{p^2}{2\gamma^2} + M^2 \frac{| \boldsymbol{u} |^2}{2} \right)
$$

*assuming that* $\boldsymbol{u} \cdot \boldsymbol{n} \mid = 0$ *on the boundary.*

*Proof.* We multiply the pressure (first) equation of model (3.3.23) by $\frac{p}{\gamma^2}$ and the velocity (second) equation by $M^2 \boldsymbol{u}$ and integrate over the domain $\Omega$ we obtain:

$$
\int_\Omega \frac{p}{\gamma^2} \partial_t p + \int_\Omega \frac{M^p \beta^q}{\gamma} p \nabla \cdot \boldsymbol{u} = 0
\tag{3.3.24}
$$

and

$$
\int_\Omega M^2 \boldsymbol{u} \cdot \partial_t \boldsymbol{u} + \int_\Omega \frac{M^p \beta^q}{\gamma} \boldsymbol{u} \cdot \nabla p = 0.
\tag{3.3.25}
$$

Using the definition of the total energy:

$$
E = \int_\Omega \left( \frac{p^2}{2\gamma^2} + M^2 \frac{| \boldsymbol{u} |^2}{2} \right).
\tag{3.3.26}
$$

Hence:

$$E = -\int_{\Omega} \frac{M^p \beta^q}{\gamma} p \nabla \cdot \boldsymbol{u} - \int_{\Omega} \frac{M^p \beta^q}{\gamma} \boldsymbol{u} \cdot \nabla p \qquad (3.3.27)$$

Using integration by parts for the first term of Eq. (3.3.27):

$$-\int_{\Omega} \frac{M^p \beta^q}{\gamma} \nabla \cdot \boldsymbol{u} \, p = \int_{\Omega} \frac{M^p \beta^q}{\gamma} \nabla p \cdot \boldsymbol{u} - \int_{\Gamma} \frac{M^p \beta^q}{\gamma} p(\boldsymbol{u} \cdot \boldsymbol{n}) \qquad (3.3.28)$$

$\Gamma$ is the boundary of $\Omega$ and $\boldsymbol{n}$ is the outward unit vector normal to $\Gamma$. We assume that $\boldsymbol{u} \cdot \boldsymbol{n} \mid_{\Gamma} = 0$. Summing the two equations we obtain that:

$$\partial_t \left( \int_{\Omega} \frac{p^2}{2\gamma^2} + \int_{\Omega} M^2 \frac{\mid \boldsymbol{u} \mid^2}{2} \right) = 0.$$

$\square$

The other invariant property for the linear acoustic system is stated in the following lemma:

**Lemma 3.3.** *The total vorticity defined as $w = rot(\boldsymbol{u})$ is conserved:*

$$\partial_t w = \partial_t rot(\boldsymbol{u}) = 0.$$

*Where $rot\boldsymbol{u} = -\partial_y u_x + \partial_x u_y$.*

*Proof.* We obtain the vorticity equation via applying the rot operator to the velocity equation of model (3.3.23): $\partial_t rot(\boldsymbol{u}) + \frac{1}{\gamma M^{2-p}} rot(\nabla p) = 0$ and as $rot(\nabla p) = 0$, then $\partial_t rot(\boldsymbol{u}) = \partial_t w = 0$. $\square$

In line with the wave analysis done on the linear MHD model (3.1.9), we outline the wave structure of the linear acoustic step to show that there are also different scales within this model.

## 3.3.1 Wave Structure of the Linear Acoustic Step

To analyse the wave structure of the acoustic step, we compute the wave speeds through the calculation of the eigenvalues of the Jacobian in the direction of the normal vector $\boldsymbol{\theta}$. The Jacobian is:

$$\hat{T} = \begin{pmatrix} 0 & \gamma \beta^q M^p \theta_1 & \gamma \beta^q M^p \theta_2 \\ \frac{\beta^q}{\gamma M^{2-p}} \theta_1 & 0 & 0 \\ \frac{\beta^q}{\gamma M^{2-p}} \theta_2 & 0 & 0 \end{pmatrix}.$$

We find the eigenvalues of the matrix $\hat{T}$:

$$\lambda_0 = 0, \quad \lambda_1 = \beta^q M^{p-1} \parallel \boldsymbol{\theta} \parallel^2, \quad \lambda_2 = -\beta^q M^{p-1} \parallel \boldsymbol{\theta} \parallel^2$$

This result shows the different waves present in the acoustic step: the acoustic wave and the stationary shear wave.

## 3.3.2 The Spatial Discretization and the associated de Rham Sequence

In order to choose the correct spaces for model (3.3.23) that ensure the exact preservation of the invariant quantities at the discrete level, we need to refer to the 2D de Rham sequences introduced earlier in section (2.3):

- The first choice comes as a result of looking at the following de Rham sequence:

de Rham Sequence 1

$$
\begin{array}{ccccc}
 & \nabla & & rot & \\
H^1(\Omega) & \longrightarrow & H(rot;\Omega) & \longrightarrow & L^2(\Omega) \\
 & & & & \\
\Pi_0 \downarrow & & \Pi_1 \downarrow & & \Pi_3 \downarrow \\
 & \nabla & & rot & \\
V_0 & \longrightarrow & V_1 & \longrightarrow & V_3 \\
 & & & & \\
\mathcal{S}^{p,p} & & \begin{pmatrix} \mathcal{S}^{p-1,p} \\ \mathcal{S}^{p,p-1} \end{pmatrix} & & \mathcal{S}^{p-1,p-1}
\end{array}
$$

The definition of the involved operators and the respective Sobolev spaces are found in section (2.3). If we consider taking $p \in H^1(\Omega)$ then we can see clearly from the above mentioned de Rham sequence, that we can apply the gradient "$\nabla$" operator on a scalar field living in $H^1(\Omega)$ space. The application of the gradient operator on a scalar field living in $H^1(\Omega)$ space implies that the resultant vector field living in $H(rot;\Omega)$. Hence, we need to have $\boldsymbol{u} \in H(rot;\Omega)$. Looking at model (3.3.23) we see that we have the divergence "$\nabla \cdot$" operator acting on the velocity field, which is not permitted. To go around this, we find a variational formulation for model (3.3.23) that

makes use of the dual of "$\nabla\cdot$" which is "$-\nabla$". Take a test function $q \in H^1(\Omega)$ and take the dot product with the pressure equation. We also take a test function $\boldsymbol{v} \in H(rot;\Omega)$ and take the dot product with the velocity equation and integrate over the domain $\Omega$, we get:

$$
\begin{cases}
\partial_t \int_\Omega pq + \gamma M^p \int_\Omega \nabla \cdot \boldsymbol{u}q = 0, \quad p,q \in H^1(\Omega) \\[3mm]
\partial_t \int_\Omega \boldsymbol{u} \cdot \boldsymbol{v} + \dfrac{1}{\gamma M^{2-p}} \int_\Omega \nabla p \cdot \boldsymbol{v} = 0, \quad \boldsymbol{u}, \boldsymbol{v} \in H(rot;\Omega)
\end{cases}
\tag{3.3.29}
$$

We integrate the term $\int_\Omega \nabla \cdot \boldsymbol{u}q$ by parts using Green's Formula for the first term of Eq. (3.3.27):

$$
\frac{M^p \beta^q}{\gamma} \int_\Omega \nabla \cdot \boldsymbol{u} \, q = -\frac{M^p \beta^q}{\gamma} \int_\Omega \nabla q \cdot \boldsymbol{u} + \frac{M^p \beta^q}{\gamma} \int_\Gamma q \, (\boldsymbol{u} \cdot \boldsymbol{n})
\tag{3.3.30}
$$

where $\Gamma$ is the boundary of $\Omega$ and $\boldsymbol{n}$ is the outward unit vector normal to $\Gamma$. For simplicity, we assume that $\boldsymbol{u} \cdot \boldsymbol{n} \mid_\Gamma = 0$. We get:

$$
\begin{cases}
\partial_t \int_\Omega pq - \dfrac{M^p \beta^q}{\gamma} \int_\Omega \nabla q \cdot \boldsymbol{u} = 0 \\[3mm]
\partial_t \int_\Omega \boldsymbol{u} \cdot \boldsymbol{v} + \dfrac{1}{\gamma M^{2-p}} \int_\Omega \nabla p \cdot \boldsymbol{v} = 0
\end{cases}
\tag{3.3.31}
$$

Hence, we can write the variational formulation for model (3.3.23) considering the space pair $H(rot;\Omega) - H^1(\Omega)$ at the continuous level in the following manner:

---

**Variational Formulation 1**

Find $(\boldsymbol{u}, p) \in H(rot,\Omega) \times H^1(\Omega)$ such that:

$$
\begin{cases}
\partial_t \int_\Omega pq - \dfrac{M^p \beta^q}{\gamma} \int_\Omega \nabla q \cdot \boldsymbol{u} = 0 \quad \forall q \in H^1(\Omega) \\[3mm]
\partial_t \int_\Omega \boldsymbol{u} \cdot \boldsymbol{v} + \dfrac{1}{\gamma M^{2-p}} \int_\Omega \nabla p \cdot \boldsymbol{v} = 0 \quad \forall \boldsymbol{v} \in H(rot;\Omega)
\end{cases}
\tag{3.3.32}
$$

---

In order to discretize the above variational formulation, we substitute $\boldsymbol{u}, \boldsymbol{v}, p, q$ with their discrete counterparts, and the discrete variational formulation writes:

> **Discrete Variational Formulation 1**
>
> Find $(\boldsymbol{u}_h, p_h) \in V_1 \times V_0$ such that:
>
> $$\begin{cases} \partial_t \int_\Omega p_h q_h - \dfrac{M^p \beta^q}{\gamma} \int_\Omega \nabla q_h \cdot \boldsymbol{u}_h = 0 & \forall q_h \in V_0 \\[2em] \partial_t \int_\Omega \boldsymbol{u}_h \cdot \boldsymbol{v}_h + \dfrac{1}{\gamma M^{2-p}} \int_\Omega \nabla p_h \cdot \boldsymbol{v}_h = 0 & \forall \boldsymbol{v}_h \in V_1 \end{cases}$$
>
> (3.3.33)

Note that the second Eq. of (3.3.33) means that $\partial_t \boldsymbol{u}_h + \frac{1}{\gamma M^{2-p}} \nabla p_h \in V_1$ is $L^2$ orthogonal to $V_1$ and hence this Eq. could be written equivalently in strong form. The assembly of the discrete fields $\boldsymbol{u}_h, \boldsymbol{v}_h$ and $p_h, q_h$ is done in the following way:

- $\boldsymbol{u}_h, \boldsymbol{v}_h \in V_1$, are defined in the following manner:

$$\boldsymbol{u}_h(\boldsymbol{x}) = \sum_{\boldsymbol{j}=1}^{N_1} u_{\boldsymbol{j}} \boldsymbol{\phi}_{\boldsymbol{j}}^1(\boldsymbol{x}), \quad \boldsymbol{v}_h(\boldsymbol{x}) = \sum_{\boldsymbol{i}=1}^{N_1} v_{\boldsymbol{i}} \boldsymbol{\phi}_{\boldsymbol{i}}^1(\boldsymbol{x})$$

  where we have the multi-indices $\boldsymbol{i} = (i_1, i_2)$ and $\boldsymbol{j} = (j_1, j_2)$, and $\boldsymbol{\phi}_{\boldsymbol{i}}^1$ stands for the test basis function defined on $V_1$ as defined in section (2.3). Likewise, $\boldsymbol{\phi}_{\boldsymbol{j}}^1$ stands for the trial basis function defined on $V_1$. $u_{\boldsymbol{j}}, v_{\boldsymbol{i}}$ are the spline coefficients.

- $p_h, q_h \in V_0$, are defined as:

$$p_h(\boldsymbol{x}) = \sum_{\boldsymbol{j}=1}^{N_0} p_{\boldsymbol{j}} \phi_{\boldsymbol{j}}^0(\boldsymbol{x}), \quad q_h(\boldsymbol{x}) = \sum_{\boldsymbol{i}=1}^{N_0} q_{\boldsymbol{i}} \phi_{\boldsymbol{i}}^0(\boldsymbol{x})$$

  where $\phi_{\boldsymbol{i}}^0$ stands for the test basis functions defined on $V_0$ and $\phi_{\boldsymbol{j}}^0$ stands for the trial basis functions defined on $V_0$. $p_{\boldsymbol{j}}, q_{\boldsymbol{i}}$ are the spline coefficients.

In order to complete the method, we need to discretize in time as well. Before doing so, we introduce the second formulation and after that we detail the discretization in time for both formulations.

- The second choice comes as a result of inspecting the second de Rham sequence in 2D:

de Rham Sequence 2

$$
\begin{array}{ccccc}
 & \nabla^{\perp} & & \nabla\cdot & \\
H^1(\Omega) & \longrightarrow & H(div,\Omega) & \longrightarrow & L^2(\Omega) \\
\end{array}
$$

$$
\Pi_0\downarrow \qquad\qquad \Pi_2\downarrow \qquad\qquad \Pi_3\downarrow
$$

$$
\begin{array}{ccccc}
 & \nabla^{\perp} & & \nabla\cdot & \\
V_0 & \longrightarrow & V_2 & \longrightarrow & V_3 \\
\end{array}
$$

$$
\mathcal{S}^{p,p} \qquad \begin{pmatrix} \mathcal{S}^{p,p-1} \\ \mathcal{S}^{p-1,p} \end{pmatrix} \qquad \mathcal{S}^{p-1,p-1}
$$

The definition of the involved operators and the respective Sobolev spaces are found in section (2.3).

If we consider taking $\boldsymbol{u} \in H(div;\Omega)$ then we can see clearly from the above mentioned de Rham sequence, that we can apply the divergence ($\nabla\cdot$) operator on a vector field living in $H(div;\Omega)$. The application of the divergence operator on a vector field living in $H(div;\Omega)$ implies that the resultant scalar field living in $L^2(\Omega)$. Hence, we need to have $p \in L^2(\Omega)$. Looking at model (3.3.23) we see that we have the gradient ($\nabla$) operator acting on the pressure field, which is not permitted, considering the de Rham sequence we are operating within. To go around this, we find a variational formulation for model (3.3.23) that makes use of the dual of "$\nabla$" which is "$-\nabla\cdot$". We take a test function $q \in L^2(\Omega)$ and take the dot product with the pressure equation. We also take a test function $\boldsymbol{v} \in H(div;\Omega)$ and take the dot product with the velocity equation and integrate over the domain $\Omega$, we get:

$$
\begin{cases}
\partial_t \int_{\Omega} pq + \gamma M^p \int_{\Omega} \nabla \cdot \boldsymbol{u}q = 0 \\[4mm]
\partial_t \int_{\Omega} \boldsymbol{u} \cdot \boldsymbol{v} + \dfrac{1}{\gamma M^{2-p}} \int_{\Omega} \nabla p \cdot \boldsymbol{v} = 0
\end{cases}
\tag{3.3.34}
$$

We integrate the term $\int_\Omega \nabla p \cdot \boldsymbol{v} = 0$ by parts using Green's formula for the first term of Eq. (3.3.27):

$$\frac{1}{\gamma M^{2-p}} \int_\Omega \nabla p \cdot \boldsymbol{v} = -\frac{1}{\gamma M^{2-p}} \int_\Omega p \nabla \cdot \boldsymbol{v} + \frac{1}{\gamma M^{2-p}} \int_\Gamma p(\boldsymbol{n} \cdot \boldsymbol{v})$$

where $\Gamma$ is the boundary of $\Omega$ and $\boldsymbol{n}$ is the outward unit vector normal to $\Gamma$. For simplicity, we assume that $p \mid_\Gamma = 0$. We get:

$$
\begin{cases}
\partial_t \int_\Omega pq + \dfrac{M^p \beta^q}{\gamma} \int_\Omega \nabla \cdot \boldsymbol{u} q = 0 \\[4mm]
\partial_t \int_\Omega \boldsymbol{u} \cdot \boldsymbol{v} - \dfrac{1}{\gamma M^{2-p}} \int_\Omega p \nabla \cdot \boldsymbol{v} = 0
\end{cases}
\tag{3.3.35}
$$

The variational formulation for the space pair $H(div; \Omega) - L^2(\Omega)$ at the continuous level:

---

**Variational Formulation 2**

Find $(\boldsymbol{u}, p) \in H(div; \Omega) \times L^2(\Omega)$ such that:

$$
\begin{cases}
\partial_t \int_\Omega pq + \dfrac{M^p \beta^q}{\gamma} \int_\Omega \nabla \cdot \boldsymbol{u} q = 0 \quad \forall q \in L^2(\Omega) \\[4mm]
\partial_t \int_\Omega \boldsymbol{u} \cdot \boldsymbol{v} - \dfrac{1}{\gamma M^{2-p}} \int_\Omega p \nabla \cdot \boldsymbol{v} = 0 \quad \forall \boldsymbol{v} \in H(div; \Omega)
\end{cases}
\tag{3.3.36}
$$

---

And to discretize the above variational formulation, we substitute $\boldsymbol{u}, \boldsymbol{v}, p, q$ with their discrete counterparts, and the discrete variational formulation writes:

---

**Discrete Variational Formulation 2**

Find $(\boldsymbol{u}_h, p_h) \in V_2 \times V_3$ such that:

$$
\begin{cases}
\partial_t \int_\Omega p_h q_h + \dfrac{M^p \beta^q}{\gamma} \int_\Omega \nabla \cdot \boldsymbol{u}_h q_h = 0 \quad \forall q_h \in V_3 \\[4mm]
\partial_t \int_\Omega \boldsymbol{u}_h \cdot \boldsymbol{v}_h - \dfrac{1}{\gamma M^{2-p}} \int_\Omega p_h \nabla \cdot \boldsymbol{v}_h = 0 \quad \forall \boldsymbol{v}_h \in V_2
\end{cases}
\tag{3.3.37}
$$

---

The first Eq. of (3.3.37) implies that $\partial_t p_h + \frac{M^p \beta^q}{\gamma} \nabla \cdot \boldsymbol{u}_h \in V_1$ is $L^2$ orthogonal to $V_3$ and hence this Eq. could be written equivalently in strong form. The assembly of the discrete fields $\boldsymbol{u}_h, \boldsymbol{v}_h$ and $p_h, q_h$ is done in the following way:

- $\boldsymbol{u}_h, \boldsymbol{v}_h \in V_2$, are defined in the following manner:

$$\boldsymbol{u}_h(\boldsymbol{x}) = \sum_{\boldsymbol{j}=1}^{N_2} u_{\boldsymbol{j}} \boldsymbol{\phi}_{\boldsymbol{j}}^2(\boldsymbol{x}), \quad \boldsymbol{v}_h(\boldsymbol{x}) = \sum_{\boldsymbol{i}=1}^{N_2} v_{\boldsymbol{i}} \boldsymbol{\phi}_{\boldsymbol{i}}^2(\boldsymbol{x})$$

where we have the multi-indices $\boldsymbol{i} = (i_1, i_2)$ and $\boldsymbol{j} = (j_1, j_2)$ and $\boldsymbol{\phi}_{\boldsymbol{i}}^2$ stands for the test basis function defined on $V_2$ as defined in section (2.3). Likewise, $\boldsymbol{\phi}_{\boldsymbol{j}}^2$ stands for the trial basis function defined on $V_2$. $u_{\boldsymbol{j}}, v_{\boldsymbol{i}}$ are the spline coefficients.

- $p_h, q_h \in V_3$, are defined as:

$$p_h(\boldsymbol{x}) = \sum_{\boldsymbol{j}=1}^{N_3} p_{\boldsymbol{j}} \phi_{\boldsymbol{j}}^3(\boldsymbol{x}), \quad q_h(\boldsymbol{x}) = \sum_{\boldsymbol{i}=1}^{N_3} q_{\boldsymbol{i}} \phi_{\boldsymbol{i}}^3(\boldsymbol{x})$$

where $\phi_{\boldsymbol{i}}^3$ stands for the test basis functions defined on $V_3$ and $\phi_{\boldsymbol{j}}^3$ stands for the trial basis functions defined on $V_3$. $p_{\boldsymbol{j}}, q_{\boldsymbol{i}}$ are the spline coefficients.

### 3.3.3 Discretization in Time

We choose an implicit scheme for the acoustic step, which can be made explicit if we want to. We use a classical $\theta$-scheme for the time discretization. A special case of the $\theta$-scheme is when $\theta = 0.5$, also known as Cranck-Nicolson (CN) scheme, which is a second order in time scheme. Applying the $\theta$-scheme to the above mentioned discrete variational formulations, we get the following two systems, which are discrete in space and time to solve:

> **System 1**
>
> We solve for $(\boldsymbol{u}_h^{n+1}, p_h^{n+1})$, where $(\boldsymbol{u}_h, p_h) \in V_1 \times V_0$ such that:
>
> $$\begin{cases} \displaystyle \int_\Omega p_h^{n+1} q_h - \theta \Delta t M^p \gamma \int_\Omega \boldsymbol{u}_h^{n+1} \cdot \nabla q_h = \int_\Omega p_h^n q_h \\ \displaystyle +(1-\theta)\Delta t M^p \gamma \int_\Omega \boldsymbol{u}_h^n \cdot \nabla q_h \qquad \forall q_h \in V_0 \\[2em] \displaystyle \int_\Omega \boldsymbol{u}_h^{n+1} \cdot \boldsymbol{v}_h + \theta \Delta t \frac{1}{\gamma M^{2-p}} \int_\Omega \nabla p_h^{n+1} \cdot \boldsymbol{v}_h = \int_\Omega \boldsymbol{u}_h^n \cdot \boldsymbol{v}_h \\ \displaystyle -(1-\theta)\Delta t \frac{1}{\gamma M^{2-p}} \int_\Omega \nabla p_h^n \cdot \boldsymbol{v}_h \qquad \forall \boldsymbol{v}_h \in V_1 \end{cases}$$

> **System 2**
>
> We solve for $(\boldsymbol{u}_h^{n+1}, p_h^{n+1})$, where $(\boldsymbol{u}_h, p_h) \in V_2 \times V_3$ such that:
>
> $$\begin{cases} \displaystyle \int_\Omega p_h^{n+1} q_h + \theta \Delta t M^p \gamma \int_\Omega \nabla \cdot \boldsymbol{u}_h^{n+1} q_h = \int_\Omega p_h^n q_h \\ \displaystyle -(1-\theta)\Delta t M^p \gamma \int_\Omega \nabla \cdot \boldsymbol{u}_h^n q_h \qquad \forall q_h \in V_3 \\[2em] \displaystyle \int_\Omega \boldsymbol{u}_h^{n+1} \cdot \boldsymbol{v}_h - \theta \Delta t \frac{1}{\gamma M^{2-p}} \int_\Omega p_h^{n+1} \nabla \cdot \boldsymbol{v}_h = \int_\Omega \boldsymbol{u}_h^n \cdot \boldsymbol{v}_h \\ \displaystyle +(1-\theta)\Delta t \frac{1}{\gamma M^{2-p}} \int_\Omega p_h^n \nabla \cdot \boldsymbol{v}_h \qquad \forall \boldsymbol{v}_h \in V_2 \end{cases}$$

**Remark 3.3.1.** As mentioned before, setting $\theta = 0.5$ leads to a second order in time scheme. If we take $\theta = 1$, the scheme reduces to a fully implicit scheme. Whereas choosing $\theta = 0$ reduces the schemes to a fully explicit scheme. In the implicit scheme, we solve the two scales at the same time, the acoustic wave and the stationary shear wave.

### 3.3.4 Systems' Reduction

We propose two ways to reduce system 1 and system 2:

**Reduction 1:** we consider the formulation where we have $p_h \in V_0$ and $\boldsymbol{u}_h \in V_1$ with vanishing Neumann boundary conditions as specified before. In this case, we

solve the velocity (second) equation of model (3.3.23) strongly as suggested before:

$$\boldsymbol{u}_h^{n+1} + \theta\Delta t \left[\frac{1}{\gamma M^{2-p}}\nabla\right] p_h^{n+1} = \boldsymbol{u}_h^n - (1-\theta)\Delta t \left[\frac{1}{\gamma M^{2-p}}\nabla\right] p_h^n \qquad (3.3.38)$$

We use the term strong form here in the sense that the equation is solved on the coefficients level, since the associated de Rham sequence is respected at the discrete level without having to use the weak form. One can see that since $p_h \in V_0$, then $\nabla p_h \in V_1$ which reiterates the fact that the velocity (second) equation is correctly posed. We take the pressure (first) equation weakly because applying the divergence on $\boldsymbol{u}_h$ which is in $V_1$ is not allowed, so we will need to integrate the term that involves the divergence by parts, and hence the usage of the weak form. For that we introduce a test function $q_h \in V_0$, take the dot product with the pressure equation and integrate over the domain $\Omega$, we obtain:

$$\int_\Omega p_h^{n+1} q_h + \theta\Delta t M^p \gamma \int_\Omega \nabla\cdot\boldsymbol{u}_h^{n+1} q_h = \int_\Omega p_h^n q_h - (1-\theta)\Delta t M^p \int_\Omega \nabla\cdot\boldsymbol{u}_h^n q_h. \quad (3.3.39)$$

Integrating by parts the terms $\theta\Delta t M^p \gamma \int_\Omega \nabla\cdot\boldsymbol{u}_h^{n+1} q_h$ and $-(1-\theta)\Delta t M^p \int_\Omega \nabla\cdot\boldsymbol{u}_h^n q_h$, we obtain:

$$\int_\Omega p_h^{n+1} q - \theta\Delta t M^p \gamma \int_\Omega \boldsymbol{u}_h^{n+1}\cdot\nabla q_h = \int_\Omega p_h^n q_h + (1-\theta)\Delta t M^p \int_\Omega \boldsymbol{u}_h^n\cdot\nabla q_h. \quad (3.3.40)$$

Since the equation on $\boldsymbol{u}$ (3.3.38) is strong we substitute for $\boldsymbol{u}^{n+1}$ in Eq. (3.3.40):

$$A(p_h, q_h) = \int_\Omega p_h^{n+1} q_h + \theta^2\Delta t^2 \frac{1}{M^{2(1-p)}} \int_\Omega \nabla p_h^{n+1}\cdot\nabla q_h = b(q_h) \qquad (3.3.41)$$

with

$$b(q_h) = \int_\Omega p_h^n q_h + \Delta t M^p \gamma \int_\Omega \boldsymbol{u}_h^n\cdot\nabla q_h - \theta(1-\theta)\Delta t \frac{1}{M^{2(1-p)}} \int_\Omega \nabla p_h^n\cdot\nabla q_h \quad (3.3.42)$$

we obtain at the end:

> **System 3**
>
> - At first we solve for $p_h^{n+1} \in V_0$ from the weak formulation:
>
> $$A(p_h^{n+1}, q_h) = b(q_h), \quad \forall q_h \in V_0$$
>
> - Once this is obtained, we compute $\boldsymbol{u}_h^{n+1} \in V_1$ from the strong form:
>
> $$\boldsymbol{u}_h^{n+1} = -\theta \Delta t \left[\frac{\beta^q}{\gamma M^{2-p}}\nabla\right] p_h^{n+1} + \boldsymbol{u}_h^n - (1-\theta)\Delta t^2 \left[\frac{\beta^q}{\gamma M^{2-p}}\nabla\right] p_h^n$$
>
> where:
>
> $$A(p_h, q_h) = \int_\Omega p_h^{n+1} q_h + \theta^2 \Delta t^2 \frac{1}{M^{2(1-p)}} \int_\Omega \nabla p_h^{n+1} \cdot \nabla q_h$$
>
> and
>
> $$b(q_h) = \int_\Omega p_h^n q_h + \Delta t M^p \gamma \int_\Omega \boldsymbol{u}_h^n \cdot \nabla q_h - \theta(1-\theta)\Delta t \frac{1}{M^{2(1-p)}} \int_\Omega \nabla p_h^n \cdot \nabla q_h$$

and written in a matrix form:

> **Matrix Form 1**
>
> $$\left(M_0 + \frac{\theta^2 \Delta t^2}{M^{2(1-p)}} \mathcal{G}^T M_0 \mathcal{G}\right) \boldsymbol{\mathcal{P}}^{n+1} = \left(M_0 - \theta(1-\theta)\Delta t \frac{1}{M^{2(1-p)}} \mathcal{G}^T M_0 \mathcal{G}\right) \boldsymbol{\mathcal{P}}^n$$
> $$+ \Delta t M^p \gamma \mathcal{G}^T M_1 \boldsymbol{\mathcal{U}}^n$$
>
> $$\boldsymbol{\mathcal{U}}^{n+1} + \theta \Delta t \frac{1}{\gamma M^{2-p}} \mathcal{G} \boldsymbol{\mathcal{P}}^{n+1} = \boldsymbol{\mathcal{U}}^n - (1-\theta)\Delta t \frac{1}{\gamma M^{2-p}} \mathcal{G} \boldsymbol{\mathcal{P}}^n$$
>
> where $M_0 = ((\int_\Omega \phi_i^0 \phi_j^0 d\boldsymbol{x}))_{i,j}$ is the mass matrix in $V_0$ and $M_1 = ((\int_\Omega \phi_i^1 \cdot \phi_j^1 d\boldsymbol{x}))_{i,j}$ is the mass matrix in $V_1$. $\boldsymbol{\mathcal{U}}$ and $\boldsymbol{\mathcal{P}}$ are the vectors of spline coefficients. $\mathcal{G}$ is the discrete gradient operator as defined in section (2.4).

In this algorithm we apply the gradient operator to $p$ which is in $H^1$. Hence, by construction of the operator, applying the rot leads to the conservation of vorticity in time because $\mathcal{R}(\mathcal{G}) = 0$, where $\mathcal{R}$ is the discrete rot operator.

**Remark 3.3.2.** Looking at "Matrix Form 1" one can see that there are a few advantages to using this reduction in comparison to the form derived previously. To start with, we can see that in this case, one only needs to invert a matrix of one variable (the pressure) whereas previously, we had to invert a matrix of three variables (one for the pressure and two for each component of the velocity). We also note that such formulation is not possible in the context of classical FE as the velocity equation would have needed to be solved weakly. On top of that, the vorticity equation is preserved exactly at the discrete level in comparison to a classical FE formulation. Lastly, referring back to the wave analysis made on the acoustic step, we can see that in the case of "Matrix Form 1", we have only one scale to resolve, whereas we had the two scales present before, hence the condition number of the resultant matrix is smaller in the case of using "Matrix Form 1".

**Reduction 2:** we consider the formulation where we have $p_h \in V_3$ and $\boldsymbol{u}_h \in V_2$ with vanishing Neumann boundary conditions as specified before. In this case, the pressure (first) equation of system (3.3.23) is solved strongly as suggested earlier:

$$p_h^{n+1} + \theta \Delta t \left[ M^p \gamma \nabla \cdot \right] \boldsymbol{u}_h^{n+1} = p_h^n - (1-\theta) \Delta t \left[ M^p \gamma \nabla \cdot \right] \boldsymbol{u}_h^n \tag{3.3.43}$$

where $\nabla \cdot$ is the discrete divergence operator. Since $\boldsymbol{u}_h \in V_2$ we see that $\nabla \cdot \boldsymbol{u}_h \in V_3$, which confirms that the pressure equation is correctly posed. We consider the first (velocity) equation weakly. For that we introduce a test function $\boldsymbol{v}_h \in V_2$, take the dot product with the velocity equation of system (3.3.23) and integrate over the domain $\Omega$, we get:

$$\int_\Omega \boldsymbol{u}_h^{n+1} \cdot \boldsymbol{v}_h + \theta \Delta t \frac{1}{\gamma M^{2-p}} \int_\Omega \nabla p_h^{n+1} \cdot \boldsymbol{v}_h = \int_\Omega \boldsymbol{u}_h^n \cdot \boldsymbol{v}_h$$
$$- (1-\theta) \Delta t \frac{1}{\gamma M^{2-p}} \int_\Omega \nabla p_h^n \cdot \boldsymbol{v}_h. \tag{3.3.44}$$

Integrating by parts we obtain:

$$\int_\Omega \boldsymbol{u}_h^{n+1} \cdot \boldsymbol{v}_h - \theta \Delta t \frac{1}{\gamma M^{2-p}} \int_\Omega p_h^{n+1} \nabla \cdot \boldsymbol{v}_h = \int_\Omega \boldsymbol{u}_h^n \cdot \boldsymbol{v}_h$$
$$+ (1-\theta) \Delta t \frac{1}{\gamma M^{2-p}} \int_\Omega p_h^n \nabla \cdot \boldsymbol{v}_h. \tag{3.3.45}$$

Since the equation on $p$ is strong we substitute for $p_h^{n+1}$ in the last equation and we obtain:

$$A_2(\boldsymbol{u}_h, \boldsymbol{v}_h) = \int_\Omega \boldsymbol{u}_h^{n+1} \cdot \boldsymbol{v}_h + \theta^2 \Delta t^2 \frac{1}{M^{2(1-p)}} \int_\Omega \nabla \cdot \boldsymbol{u}_h^{n+1} \nabla \cdot \boldsymbol{v}_h = b_2(\boldsymbol{v}_h) \quad (3.3.46)$$

with

$$b_2(\boldsymbol{v}_h) = \int_\Omega \boldsymbol{u}_h^n \cdot \boldsymbol{v}_h + \Delta t \frac{1}{\gamma M^{2-p}} \int_\Omega p_h^n \nabla \cdot \boldsymbol{v}_h$$
$$- \theta(1-\theta)\Delta t^2 \frac{1}{M^{2(1-p)}} \int_\Omega \nabla \cdot \boldsymbol{u}_h^n \nabla \cdot \boldsymbol{v}_h \qquad (3.3.47)$$

---

**System 4**

- We first solve for $\boldsymbol{u}_h^{n+1} \in V_2$ through the weak form:

$$A_2(\boldsymbol{u}_h^{n+1}, \boldsymbol{v}_h) = b_2(\boldsymbol{v}_h), \quad \forall \boldsymbol{v}_h \in V_2$$

- Once this is obtained, we compute $p_h^{n+1} \in V_3$ strongly:

$$p_h^{n+1} = -\theta\Delta t \left[ M^p \gamma \nabla \cdot \right] \boldsymbol{u}_h^{n+1} + p_h^n - (1-\theta)\Delta t \left[ M^p \gamma \nabla \cdot \right] \boldsymbol{u}_h^n$$

where:

$$A_2(\boldsymbol{u}_h, \boldsymbol{v}_h) = \int_\Omega \boldsymbol{u}_h^{n+1} \cdot \boldsymbol{v}_h + \theta^2 \Delta t^2 \frac{1}{M^{2(1-p)}} \int_\Omega \nabla \cdot \boldsymbol{u}_h^{n+1} \nabla \cdot \boldsymbol{v}_h = b_2(\boldsymbol{v}_h)$$

with

$$b_2(\boldsymbol{v}_h) = \int_\Omega \boldsymbol{u}_h^n \cdot \boldsymbol{v}_h + \Delta t \frac{1}{\gamma M^{2-p}} \int_\Omega p_h^n \nabla \cdot \boldsymbol{v}_h$$
$$- \theta(1-\theta)\Delta t^2 \frac{1}{M^{2(1-p)}} \int_\Omega \nabla \cdot \boldsymbol{u}_h^n \nabla \cdot \boldsymbol{v}_h$$

---

**Matrix Form 2**

$$\boldsymbol{\mathcal{P}}^{n+1} + \theta\Delta t M^p \gamma \mathcal{D} \boldsymbol{U}^{n+1} = \boldsymbol{\mathcal{P}}^n - (1-\theta)\Delta t M^p \gamma \mathcal{D} \boldsymbol{\mathcal{U}}^n$$

$$(M_2 + \frac{\theta^2 \Delta t^2}{M^{2(1-p)}} \mathcal{D}^T M_2 \mathcal{D}) \boldsymbol{\mathcal{U}}^{n+1} = (M_2 - \frac{\theta(1-\theta)\Delta t^2}{M^{2(1-p)}} \mathcal{D}^T M_2 \mathcal{D}) \boldsymbol{\mathcal{U}}^n$$
$$+ \Delta t \frac{1}{\gamma M^{2-p}} \mathcal{D}^T M_3 \boldsymbol{\mathcal{P}}^n$$

where $M_2 = ((\int_\Omega \boldsymbol{\phi}_{\boldsymbol{i}}^2 \cdot \boldsymbol{\phi}_{\boldsymbol{j}}^2 d\boldsymbol{x}))_{\boldsymbol{i},\boldsymbol{j}}$ is the mass matrix in $V_2$ and $M_3 = ((\int_\Omega \phi_{\boldsymbol{i}}^3 \phi_{\boldsymbol{j}}^3 d\boldsymbol{x}))_{\boldsymbol{i},\boldsymbol{j}}$ is the mass matrix in $V_3$. $\boldsymbol{\mathcal{U}}$ and $\boldsymbol{\mathcal{P}}$ are the vectors of spline coefficients. $\mathcal{D}$ is the discrete divergence operator as defined in section (2.4).

**Remark 3.3.3.** In the case of "Matrix Form 2", we need to invert a matrix with only two variables (the two components of the velocity) in comparison to inverting a matrix with three variables like in the case of classical FE. This reduction allows us also to compute the B-spline coefficients of the pressure in the strong form (matrix-vector product for the computation), in comparison to the classical FE formulation, where we would have had to invert an associated operator. In contrast to using "Matrix Form 1", we note that the operator we are inverting in "Matrix Form 2" contains the two scales that were analysed in section (3.3.1). This reflects badly on the condition number, and this issue can be dealt with with a specific type of preconditioning the discussion of which is beyond the scope of this work. For details see [42]. Matrix Form 1 is also more convenient because we invert a smaller system only for the scalar variable $p$ rather than inverting a system for the vector variable $\boldsymbol{u}$ as in the case of Matrix Form 2.

### 3.3.5 Numerical Results

In this section, we present the numerical results obtained from solving model (3.3.23), where we consider an exact solution and a time dependent manufactured solution.

#### 3.3.5.1 Test Case 1: Exact Solution

For simplicity, we ignore the constants (set all constants to 1). Model (3.3.36) has the following exact solution on the domain $\Omega = [0,1] \times [0,1]$ and $t \in [0,T]$:

$$\begin{cases} p = -2\sqrt{2}\pi \sin(2\pi\sqrt{2}t)\cos(2\pi x)\cos(2\pi y) \\ u_1 = 2\pi \cos(2\pi\sqrt{2}t)\sin(2\pi x)\cos(2\pi y) \\ u_2 = 2\pi \cos(2\pi\sqrt{2}t)\cos(2\pi x)\sin(2\pi y) \end{cases} \tag{3.3.48}$$

We run the simulation with the initial conditions given by the exact solution at $t = 0$:

**Remark 3.3.4.** When considering formulation $(H(rot; \Omega) - H^1(\Omega))$, we need to insure that the vorticity is initialized correctly to zero at the discrete level. We make use of the identity:

$$rot(\nabla \phi) = 0$$

where $\phi$ is a scalar field and $rot\boldsymbol{u} = -\partial_y u_x + \partial_x u_y$. For that, we introduce a field $\phi \in H^1(\Omega)$, and define $\boldsymbol{u} = \nabla\phi$, which reiterates that $\boldsymbol{u} \in H(rot; \Omega)$, considering

the associated de Rham sequence. The discrete field $\phi_h$ is found through using
the $L_2$-projection into $V_0$ (We use the $L_2$-projection rather than the commuting
projector $\Pi_0$ for simplicity), and hence:

$$\boldsymbol{u}_h = \nabla\phi_h \in V_1, \quad \text{which leads to} \quad w_h = rot\boldsymbol{u}_h = 0.$$

The $\phi$ which would lead to the velocity initialization found in Eq. (3.3.48) is:

$$\phi = -\cos(2\pi x)\cos(2\pi y).$$

We present in what follows the results of the simulation considering the system to
be solved in what we call Reduction 1 and Reduction 2. Fig. (3.1) presents the
convergence rates obtained from using Reduction 1 - $(H(rot;\Omega) - H^1(\Omega))$, where
we can see that the convergence order is as expected from using B-spline of degrees
2,3 and 4, whereas Fig. (3.2) shows the convergence rates obtained with various
B-splines' polynomial degrees considering Reduction 2 - $(H(div;\Omega) - L^2(\Omega))$. In
both cases, the final time of simulation is T = 0.1s.



(A) p               (B) $u_1$               (C) $u_2$
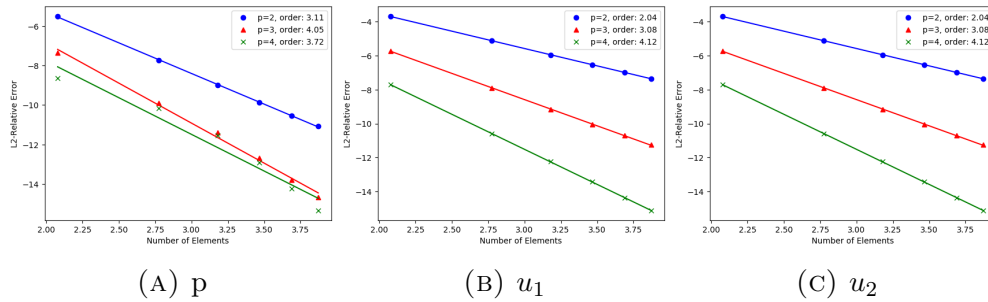
FIGURE 3.1: Log-Log plot showing the convergence orders for the acoustic
system with an exact solution considering Reduction 1 - $(H(rot;\Omega) - H^1(\Omega))$.
T = 0.1 and with a spline degree 2,3 and 4.



(A) p               (B) $u_1$               (C) $u_2$
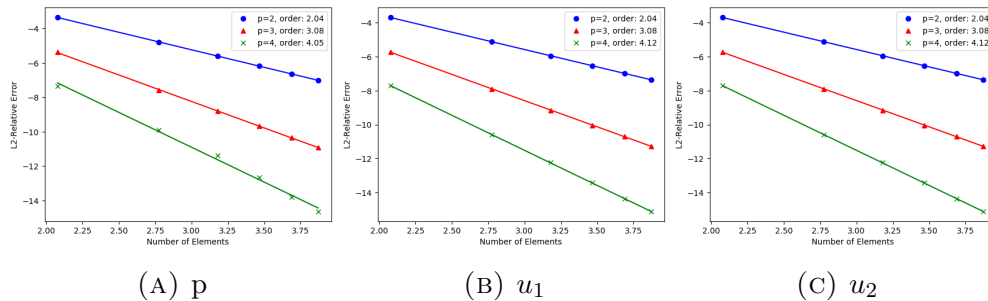
FIGURE 3.2: Log-Log plot showing the convergence orders for the acoustic
system with an exact solution considering Reduction 2 - $(H(div;\Omega) - L^2(\Omega))$.
We use B-spline degrees 2,3,4. T = 0.1s.

We also include how the initialization for each of the pressure and the two components of the velocity vector field look like, where we plot both the analytical and the numerical initializations. Considering Reduction 1-($H(rot; \Omega) - H^1(\Omega)$), we can see the initialization in Fig. (3.3a, 3.4a, 3.5a) for p, $u_1$ and $u_2$, respectively. The analytical solution is plotted in red while the numerical solution is plotted in blue. One can barely distinguish the red plot as the two solutions are very close to one another. Fig. (3.3b, 3.4b, 3.5b) show how the numerical solution compares to the analytical solution at time 0.5s, and Fig. (3.3c, 3.4c, 3.5c) show how the numerical solution compares to the analytical solution at final time step, t = 1s.



(A) Initialization (t = 0s)          (B) t = 0.5s          (C) t = 1s
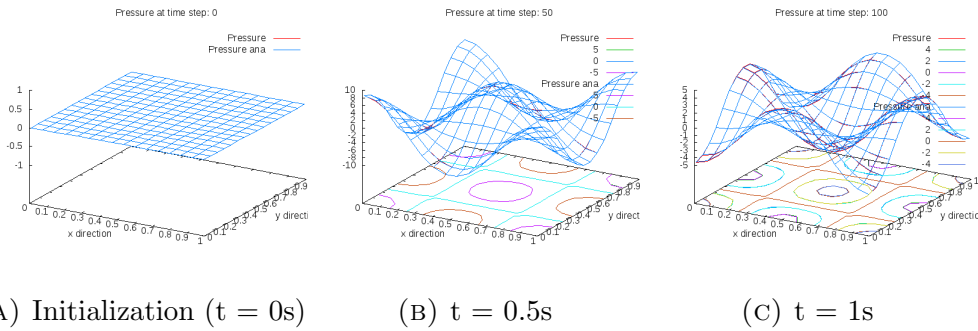
FIGURE 3.3: Reduction 1 - ($H(rot; \Omega) - H^1(\Omega)$): Numerical solution versus analytical solution for the pressure (p). The simulation was run with 16 elements in each direction and B-splines of degree 2, with $\Delta t = 0.01$



(A) Initialization (t = 0s)          (B) t = 0.5s          (C) t = 1s
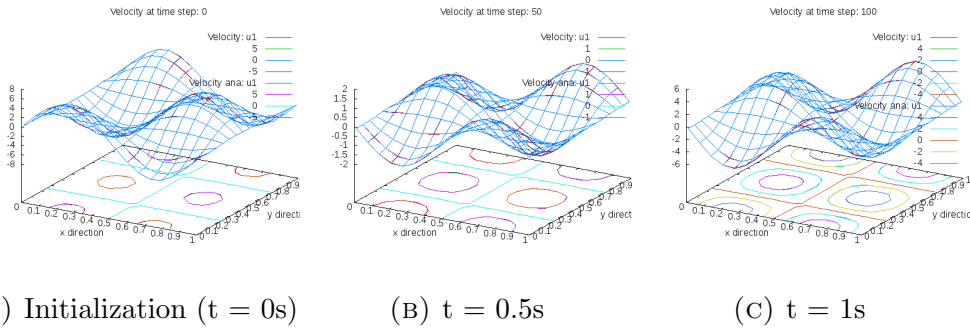
FIGURE 3.4: Reduction 1 - ($H(rot; \Omega) - H^1(\Omega)$): Numerical solution versus analytical solution for the first component of the velocity ($u_1$). The simulation was run with 16 elements in each direction and B-splines of degree 2, with $\Delta t = 0.01$

(A) Initialization (t = 0s)     (B) t = 0.5s     (C) t = 1s
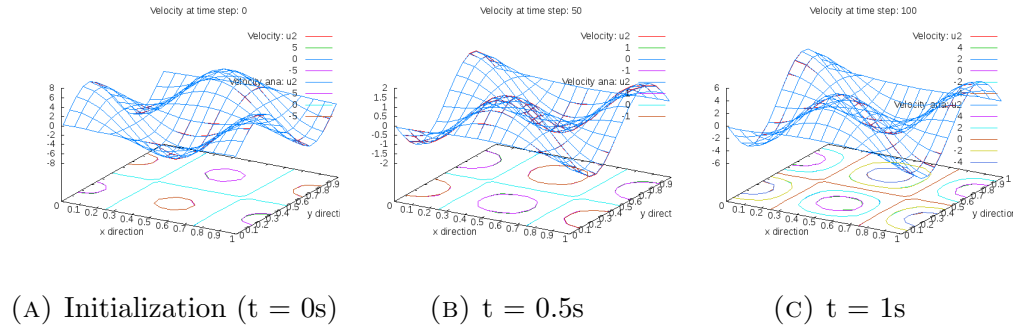
FIGURE 3.5: Reduction 1 - $(H(rot; \Omega) - H^1(\Omega))$: Numerical solution versus analytical solution for the second component of the velocity ($u_2$). The simulation was run with 16 elements in each direction and B-splines of degree 2, with
$$\Delta t = 0.01$$

As for using Reduction 2 - $(H(div; \Omega) - L^2(\Omega))$, then the solution looks the same as in the case of Reduction 1 - $(H(rot; \Omega) - H^1(\Omega))$.

### 3.3.5.2 Total Energy and Vorticity

We include here the plots for the total energy and the vorticity over time. Fig. (3.6) shows the plots using Reduction 1 - $(H(rot; \Omega) - H^1(\Omega))$. The total energy is conserved up to $10^{-11}$ in the case of $dt = 10^{-2}$ (T = 100s), whereas the vorticity is preserved up to $10^{-11}$ in the case of $dt = 10^{-2}$, as can be seen in Fig. (3.6b).



(A) Total Energy     (B) Vorticity
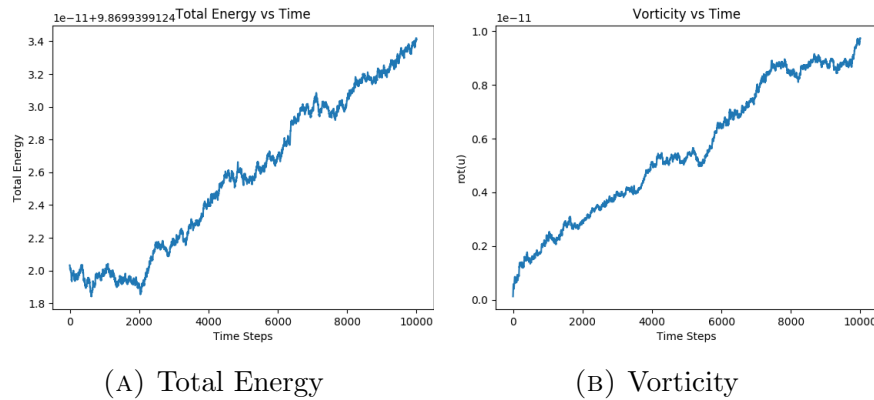
FIGURE 3.6: Total Energy and Vorticity plotted versus time for 16 elements in each direction and B-splines degree 2, with 10000 time steps and dt = 0.01, with Reduction 1 - $(H(rot; \Omega) - H^1(\Omega))$

We also show the total energy conservation for the case of Reduction 2 - $(H(div; \Omega) - L^2(\Omega))$ as can be seen in Fig. (3.7). Fig. (3.7a) demonstrates that the total energy is conserved up to $10^{-12}$ in the case of $dt = 10^{-2}$ and it is conserved up to $10^{-11}$ in the case of $dt = 10^{-4}$, as can be seen in Fig. (3.7b).

(A) Total Energy with $dt = 10^{-2}$    (B) Total Energy with $dt = 10^{-4}$
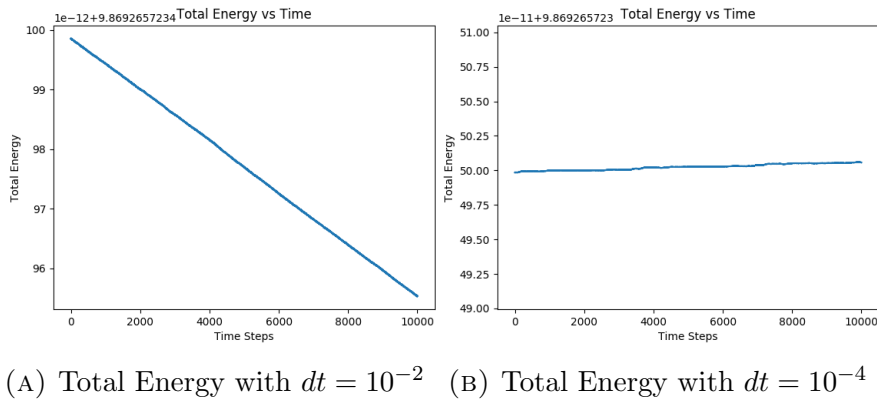
FIGURE 3.7: Total Energy and Vorticity plotted versus time for 16 elements in each direction and B-splines degree 2, with 10000 time steps and using Reduction 2-$(H(div; \Omega) - L^2(\Omega))$

**Remark 3.3.5.** We do not include the vorticity in the case of Formulation $(H(div; \Omega) - L^2(\Omega))$, where $\boldsymbol{u} \in H(div; \Omega)$ because it is not permitted to apply the rot operator on a vector field living in $H(div; \Omega)$, according to the de Rham sequence, and hence this formulation is not able to preserve the vorticity.

In Fig. (3.8), we can see the advantage of using the reduced formulation versus solving the system directly. For brevity, we include the results considering only Reduction - 2 from the point of view of computational costs as outlined in Remark (3.3.3). Note that Reduction - 1 leads to a faster algorithm than Reduction - 2, as we have specified above.



(A) B-splines of degree 5        (B) B-splines of degree 7
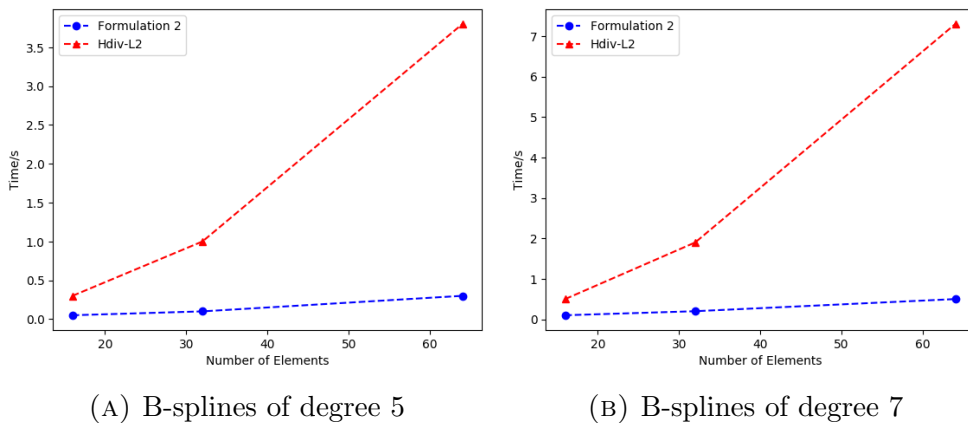
FIGURE 3.8: CPU time comparison between using the numerical scheme outlined in Reduction - 2 versus the full formulation for the space pair $H(div; \Omega) - L^2(\Omega)$.

### 3.3.5.3   Numerical Scheme for a Manufactured Solution

In this case, we derive a right hand side which corresponds to an assumed solution for each respective equation of model (3.3.23) (velocity and pressure equations). We define $S_p$ to be the source term associated with the pressure equation and $\boldsymbol{S_u}$ to be the source term associated with the velocity equation. We note that in order to have a commuting de Rham sequence, we need to have $S_p$ projected into $V_3$, so $S_{p_h} = \Pi_3 S_p$ and hence $S_{p_h} \in V_3$. As for $\boldsymbol{S_u}$, we require that $\boldsymbol{S_{uh}} = \Pi_2 \boldsymbol{S_u}$ and hence $\boldsymbol{S_{uh}} \in V_2$. The commuting projectors are defined in section (2.3).

In order to derive the spatial and temporal discretization for the manufactured solution case, we follow similar steps to those taken in "Reduction 2" and consider only the formulation $(H(div; \Omega) - L^2(\Omega))$ for brevity (the same procedure follows for $H(rot; \Omega) - H^1(\Omega))$; we take the equation for pressure strongly and plug it in the weak form of the velocity equation. The final system discretized in space and time is:

> **System 4**
>
> - We solve for $\boldsymbol{u}_h^{n+1} \in V_2$ via:
>
> $$A_2(\boldsymbol{u}_h^{n+1}, \boldsymbol{v}_h) = b_2(\boldsymbol{v}_h), \quad \forall \boldsymbol{v}_h \in V_2$$
>
> - Once $\boldsymbol{u}_h^{n+1}$ is obtained, we compute $p_h^{n+1} \in V_3$ strongly:
>
> $$p_h^{n+1} = -\theta \Delta t \left[ M^p \gamma \nabla \cdot \right] \boldsymbol{u}_h^{n+1} + p_h^n - (1-\theta)\Delta t \left[ M^p \gamma \nabla \cdot \right] \boldsymbol{u}_h^n + \Delta t S_{p_h}^n$$
>
> where:
>
> $$A_2(\boldsymbol{u}_h, \boldsymbol{v}_h) = \int_\Omega \boldsymbol{u}_h^{n+1} \cdot \boldsymbol{v}_h + \theta^2 \Delta t^2 \frac{1}{M^{2(1-p)}} \int_\Omega \nabla \cdot \boldsymbol{u}_h^{n+1} \nabla \cdot \boldsymbol{v}_h = b_2(\boldsymbol{v}_h)$$
>
> and
>
> $$b_2(\boldsymbol{v}_h) = \int_\Omega \boldsymbol{u}_h^n \cdot \boldsymbol{v}_h + \frac{\Delta t}{\gamma M^{2-p}} \int_\Omega p_h^n \nabla \cdot \boldsymbol{v}_h - \frac{c_i c_e}{M^{2(1-p)}} \int_\Omega \nabla \cdot \boldsymbol{u}_h^n \nabla \cdot \boldsymbol{v}_h$$
> $$+ \Delta t^2 \frac{1}{\gamma M^{2-p}} \int_\Omega S_{p_h}^n \nabla \cdot \boldsymbol{v}_h + \Delta t \int_\Omega \boldsymbol{S_{uh}}^n \cdot \boldsymbol{v}_h$$
>
> where $S_{p_h}^n = \frac{1}{\Delta t} \int_\Omega \int_{t_n}^{t_{n+1}} S_{p_h} dt$ and $\boldsymbol{S_{uh}}^n = \frac{1}{\Delta t} \int_\Omega \int_{t_n}^{t_{n+1}} \boldsymbol{S_{uh}} dt$.

> **Matrix Form 2**
>
> $$\boldsymbol{\mathcal{P}}^{n+1} + \theta \Delta t M^p \gamma \mathcal{D} \boldsymbol{\mathcal{U}}^{n+1} = \boldsymbol{\mathcal{P}}^n - (1-\theta)\Delta t M^p \gamma \mathcal{D} \boldsymbol{\mathcal{U}}^n + \Delta t S_{ph}^n$$
>
> $$(M_2 + \theta^2 \Delta t^2 \frac{1}{M^{2(1-p)}} \mathcal{D}^T M_2 \mathcal{D}) \boldsymbol{\mathcal{U}}^{n+1} = M_2 \boldsymbol{\mathcal{U}}^n + \Delta t \frac{1}{\gamma M^{2-p}} \mathcal{D}^T M_3 \boldsymbol{\mathcal{P}}^n$$
>
> $$- \theta(1-\theta)\Delta t^2 \frac{1}{M^{2(1-p)}} \mathcal{D}^T M_2 \mathcal{D} \boldsymbol{\mathcal{U}}^n + \Delta t \frac{1}{\gamma M^{2-p}} \mathcal{D}^T M_3 S_{ph}^n + \Delta t M_2 \boldsymbol{S_{uh}}^n$$
>
> where $M_2 = ((\int_\Omega \boldsymbol{\phi_i^2} \cdot \boldsymbol{\phi_j^2} d\boldsymbol{x}))_{i,j}$ is the mass matrix in $V_2$ and $M_3 = ((\int_\Omega \phi_i^3 \phi_j^3 d\boldsymbol{x}))_{i,j}$ is the mass matrix in $V_3$. $\boldsymbol{\mathcal{U}}$ and $\boldsymbol{\mathcal{P}}$ are the vectors of spline coefficients. $\mathcal{D}$ is the discrete divergence operator.

#### 3.3.5.4 Test Case 2: Time Dependent Solution

If we assume that the state variables (pressure and velocity) have the following solution defined on the domain $\Omega = [0,1] \times [0,1]$ and $t \in [0,T]$:

$$\begin{cases} p = exp(-\pi t)\sin(2\pi x)\sin(2\pi y) \\ u_1 = exp(-\pi t)\sin(2\pi x)\sin(2\pi y) \\ u_2 = exp(-\pi t)\sin(2\pi x)\sin(2\pi y) \end{cases} \tag{3.3.49}$$

Note that the BC required for the variational formulation are verified. Neglecting the constant coefficients (set all constant coefficients to 1), the corresponding source terms are defined on the domain $\Omega = [0,1] \times [0,1]$ and $t \in [0,T]$ and have the form:

$$\begin{cases} S_p = -\pi exp(-\pi t)\sin(2\pi x)\sin(2\pi y) + 2\pi exp(-\pi t)(\cos(2\pi x)\sin(2\pi y) \\ + \sin(2\pi x)\cos(2\pi y)) \\ S_{u1} = -\pi exp(-\pi t)\sin(2\pi x)\sin(2\pi y) + 2\pi exp(-\pi t)\cos(2\pi x)\sin(2\pi y) \\ S_{u2} = -\pi exp(-\pi t)\sin(2\pi x)\sin(2\pi y) + 2\pi exp(-\pi t)\sin(2\pi x)\cos(2\pi y) \end{cases} \tag{3.3.50}$$

We include in Fig. (3.9) the convergence rates obtained from running the test case with the assumed solution (3.3.49).

(A) p      (B) $u_1$      (C) $u_2$
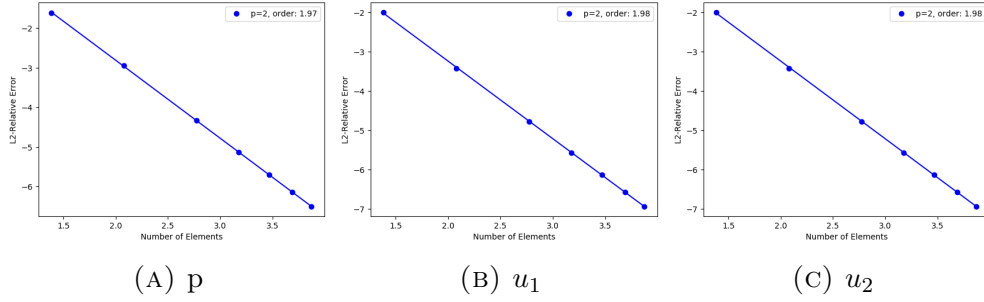
FIGURE 3.9: Log-Log plot showing the convergence orders for the acoustic system with a time dependent source term considering Reduction 2 - $(H(div; \Omega) - L^2(\Omega))$ and B-spline degree 2.

In this section, we have introduced the linear acoustic step and derived two important invariant properties (the total energy and the vorticity). We have discretized the system spatially and temporally and presented test cases to verify the numerical schemes we derived. In the following part, we follow similar steps for the analysis of the linear magnetic step.

## 3.4 Linear Magnetic Step with Constant Coefficients

The model for the magnetic part, which is a hyperbolic system used to model the magnetic field perturbation defined on $\Omega = [0,1] \times [0,1]$, $t \in [0,T]$, where t is the time and T is the final time, at the continuous level is given by:

$$\begin{cases} \partial_t \boldsymbol{u} - \dfrac{1}{M^{2-p}\beta^{1-q}}(rot\boldsymbol{B})\mathbf{b}^\perp = -\dfrac{1}{M^{2-p}\beta^{1-q}}j\boldsymbol{B}^\perp \\[4mm] \partial_t \boldsymbol{B} + M^p \beta^q \nabla^\perp (\boldsymbol{u} \cdot \mathbf{b}^\perp) = 0 \end{cases} \qquad (3.4.51)$$

with adequate boundary conditions which will be defined later on. $\boldsymbol{u}$ is the velocity field, $\boldsymbol{B}$ is the magnetic field, $j$ is the background current density and $\mathbf{b}$ is the background magnetic field. The constant coefficients are defined in detail in section (3.1.3). We also use the notation:

$$\mathbf{b}^\perp = (-b_2, \quad b_1)^T, \quad rot\boldsymbol{B} = \partial_x B_y - \partial_y B_x, \quad \nabla^\perp F = (\partial_y F, \quad -\partial_x F)^T.$$

With the following conservation properties:

> **Conservation properties**
>
> - Defining
> $$E(t) = \int_\Omega \left( \frac{|\boldsymbol{B}|^2}{2\beta} + M^2 \frac{|\boldsymbol{u}|^2}{2} \right)$$
> The model satisfies
> $$\frac{dE(t)}{dt} = \frac{M^p}{\beta^{1-q}} \int_\Omega j\boldsymbol{B}^\perp \cdot \boldsymbol{u}$$
>
> - If the equilibrium current is zero then the energy is preserved.
> - The divergence of the magnetic field is preserved in time.

*Proof.* To prove the energy conservation at the continuous level, we take the dot product of the velocity equation of model (3.4.51) with $M^2\boldsymbol{u}$ and the magnetic equation of model (3.4.51) with $\frac{\boldsymbol{B}}{\beta}$ and integrate over the whole domain $\Omega$:

$$\frac{M^2}{2}\partial_t \int_\Omega |\boldsymbol{u}|^2 - \frac{1}{M^{-p}\beta^{1-q}} \int_\Omega (rot\boldsymbol{B})\mathbf{b}^\perp \cdot \boldsymbol{u} = \frac{1}{M^{-p}\beta^{1-q}} \int_\Omega j\boldsymbol{B}^\perp \cdot \boldsymbol{u} \quad (3.4.52)$$

$$\frac{1}{2\beta}\partial_t \int_\Omega |\boldsymbol{B}|^2 + M^p\beta^{q-1} \int_\Omega \nabla^\perp(\boldsymbol{u} \cdot \mathbf{b}^\perp) \cdot \boldsymbol{B} = 0 \quad (3.4.53)$$

Integrating the term $-\frac{1}{M^{2-p}\beta^{1-q}} \int_\Omega (rot\boldsymbol{B})\mathbf{b}^\perp \cdot \boldsymbol{u}$ by parts, making use of Green's formula:

$$-\frac{1}{M^{2-p}\beta^{1-q}} \int_\Omega (rot\boldsymbol{B})\mathbf{b}^\perp \cdot \boldsymbol{u} = \int_\Omega \boldsymbol{B} \cdot \nabla^\perp(\boldsymbol{u} \cdot \mathbf{b}^\perp) - \int_\Gamma (\boldsymbol{B} \cdot \boldsymbol{n}^\perp)(\boldsymbol{u} \cdot \mathbf{b}^\perp)$$

we eliminate the boundary term by choosing a vanishing Neumann boundary condition, so we set $\boldsymbol{B} \cdot \boldsymbol{n}^\perp |_\Gamma = 0$. We note that the dual of "$rot$" is "$\nabla^\perp$", and adding Eq. (3.4.52) to Eq. (3.4.53), which corresponds to the total energy of the system:

$$\frac{dE(t)}{dt} = \frac{M^2}{2}\partial_t \int_\Omega |\boldsymbol{u}|^2 + \frac{1}{2\beta}\partial_t \int_\Omega |\boldsymbol{B}|^2$$

$$\frac{dE(t)}{dt} = \frac{1}{M^{-p}\beta^{1-q}} \int_\Omega (rot\boldsymbol{B})\mathbf{b}^\perp \cdot \boldsymbol{u} - M^p\beta^{q-1} \int_\Omega \nabla^\perp(\boldsymbol{u} \cdot \mathbf{b}^\perp) \cdot \boldsymbol{B} + \frac{1}{M^{-p}\beta^{1-q}} \int_\Omega j\boldsymbol{B}^\perp \cdot \boldsymbol{u}$$

$$\frac{dE(t)}{dt} = \frac{1}{M^{-p}\beta^{1-q}} \int_\Omega j\boldsymbol{B}^\perp \cdot \boldsymbol{u}$$

In the case of a zero equilibrium current, the energy is preserved. □

### 3.4.1 Wave Structure of the Linear Magnetic Step

To analyse the wave structure of the magnetic step, we compute the wave speeds through the calculation of the eigenvalues of the Jacobian in the direction of the normal vector $\boldsymbol{\theta}$. The Jacobian is:

$$\hat{T} = \begin{pmatrix} 0 & 0 & -\frac{1}{M^{2-p}\beta^{1-q}}b_2\theta_2 & \frac{1}{M^{2-p}\beta^{1-q}}b_2\theta_1 \\ 0 & 0 & \frac{1}{M^{2-p}\beta^{1-q}}b_1\theta_2 & -\frac{1}{M^{2-p}\beta^{1-q}}b_1\theta_1 \\ -\beta^q M^p b_2\theta_2 & \beta^q M^p b_2\theta_1 & 0 & 0 \\ \beta^q M^p b_1\theta_2 & -\beta^q M^p b_1\theta_1 & 0 & 0 \end{pmatrix}.$$

We find the four eigenvalues of the matrix $\hat{T}$ which correspond to the slow and fast magnetoacoustic waves:

$$\lambda = \pm(\frac{1}{2}V_a^2 \pm V_{ac})^{\frac{1}{2}}$$

with the Alfven speed $V_a$ given by: $V_a^2 = M^{2p-2}\beta^{2q-1}(\boldsymbol{\theta}\cdot\mathbf{b})^2$ and $V_{ac}^2 = \frac{1}{4}V_a^4$ which simplifies to having: $\lambda_1 = -V_a$, $\lambda_2 = 0$, $\lambda_3 = 0$ and $\lambda_4 = V_a$

### 3.4.2 The Spatial Discretization and the associated de Rham Sequence

In order to choose the correct spaces for model (3.4.51) that ensures the exact preservation of the divergence free condition at the discrete level, we refer to the 2D de Rham sequence introduced earlier in section (2.3). We consider taking $\boldsymbol{B} \in H(div; \Omega)$, as we need that in order to insure that $\nabla \cdot \boldsymbol{B}$ at the discrete level. We also note that we need $\boldsymbol{u} \in H(div; \Omega)$, as the velocity is a vector field and needs to be defined within the same de Rham sequence and assume that $\boldsymbol{u}\cdot\mathbf{b}^\perp \in H^1(\Omega)$. If we apply the commuting projector $\Pi_2$ to the magnetic equation of model (3.4.51), we obtain:

$$\partial_t\Pi_2\boldsymbol{B} + \Pi_2\nabla^\perp(\boldsymbol{u}\cdot\mathbf{b}^\perp) = 0 \tag{3.4.54}$$

The commuting diagram implies that $\Pi_2\nabla^\perp = \nabla^\perp\Pi_0$, and we note that $\boldsymbol{B}_h = \Pi_2\boldsymbol{B}$ hence $\boldsymbol{B}_h \in V_2$, and the discrete velocity field $\boldsymbol{u}_h \in V_2$ and assume that $\boldsymbol{u}_h\cdot\mathbf{b}^\perp \in H^1(\Omega)$:

$$\partial_t\boldsymbol{B}_h + \nabla^\perp\Pi_0(\boldsymbol{u}_h\cdot\mathbf{b}^\perp) = 0 \tag{3.4.55}$$

For the purposes of this work, we assume that $\mathbf{b}^\perp$ to be constant in each component.

**Remark 3.4.1.** The energy conservation relies on the symmetry between the term $\int_\Omega (rot\boldsymbol{B})\mathbf{b}^\perp \cdot \boldsymbol{u}$ and the term $\int_\Omega \nabla^\perp(\boldsymbol{u} \cdot \mathbf{b}^\perp) \cdot \boldsymbol{B}$. This needs to be conserved at the discrete level. Hence the commuting projector $\Pi_0$ is also needed in the weak form of the velocity equation of model (3.4.51) at the discrete level.

We start by introducing a test function $\boldsymbol{v} \in H(div; \Omega)$ and take the dot product with the velocity equation of model (3.4.51) while setting $j = 0$ and integrate over the domain $\Omega$:

$$\partial_t \int_\Omega \boldsymbol{u} \cdot \boldsymbol{v} - \int_\Omega \boldsymbol{B} \cdot \nabla^\perp(\boldsymbol{v} \cdot \mathbf{b}^\perp) = 0, \ \forall \boldsymbol{v} \in H(div; \Omega). \tag{3.4.56}$$

Considering remark (3.4.1), we write the discrete version of Eq. (3.4.56) in the following manner:

$$\partial_t \int_\Omega \boldsymbol{u}_h \cdot \boldsymbol{v}_h - \int_\Omega \boldsymbol{B}_h \cdot \nabla^\perp \Pi_0(\boldsymbol{v}_h \cdot \mathbf{b}^\perp) = 0, \ \forall \boldsymbol{v}_h \in V_2 \tag{3.4.57}$$

where $\boldsymbol{u}_h \in V_2$ and $\boldsymbol{B}_h \in V_2$.

This results in the following system, where we solve the velocity equation of model (3.4.51) weakly, and the magnetic equation of model (3.4.51) strongly:

---
**Spatially discretized magnetic step**

Find $(\boldsymbol{u}_h, \boldsymbol{B}_h) \in V_2$ such that:

$$\partial_t \int_\Omega \boldsymbol{u}_h \cdot \boldsymbol{v}_h - \int_\Omega \boldsymbol{B}_h \cdot \nabla^\perp \Pi_0(\boldsymbol{v}_h \cdot \mathbf{b}^\perp) = 0, \ \forall \boldsymbol{v}_h \in V_2$$

and
$$\partial_t \boldsymbol{B}_h + \nabla^\perp \Pi_0(\boldsymbol{u}_h \cdot \mathbf{b}^\perp) = 0,$$

assuming that $\boldsymbol{u}_h \cdot \mathbf{b}^\perp \in H^1(\Omega)$.

---

**Remark 3.4.2.** Using the above mentioned spatial discretization leads to the preservation of the total energy and holds the divergence free condition true, as the application of the divergence operator on $\partial_t \boldsymbol{B}_h + \nabla^\perp \Pi_0(\boldsymbol{u}_h \cdot \mathbf{b}^\perp) = 0$, leads to a divergence-free magnetic field, given that $\nabla \cdot \boldsymbol{B}_h = 0$ is enforced initially.

### 3.4.3 Discretization in Time

As in the case of the acoustic step, we use the general $\theta$-scheme on model (3.4.51). We obtain the following model discretized in time:

$$
\begin{cases}
\displaystyle \int_\Omega \boldsymbol{u}_h^{n+1} \cdot \boldsymbol{v}_h - \theta\Delta t \frac{1}{M^{2-p}\beta^{1-q}} \int_\Omega \nabla_h^\perp \Pi_0(\boldsymbol{v}_h \cdot \mathbf{b}^\perp) \cdot \boldsymbol{B}_h^{n+1} = \int_\Omega \boldsymbol{u}_h^n \cdot \boldsymbol{v}_h \\[2mm]
\displaystyle +(1-\theta)\Delta t \frac{1}{M^{2-p}\beta^{1-q}} \int_\Omega \nabla^\perp \Pi_0(\boldsymbol{v}_h \cdot \mathbf{b}^\perp) \cdot \boldsymbol{B}_h^n \\[4mm]
\displaystyle \boldsymbol{B}_h^{n+1} = \boldsymbol{B}_h^n - \theta\Delta t M^p \beta^q \nabla^\perp \Pi_0(\boldsymbol{u}_h^{n+1} \cdot \mathbf{b}^\perp) - (1-\theta)\Delta t M^p \beta^q \nabla^\perp \Pi_0(\boldsymbol{u}_h^n \cdot \mathbf{b}^\perp)
\end{cases}
$$
$$(3.4.58)$$

Plugging in $\boldsymbol{B}_h^{n+1}$ into the weak formulation of the velocity equation of system (3.4.58):

$$
\begin{cases}
\displaystyle \int_\Omega \boldsymbol{u}_h^{n+1} \cdot \boldsymbol{v}_h - \theta\Delta t \frac{1}{M^{2-p}\beta^{1-q}} \int_\Omega \nabla_h^\perp \Pi_0(\boldsymbol{v}_h \cdot \mathbf{b}^\perp) \cdot (\boldsymbol{B}_h^n - \theta\Delta t M^p \beta^q \nabla_h^\perp \Pi_0(\boldsymbol{u}_h^{n+1} \cdot \mathbf{b}^\perp) \\[4mm]
\displaystyle -(1-\theta)\Delta t M^p \beta^q \nabla_h^\perp \Pi_0(\boldsymbol{u}_h^n \cdot \mathbf{b}^\perp)) = \int_\Omega \boldsymbol{u}_h^n \cdot \boldsymbol{v}_h \\[4mm]
\displaystyle +(1-\theta)\Delta t \frac{1}{M^{2-p}\beta^{1-q}} \int_\Omega \nabla_h^\perp \Pi_0(\boldsymbol{v}_h \cdot \mathbf{b}^\perp) \cdot \boldsymbol{B}_h^n
\end{cases}
$$
$$(3.4.59)$$

Defining $c_i = \theta\Delta t$, and $c_e = (1-\theta)\Delta t$ and expanding the velocity equation we obtain at the end:

---

**Magnetic step discretized in space and time 1**

- We first solve for $\boldsymbol{u}_h^{n+1}$ such that $\boldsymbol{u}_h \in V_2$ from the weak form:

$$A(\boldsymbol{u}_h^{n+1}, \boldsymbol{v}_h) = b_1(\boldsymbol{v}_h) + b_2(\boldsymbol{v}_h), \quad \forall \boldsymbol{v}_h \in V_2,$$

where:
$$A(\boldsymbol{u}_h^{n+1}, \boldsymbol{v}_h) = \int_\Omega \boldsymbol{u}_h^{n+1} \cdot \boldsymbol{v}_h$$
$$+ \frac{c_i^2}{M^{2-2p}\beta^{1-2q}} \int_\Omega \nabla^\perp \Pi_0(\boldsymbol{u}_h^{n+1} \cdot \mathbf{b}^\perp) \cdot \nabla^\perp \Pi_0(\boldsymbol{v}_h \cdot \mathbf{b}^\perp)$$

with

$$b_1(\boldsymbol{v}_h) = \int_\Omega \boldsymbol{u}_h^n \cdot \boldsymbol{v}_h + \frac{\Delta t}{M^{2-p}\beta^{1-q}} \int_\Omega \boldsymbol{B}_h^n \cdot \nabla^\perp \Pi_0(\boldsymbol{v}_h \cdot \mathbf{b}^\perp)$$

$$b_2(\boldsymbol{v}_h) = -\frac{c_i c_e}{M^{2-2p}\beta^{1-2q}} \int_\Omega \nabla^\perp \Pi_0(\boldsymbol{u}_h^n \cdot \mathbf{b}^\perp) \cdot \nabla^\perp \Pi_0(\boldsymbol{v}_h \cdot \mathbf{b}^\perp)$$

- Once $\boldsymbol{u}_h^{n+1}$ is obtained, we compute $\boldsymbol{B}_h^{n+1}$ such that $\boldsymbol{B}_h \in V_2$ from the strong form:

$$\boldsymbol{B}_h^{n+1} = -M^p \beta^q c_i \nabla^\perp \Pi_0(\boldsymbol{u}_h^{n+1} \cdot \mathbf{b}^\perp) + \boldsymbol{B}_h^n - c_e M^p \beta^q \nabla^\perp \Pi_0(\boldsymbol{u}_h^n \cdot \mathbf{b}^\perp)$$

assuming that $\boldsymbol{u}_h \cdot \mathbf{b}^\perp \in H^1 \Omega$.

---

Due to a limitation that we have in our code implementation, we are not able to apply the projector $\Pi_0$ on the test functions as is required in terms such as $\int_\Omega \nabla^\perp \Pi_0(\boldsymbol{u}_h^n \cdot \mathbf{b}^\perp) \cdot \nabla^\perp \Pi_0(\boldsymbol{v}_h \cdot \mathbf{b}^\perp)$, where we use $\Pi_0 = \mathcal{I}$, where $\mathcal{I}$ is the identity matrix. For the commuting projectors in the strong form, we use the $L_2$ projection instead, in the following manner:

$$\boldsymbol{B}_h^{n+1} = -M^p \beta^q c_i \nabla^\perp \Pi_0^{L2}(\boldsymbol{u}_h^{n+1} \cdot \mathbf{b}^\perp) + \boldsymbol{B}_h^n - c_e M^p \beta^q \nabla^\perp \Pi_0^{L2}(\boldsymbol{u}_h^n \cdot \mathbf{b}^\perp) \quad (3.4.60)$$

**Remark 3.4.3.** The $L_2$ projector into $V_0$ for a function f is defined in the following way:

$$\int_\Omega \Pi_0^{L2} f v dx = \int_\Omega f v dx \quad v \in V_0$$

so if F is the matrix of spline coefficients of $\Pi_0^{L2} f$, we have:

$$F = M_0^{-1} \begin{pmatrix} \int_\Omega f \phi_1^0 \\ \vdots \\ \int_\Omega f \phi_{N0}^0 \end{pmatrix}$$

where $M_0$ is the mass matrix defined on $V_0$ and $(\phi_i^0)_{1 \le i \le N_0}$ stands for the basis functions defined on $V_0$

**Remark 3.4.4.** Note that we have omitted projecting the dot products $\boldsymbol{u}_h^{n+1} \cdot \mathbf{b}^\perp$, $\boldsymbol{u}_h^n \cdot \mathbf{b}^\perp$ and $\boldsymbol{v}_h \cdot \mathbf{b}^\perp$ present in the weak formulation of the velocity equation into the $V_0$ space using the commuting projector $\Pi_0$. This is possible considering that we are using smooth enough functions and B-splines of at least degree 2 for the choice of the basis functions. We have also replaced the commuting projector $\Pi_0$ in the strong form of the magnetic field with the classical $L_2$ projector in $V_0$. Such a formulation breaks the symmetry that is needed in order to insure the energy conservation as specified in Remark (3.4.1), but still guarantees the adherence to the divergence free condition ($\nabla \cdot \boldsymbol{B}_h = 0$), as if we apply the $\nabla \cdot$ operator to the Eq. (3.4.60), we obtain $\nabla \cdot \boldsymbol{B}_h^{n+1} = 0$, given that $\nabla \cdot \boldsymbol{B}_h^0 = 0$, keeping in mind that $\nabla \cdot (\nabla^\perp) = 0$.

### 3.4.4 Numerical Results

In this section, we present numerical results of solving the linear magnetic step, we consider an exact solution and a manufactured solution.

#### 3.4.4.1 Test Case 1: Exact Solution

In this section, we derive an exact solution that fulfills model (3.4.51) using the method of separation of variables and we use the solution to test our numerical scheme. We start by setting $j = 0$ and ignoring the constant coefficients. We assume that the magnetic field has the following form:

$$\boldsymbol{B} = \partial_t \begin{pmatrix} C_1 \\ C_2 \end{pmatrix} \tag{3.4.61}$$

where $C_1$ and $C_2$ are variables to be determined and the form of the velocity is obtained through plugging the form of the magnetic field into the velocity equation

of model (3.4.51):

$$\boldsymbol{u} = rot\begin{pmatrix} C_1 \\ C_2 \end{pmatrix}\mathbf{b}^{\perp} \tag{3.4.62}$$

Where $\mathbf{b}^{\perp} = (-b_2, b_1)^T$. Plugging Eq. (3.4.61) and Eq. (3.4.62) into (3.4.51) leads to:

$$\begin{cases} \partial_{tt}C_1 - ||\mathbf{b}^{\perp}||^2 \Delta C_1 = 0 \\ \partial_{tt}C_2 - ||\mathbf{b}^{\perp}||^2 \Delta C_2 = 0 \end{cases} \tag{3.4.63}$$

Assuming that $C_1$ and $C_2$ have a solution of the form:

$$\begin{cases} C_1 = -\alpha(t)\cos(k_1\pi x)\sin(k_1\pi y) \\ C_2 = \beta(t)\sin(k_2\pi x)\cos(k_2\pi y) \end{cases} \tag{3.4.64}$$

Plugging in the form of $C_1$ and $C_2$ into (3.4.63):

$$\begin{cases} \alpha''(t)\cos(k_1\pi x)\sin(k_1\pi y) + 2(k_1\pi)^2||\mathbf{b}^{\perp}||^2\alpha(t)\cos(k_1\pi x)\sin(k_1\pi y) = 0 \\ \beta''(t)\sin(k_2\pi x)\cos(k_2\pi y) + 2(k_2\pi)^2||\mathbf{b}^{\perp}||^2\beta(t)\sin(k_2\pi x)\cos(k_2\pi y) = 0 \end{cases} \tag{3.4.65}$$

$$\begin{cases} \alpha''(t) + 2(k_1\pi)^2||\mathbf{b}^{\perp}||^2\alpha(t) = 0 \\ \beta''(t) + 2(k_2\pi)^2||\mathbf{b}^{\perp}||^2\beta(t) = 0 \end{cases} \tag{3.4.66}$$

which are a couple of second order ODEs, with the roots of the characteristic equation: $\Delta_1 = -8(k_1\pi)^2||\mathbf{b}^{\perp}||^2$ and $\Delta_2 = -8(k_2\pi)^2||\mathbf{b}^{\perp}||^2$. The associated eigenvalues to $\Delta_1$ are:

$$\lambda_{1,2} = \pm\sqrt{2}k_1\pi||\mathbf{b}^{\perp}||i \tag{3.4.67}$$

and to $\Delta_2$:

$$\lambda_{1,2} = \pm\sqrt{2}k_2\pi||\mathbf{b}^{\perp}||i \tag{3.4.68}$$

This has a general solution of the form:

$$\begin{cases} \alpha(t) = c_1\cos(Et) + c_2\sin(Et) \\ \beta(t) = c_3\cos(Dt) + c_4\sin(Dt) \end{cases} \tag{3.4.69}$$

where $E = \sqrt{2}k_1\pi||\mathbf{b}^{\perp}||$ and $D = \sqrt{2}k_2\pi||\mathbf{b}^{\perp}||$. Assuming that $\alpha(0) = 1, \alpha'(0) = 0$ and $\beta(0) = 1, \beta'(0) = 0$, this leads to $c_1 = 1$, $c_2 = 0$, $c_3 = 1$, $c_4 = 0$.

$$\begin{cases} \alpha(t) = \cos(Et) \\ \beta(t) = \cos(Dt) \end{cases} \tag{3.4.70}$$

$$\begin{cases} C_1 = -\cos(Et)\cos(k_1\pi x)\sin(k_1\pi y) \\ C_2 = \cos(Dt)\sin(k_2\pi x)\cos(k_2\pi y) \end{cases} \tag{3.4.71}$$

as:

$$\boldsymbol{B} = \partial_t \begin{pmatrix} C_1 \\ C_2 \end{pmatrix} \tag{3.4.72}$$

then:

$$\boldsymbol{B} = \begin{pmatrix} E\sin(Et)\cos(k_1\pi x)\sin(k_1\pi y) \\ -D\sin(Dt)\sin(k_2\pi x)\cos(k_2\pi y) \end{pmatrix} \tag{3.4.73}$$

and as:

$$\boldsymbol{u} = rot \begin{pmatrix} C_1 \\ C_2 \end{pmatrix} \mathbf{b}^{\perp} \tag{3.4.74}$$

then:

$$\boldsymbol{u} = (k_2\pi\cos(Dt)\cos(k_2\pi x)\cos(k_2\pi y) + k_1\pi\cos(Et)\cos(k_1\pi x)\cos(k_1\pi y))\mathbf{b}^{\perp}. \tag{3.4.75}$$

We present here the results for running model (3.4.51) with a background magnetic field given by $\mathbf{b}^{\perp} = (0.7, 0.3)$ and $k_1 = k_2 = 2.0$. Fig. (3.10) shows the convergence rates obtained from using the exact solution (3.4.75),(3.4.73), where the solutions are superconvergent with order 4,6 and 8 for B-splines degree of 2,3 and 4.



(A) $B_1$ 

(B) $B_2$

(C) $u_1$ 

(D) $u_2$
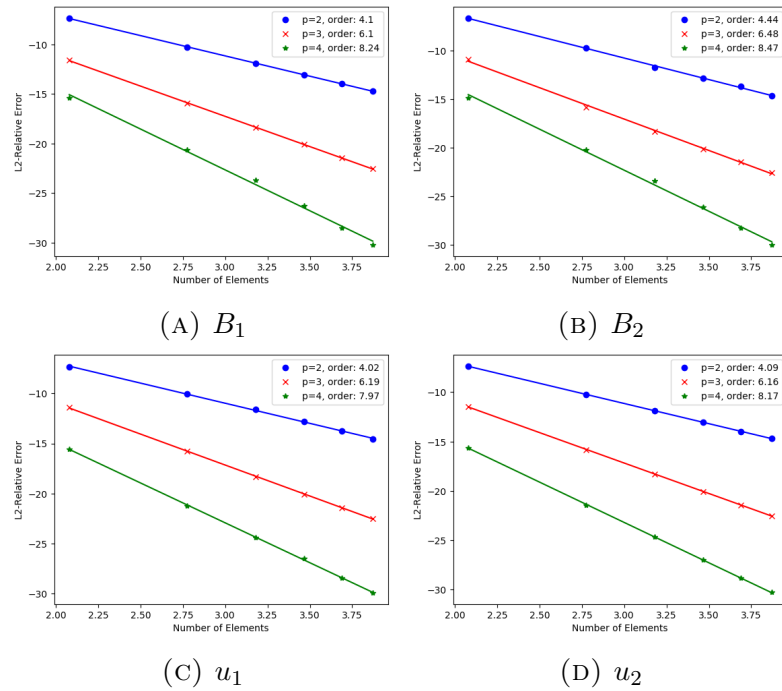
FIGURE 3.10: Log-Log plot for the convergence rates for the magnetic field and the velocity with an exact solution where $\mathbf{b}^{\perp} = (0.7, 0.3)$ and B-spline degrees 2,3 and 4.

(A) Total Energy

(B) $\nabla \cdot \boldsymbol{B}_h^n$
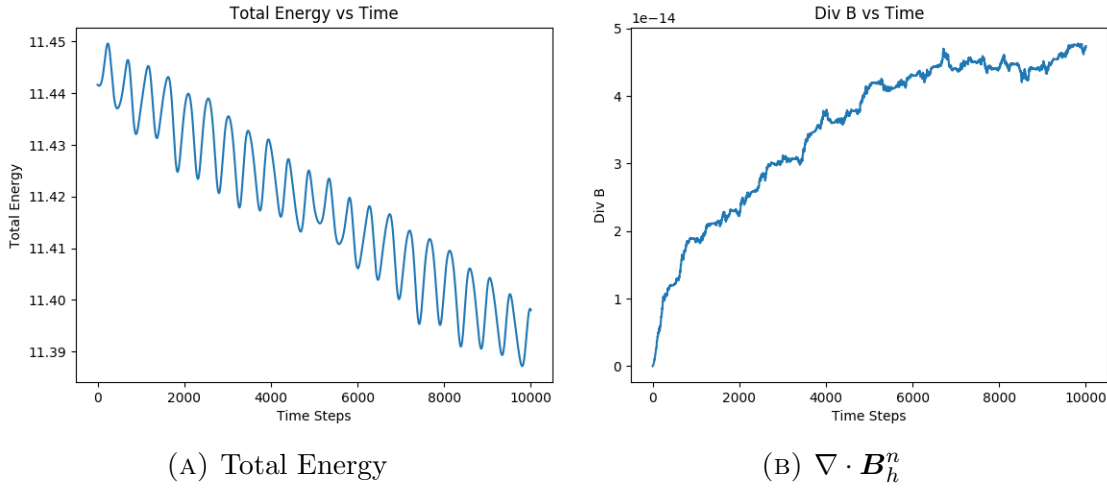
FIGURE 3.11: Total Energy and $\nabla \cdot \boldsymbol{B}_h^n$ plotted versus time for 8 elements in each direction and B-splines degree 2, with 10000 time steps, dt = 0.001 and $\mathbf{b}^\perp = (0.7, 0.3)$

The total energy can be seen in Fig. (3.11a). We can see that the total energy is not conserved, as expected ensuing the discussion in Remark (3.4.4). Fig. (3.11b) shows the preservation of the divergence free condition up to $10^{-14}$.

### 3.4.4.2 Numerical Scheme for a Manufactured Solution

For the manufactured solution, we choose a solution for the velocity and magnetic fields and derive a right hand side which corresponds to the assumed solution. This RHS acts like a source term for each respective equation of model (3.4.51) (velocity and magnetic equations). Setting $j = 0$ and ignoring the constants, the model could be written as:

$$\begin{cases} \partial_t \boldsymbol{u} - \dfrac{1}{M^{2-p}\beta^{1-q}}(rot\boldsymbol{B})\mathbf{b}^\perp = \boldsymbol{S_u} \\[4mm] \partial_t \boldsymbol{B} + M^p\beta^q \nabla^\perp(\boldsymbol{u} \cdot \mathbf{b}^\perp) = \boldsymbol{S_b} \end{cases} \tag{3.4.76}$$

where we define $\boldsymbol{S_u}$ to be the source term associated with the velocity equation and $\boldsymbol{S_b}$ is the source term associated with the magnetic equation. As before, we consider $\boldsymbol{u} \in H(div; \Omega)$ and $\boldsymbol{B} \in H(div; \Omega)$, with vanishing Neumann boundary condition $(\boldsymbol{B} \cdot \boldsymbol{n}^\perp \mid_\Gamma = 0)$. We note that in order to have a commuting de Rham sequence, we need to have $\boldsymbol{S_b} \in H(div; \Omega)$, hence $\boldsymbol{S_{bh}} = \Pi_2 \boldsymbol{S_b}$, so $\boldsymbol{S_{bh}} \in V_2$. As for $\boldsymbol{S_u}$, we also require to have $\boldsymbol{S_u} \in H(div; \Omega)$, hence $\boldsymbol{S_{uh}} = \Pi_2 \boldsymbol{S_u}$ and it follows that $\boldsymbol{S_{uh}} \in V_2$. The commuting projector $\Pi_2$ is defined in section (2.3). We use

the same strategy as we did in the case of model (3.4.51); we take the magnetic equation in the strong form (at the splines' coefficients level) and discretize it in space and time, while we take the velocity equation weakly, and discretize it in space and time. We plug in the magnetic equation (strong form) into the velocity equation (weak form) and we get:

---

**Magnetic step with a source term discretized in space and time**

- We solve first for $\boldsymbol{u}_h^{n+1}$ such that $\boldsymbol{u}_h \in V_2$ from the weak form:

$$A(\boldsymbol{u}_h^{n+1}, \boldsymbol{v}_h) = b_1(\boldsymbol{v}_h) + b_2(\boldsymbol{v}_h) + b_3(\boldsymbol{v}_h), \quad \forall \boldsymbol{v}_h \in V_2$$

  Where:

$$A(\boldsymbol{u}_h^{n+1}, \boldsymbol{v}_h) = \int_\Omega \boldsymbol{u}_h^{n+1} \cdot \boldsymbol{v}_h + c_i^2 \int_\Omega \nabla^\perp(\boldsymbol{u}_h^{n+1} \cdot \mathbf{b}^\perp) \cdot \nabla^\perp(\boldsymbol{v}_h \cdot \mathbf{b}^\perp)$$

  with

$$b_1(\boldsymbol{v}_h) = \int_\Omega \boldsymbol{u}_h^n \cdot \boldsymbol{v}_h + \Delta t \int_\Omega \boldsymbol{B}_h^n \cdot \nabla^\perp(\boldsymbol{v}_h \cdot \mathbf{b}^\perp)$$

$$b_2(\boldsymbol{v}_h) = -c_i c_e \int_\Omega \nabla^\perp(\boldsymbol{u}_h^n \cdot \mathbf{b}^\perp) \cdot \nabla^\perp(\boldsymbol{v}_h \cdot \mathbf{b}^\perp)$$

$$b_3(\boldsymbol{v}_h) = c_i \Delta t \int_\Omega \nabla^\perp(\boldsymbol{u}_h^n \cdot \mathbf{b}^\perp) \cdot \boldsymbol{S_b}_h^n + \Delta t \int_\Omega \boldsymbol{S_u}_h^n \cdot \boldsymbol{v}_h$$

- Once we obtain $\boldsymbol{u}_h^{n+1}$, we solve for $\boldsymbol{B}_h^{n+1}$ such that $\boldsymbol{B}_h \in V_2$ through the strong form:

$$\boldsymbol{B}_h^{n+1} = -c_i \nabla^\perp \Pi_0^{L2}(\boldsymbol{u}_h^{n+1} \cdot \mathbf{b}^\perp) + \boldsymbol{B}_h^n - c_e \nabla^\perp \Pi_0^{L2}(\boldsymbol{u}_h^n \cdot \mathbf{b}^\perp) + \Delta t \boldsymbol{S_b}_h^n$$

where: $\boldsymbol{S_u}_h^n = \frac{1}{\Delta t} \int_\Omega \int_{t_n}^{t_{n+1}} \boldsymbol{S_u}_h dt$ and $\boldsymbol{S_b}_h^n = \frac{1}{\Delta t} \int_\Omega \int_{t_n}^{t_{n+1}} \boldsymbol{S_b}_h dt$, assuming that $\boldsymbol{u}_h \cdot \mathbf{b}^\perp \in H^1(\Omega)$.

---

To test the numerical scheme outlined above, we propose two test cases, one with a steady state solution, and the other one is with a time dependent solution. We start with the steady state solution.

### 3.4.4.3 Test Case 2: Steady State Solution

If we assume that:

$$
\begin{cases}
B_1 = \cos(2\pi x) \cdot \sin(2\pi y), & (x, y) \in \Omega \\
B_2 = -\sin(2\pi x) \cdot \cos(2\pi y), & (x, y) \in \Omega \\
u_1 = \sin(2\pi x) \cdot \sin(2\pi y), & (x, y) \in \Omega \\
u_2 = \sin(2\pi x) \cdot \sin(2\pi y), & (x, y) \in \Omega
\end{cases}
\tag{3.4.77}
$$

Plugging in (3.4.77) into model (3.4.76), we get the following corresponding source terms ignoring the constant coefficients:

$$
\begin{cases}
S_{B1} = 2\pi(b_1 - b_2) \sin(2\pi x) \cos(2\pi y), & (x, y) \in \Omega \\
S_{B2} = -2\pi(b_1 - b_2) \cos(2\pi x) \sin(2\pi y), & (x, y) \in \Omega \\
S_{u1} = -4\pi b_2 \cos(2\pi x) \cos(2\pi y), & (x, y) \in \Omega \\
S_{u2} = 4\pi b_1 \cos(2\pi x) \cos(2\pi y), & (x, y) \in \Omega
\end{cases}
\tag{3.4.78}
$$

As before, we present the convergence orders. Fig. (3.12) shows the convergence rates obtained with $\mathbf{b}^\perp = (1.0, 1.0)$ from using the assumed solution (3.4.77), where like in the previous cases, the solutions are superconvergent with order 4 rather than the expected order 2.



(A) $B_1$      (B) $B_2$

(C) $u_1$      (D) $u_2$

FIGURE 3.12: Log-Log plot for the convergence rates for the magnetic field and the velocity with a steady state manufactured solution where $\mathbf{b}^\perp = (1.0, 1.0)$ and B-spline degree 2

The divergence of the magnetic field at the discrete level for background magnetic field configuration $\mathbf{b}^{\perp} = (1.0, 1.0)$ is shown in Fig. (3.15), where the divergence is preserved up to $10^{-14}$.
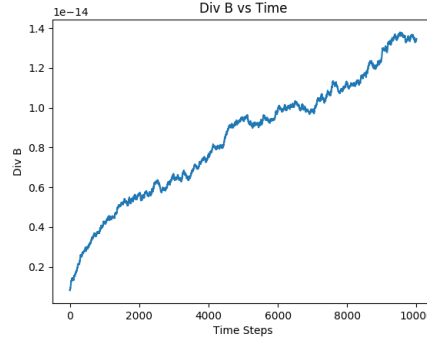


FIGURE 3.13: $\nabla \cdot B_h$ for the case of steady state solution plotted versus time for the case of 8 elements in each direction, dt = 0.001 and T = 10s, and with background magnetic field $\mathbf{b}^{\perp} = (1.0, 1.0)$.

#### 3.4.4.4 Test Case 3: Time Dependent Solution

If we assume that:

$$\begin{cases} B_1 = e^{-\pi t} \cos(2\pi x) \cdot \sin(2\pi y) & , (x, y) \in \Omega, t \in [0, T] \\ B_2 = -e^{-\pi t} \sin(2\pi x) \cdot \cos(2\pi y), (x, y) \in \Omega, t \in [0, T] \\ u_1 = e^{-\pi t} \sin(2\pi x) \cdot \sin(2\pi y) & , (x, y) \in \Omega, t \in [0, T] \\ u_2 = e^{-\pi t} \sin(2\pi x) \cdot \sin(2\pi y) & , (x, y) \in \Omega, t \in [0, T] \end{cases} \qquad (3.4.79)$$

Then the corresponding source terms ignoring the constant coefficients, for $(x, y) \in \Omega$ and $t \in [0, T]$, are:

$$\begin{cases} S_{B1} = -\pi e^{-\pi t} \cos(2\pi x) \sin(2\pi y) + 2\pi(b_1 - b_2)e^{-\pi t} \sin(2\pi x) \cos(2\pi y) \\ S_{B2} = \pi e^{-\pi t} \sin(2\pi x) \cos(2\pi y) - 2\pi(b_1 - b_2)e^{-\pi t} \cos(2\pi x) \sin(2\pi y) \\ S_{u1} = -\pi e^{-\pi t} \sin(2\pi x) \sin(2\pi y) - 4\pi b_2 e^{-\pi t} \cos(2\pi x) \cos(2\pi y) \\ S_{u2} = -\pi e^{-\pi t} \sin(2\pi x) \sin(2\pi y) + 4\pi b_1 e^{-\pi t} \cos(2\pi x) \cos(2\pi y) \end{cases}$$
$$(3.4.80)$$

Fig. (3.14) presents the convergence rates obtained from using the assumed solution (3.4.79) with $\mathbf{b}^{\perp} = (0.7, 0.3)$, where one can see that the solutions are also in this case superconvergent. Fig. (3.15) on the other hand, shows the evolution of the divergence of the magnetic field for a background magnetic field configuration given by $\mathbf{b}^{\perp} = (0.7, 0.3)$. The divergence is preserved up to $10^{-15}$. We note that this is also easily satisfied, considering that we have a time damping component.

In the following part, we propose another test case without the time damping component.



(A) $B_1$

(B) $B_2$

(C) $u_1$

(D) $u_2$
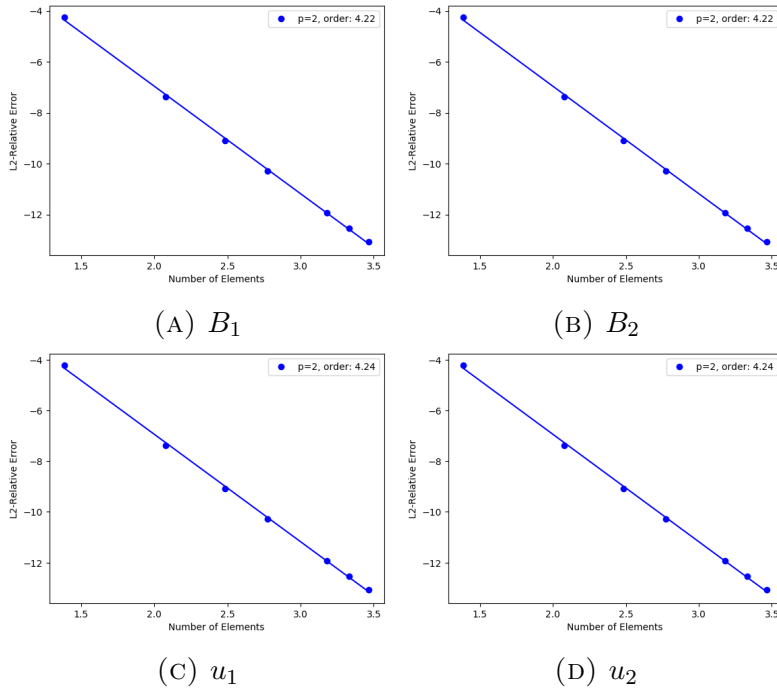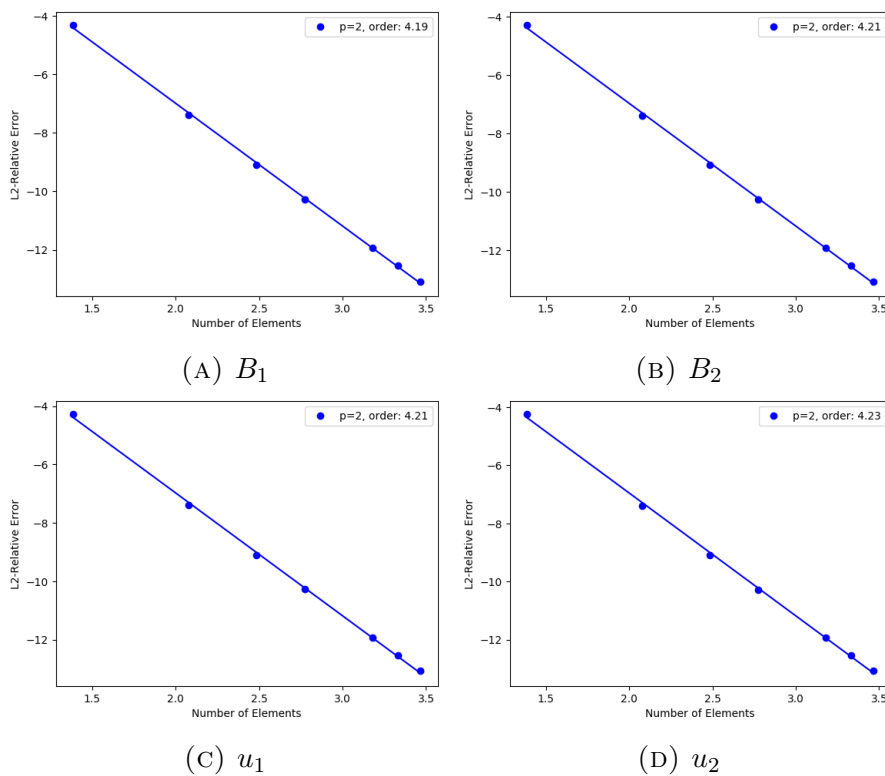
FIGURE 3.14: Convergence rates for the magnetic field and the velocity with a time dependent manufactured solution where $\mathbf{b}^\perp = (0.7, 0.3)$
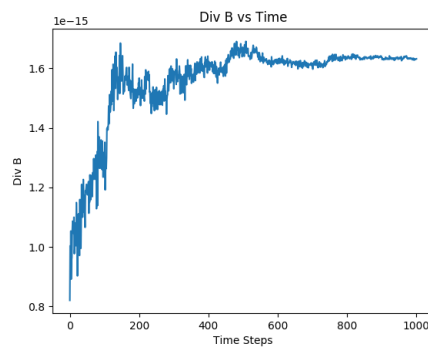


FIGURE 3.15: $\nabla \cdot B_h$ for the case of time dependent solution plotted versus time for the case of 8 elements in each direction, dt = 0.001 and T = 1s and $\mathbf{b}^\perp = (0.7, 0.3)$

We propose now another test case without time damping:

$$\begin{cases} B_1 = \cos(t)\cos(2\pi x) \cdot \sin(2\pi y), & (x,y) \in \Omega, t \in [0,T] \\ B_2 = -\cos(t)\sin(2\pi x) \cdot \sin(2\pi y), & (x,y) \in \Omega, t \in [0,T] \\ u_1 = \cos(t)\sin(2\pi x) \cdot \sin(2\pi y), & (x,y) \in \Omega, t \in [0,T] \\ u_2 = \cos(t)\sin(2\pi x) \cdot \sin(2\pi y), & (x,y) \in \Omega, t \in [0,T] \end{cases} \quad (3.4.81)$$

and the corresponding source terms, for $(x,y) \in \Omega$ and $t \in [0,T]$ are:

$$\begin{cases} S_{B1} = -\sin(t)\cos(2\pi x)\sin(2\pi y) + 2\pi(b_1 - b_2)\cos(t)\sin(2\pi x)\cos(2\pi y) \\ S_{B2} = \sin(t)\sin(2\pi x)\cos(2\pi y) - 2\pi(b_1 - b_2)\cos(t)\cos(2\pi x)\sin(2\pi y) \\ S_{u1} = -\sin(t)\sin(2\pi x)\sin(2\pi y) - 4\pi b_2 \cos(t)\cos(2\pi x)\cos(2\pi y) \\ S_{u2} = -\sin(t)\sin(2\pi x)\sin(2\pi y) + 4\pi b_1 \cos(t)\cos(2\pi x)\cos(2\pi y) \end{cases}$$
$$(3.4.82)$$

Fig. (3.16) shows the divergence-free condition at the discrete level when using the time dependent solution (3.4.81). We can see that the divergence is conserved up to $10^{-15}$ in the case of a background magnetic field configuration given by $\mathbf{b}^\perp = (0.7, 0.3)$.
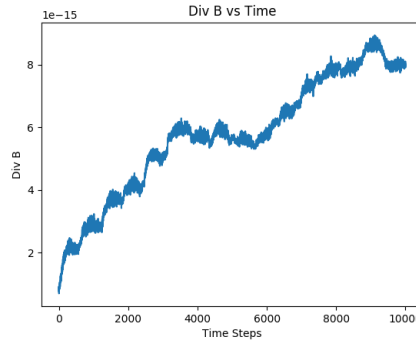


FIGURE 3.16: $\nabla \cdot \boldsymbol{B}_h$ for the case of time dependent solution plotted versus time for the case of 8 elements in each direction, dt = 0.005 and T = 50s and $\mathbf{b}^\perp = (0.7, 0.3)$

## 3.5 Linear Convection-Diffusion Step with Constant Coefficients

The model for the convection-diffusion part defined on $\Omega = [0,1] \times [0,1]$ and $t \in [0,T]$, where t is the time and T is the final time, at the continuous level is

given by:

$$
\begin{cases}
\partial_t p + M^p \beta^q \boldsymbol{a} \cdot \nabla p = \dfrac{(\gamma - 1) M^p \beta^q}{R_e P_r} \Delta p \\[3mm]
\partial_t \boldsymbol{u} + M^p \beta^q \boldsymbol{a} \cdot \nabla \boldsymbol{u} = \dfrac{M^p \beta^q}{R_e} \left( \Delta \boldsymbol{u} + k \nabla (\nabla \cdot \boldsymbol{u}) \right) \\[3mm]
\partial_t \boldsymbol{B} + M^p \beta^q \nabla^\perp (\boldsymbol{a} \cdot \boldsymbol{B}^\perp) = -\dfrac{1}{R_m} \nabla^\perp (rot \boldsymbol{B})
\end{cases}
\tag{3.5.83}
$$

with adequate boundary conditions which are defined later on. $\boldsymbol{u}$ is the velocity field, $p$ is the pressure and $\boldsymbol{B}$ is the magnetic field. $\boldsymbol{a}$ is the advection velocity. The constant coefficients are defined in section (3.1.3), whereas the operators are defined in the following manner: $\nabla^\perp F = (\partial_y F, \ -\partial_x F)^T$, $rot\boldsymbol{B} = \partial_x B_y - \partial_y B_x$, and the gradient operator is defined as: $\nabla F = (\partial_x F, \ \partial_y F)^T$. Note that $\boldsymbol{B}^\perp = (-B_2, \ B_1)^T$.

## 3.5.1 Spatial Discretization and the Associated de Rham Sequence

As the equations of the pressure, magnetic field and velocity are decoupled, we treat each one separately:

- We start by looking at the pressure equation of model (3.5.83):

$$
\partial_t p + M^p \beta^q \boldsymbol{a} \cdot \nabla p = \dfrac{(\gamma - 1) M^p \beta^q}{R_e P_r} \Delta p
\tag{3.5.84}
$$

We rewrite Eq. (3.5.84) as:

$$
\partial_t p + M^p \beta^q \nabla \cdot (\boldsymbol{a} p) = \dfrac{(\gamma - 1) M^p \beta^q}{R_e P_r} \Delta p
\tag{3.5.85}
$$

where we have used that: $\nabla \cdot (\boldsymbol{a} p) = \boldsymbol{a} \cdot \nabla p + p \nabla \cdot \boldsymbol{a}$, and we use a constant advection velocity, so that $\nabla \cdot \boldsymbol{a} = 0$. Looking at de Rham sequence 2 mentioned in section (3.3.2), we take $p \in L^2(\Omega)$ and aim to solve Eq. (3.5.85) strongly, and assume that $\boldsymbol{a} p \in H(div; \Omega)$, so the advection term, $\nabla \cdot (\boldsymbol{a} p)$, is in the same space ($L^2(\Omega)$) as the advected quantity, in this case $p$. Since we cannot define $\nabla p$ strongly, we introduce an additional vector variable, namely $\boldsymbol{y} \in H(div; \Omega)$ and define it as $\boldsymbol{y} = \nabla p$. This leads to an additional

equation, so the system writes:

$$\begin{cases} \partial_t p + M^p \beta^q \nabla \cdot (\boldsymbol{a}p) = \frac{(\gamma-1)M^p\beta^q}{R_e P_r} \nabla \cdot \boldsymbol{y} \\ \\ \nabla p - \boldsymbol{y} = 0 \end{cases} \quad (3.5.86)$$

We introduce a test function $\boldsymbol{w} \in H(div;\Omega)$ and take the dot product of the second equation of (3.5.86) with $\boldsymbol{w}$ and integrate over the domain $\Omega$:

$$\begin{cases} \partial_t p + M^p \beta^q \nabla \cdot (\boldsymbol{a}p) = \frac{(\gamma-1)M^p\beta^q}{R_e P_r} \nabla \cdot \boldsymbol{y} \\ \\ \int_\Omega \nabla p \cdot \boldsymbol{w} - \int_\Omega \boldsymbol{w} \cdot \boldsymbol{y} = 0 \end{cases} \quad (3.5.87)$$

Since $p \in L^2(\Omega)$, then $\nabla p$ is not defined strongly, so we integrate by parts the term $\int_\Omega \nabla p \cdot \boldsymbol{w}$:

$$\int_\Omega \nabla p \cdot \boldsymbol{w} = -\int_\Omega p \nabla \cdot \boldsymbol{w} + \int_\Gamma p(\boldsymbol{n} \cdot \boldsymbol{w}) \quad (3.5.88)$$

where $\Gamma$ is the boundary of $\Omega$ and $\boldsymbol{n}$ is the outward unit vector normal to $\Gamma$. We assume a natural BC such as $p\mid_\Gamma = 0$, which eliminates the boundary term. Hence we look for $p$ such that $p \in L^2(\Omega)$, $\boldsymbol{a}p \in H(div;\Omega)$ and $\boldsymbol{y} \in H(div;\Omega)$ such that:

$$\begin{cases} \partial_t p + M^p \beta^q \nabla \cdot (\boldsymbol{a}p) = \frac{(\gamma-1)M^p\beta^q}{R_e P_r} \nabla \cdot \boldsymbol{y} \\ \\ \int_\Omega p \nabla \cdot \boldsymbol{w} + \int_\Omega \boldsymbol{w} \cdot \boldsymbol{y} = 0, \quad \forall \boldsymbol{w} \in H(div;\Omega) \end{cases} \quad (3.5.89)$$

Now we introduce the spatial discretization. We apply the commuting projector $\Pi_3$ to the first equation of (3.5.91), we obtain:

$$\partial_t \Pi_3 p + M^p \beta^q \Pi_3 \nabla \cdot (\boldsymbol{a}p) = \frac{(\gamma-1)M^p\beta^q}{R_e P_r} \Pi_3 \nabla \cdot \boldsymbol{y} \quad (3.5.90)$$

The commuting diagram implies that $\Pi_3 \nabla \cdot = \nabla \cdot \Pi_2$, and we note that $p_h = \Pi_3 p$ and $\boldsymbol{y}_h = \Pi_2 \boldsymbol{y}$, hence $p_h \in V_3$, $\boldsymbol{y}_h \in V_2$ and $\boldsymbol{a}p_h \in H(div;\Omega)$. For the weak equation, we replace the test and trial functions by their finite

dimensional counterparts. The discretized system reads:

$$\begin{cases} \partial_t p_h + M^p \beta^q \nabla \cdot (\Pi_2(\boldsymbol{a} p_h)) = \frac{(\gamma-1)M^p \beta^q}{R_e P_r} \nabla \cdot \boldsymbol{y}_h \\[2mm] \int_\Omega p_h \nabla \cdot \boldsymbol{w}_h + \int_\Omega \boldsymbol{w}_h \cdot \boldsymbol{y}_h = 0, \qquad \forall \boldsymbol{w}_h \in V_2. \end{cases} \tag{3.5.91}$$

This is the spatial discretization of the pressure equation.

- The Magnetic Equation: We refer to the magnetic equation of model (3.5.83):

$$\partial_t \boldsymbol{B} + M^p \beta^q \nabla^\perp (\boldsymbol{a} \cdot \boldsymbol{B}^\perp) = -\frac{1}{R_m} \nabla^\perp (rot \boldsymbol{B}) \tag{3.5.92}$$

Looking at de Rham sequence 2 mentioned in section (3.3.2), we take $\boldsymbol{B} \in H(div; \Omega)$ and aim to solve the magnetic equation strongly, and assume that $\boldsymbol{a} \cdot \boldsymbol{B}^\perp \in H^1(\Omega)$. Since $\boldsymbol{B} \in H(div; \Omega)$, then $rot\boldsymbol{B}$ is not defined strongly, so we introduce an additional scalar variable $h \in H^1(\Omega)$ such that $rot\boldsymbol{B} = h$, this leads to the following system:

$$\begin{cases} \partial_t \boldsymbol{B} + M^p \beta^q \nabla^\perp (\boldsymbol{a} \cdot \boldsymbol{B}^\perp) = -\frac{1}{R_m} \nabla^\perp h \\[2mm] rot\boldsymbol{B} - h = 0 \end{cases} \tag{3.5.93}$$

We introduce a test function $f \in H^1(\Omega)$ and take the dot product with the second equation of (3.5.93) and integrate over the domain $\Omega$:

$$\begin{cases} \partial_t \boldsymbol{B} + M^p \beta^q \nabla^\perp (\boldsymbol{a} \cdot \boldsymbol{B}^\perp) = -\frac{1}{R_m} \nabla^\perp h \\[2mm] \int_\Omega (rot\boldsymbol{B}) f - \int_\Omega h f = 0 \end{cases} \tag{3.5.94}$$

We integrate the term $\int_\Omega (rot\boldsymbol{B}) f$ by parts:

$$\int_\Omega (rot\boldsymbol{B}) f = \int_\Omega \boldsymbol{B} \cdot \nabla^\perp f - \int_\Gamma (\boldsymbol{B} \cdot \boldsymbol{n}^\perp) f \tag{3.5.95}$$

where $\Gamma$ is the boundary of $\Omega$ and $\boldsymbol{n}$ is the outward unit vector normal to $\Gamma$. In order to eliminate the boundary term, we assume a natural BC in the form of $(\boldsymbol{B} \cdot \boldsymbol{n}^\perp) \mid_\Gamma = 0$. Hence we look for $\boldsymbol{B}$ such that $\boldsymbol{B} \in H(div; \Omega)$,

$\boldsymbol{a} \cdot \boldsymbol{B}^{\perp} \in H^1(\Omega)$ and $h \in H^1(\Omega)$:

$$\begin{cases} \partial_t \boldsymbol{B} + M^p \beta^q \nabla^{\perp}(\boldsymbol{a} \cdot \boldsymbol{B}^{\perp}) = -\frac{1}{R_m} \nabla^{\perp} h \\[2ex] \int_{\Omega} \boldsymbol{B} \cdot \nabla^{\perp} f - \int_{\Omega} hf = 0, \qquad \forall f \in H^1(\Omega). \end{cases} \tag{3.5.96}$$

To introduce the spatial discretization, we use similar steps to those taken for the pressure equation: we apply the commuting projector $\Pi_2$ to the first equation of (3.5.96), use that $\Pi_2 \nabla^{\perp} = \nabla^{\perp} \Pi_0$, define that $\boldsymbol{B}_h = \Pi_2 \boldsymbol{B}$ and $h_h = \Pi_0 h$, so $\boldsymbol{B}_h \in V_2$ and $h_h \in V_0$ and assuming that $\boldsymbol{a} \cdot \boldsymbol{B}_h^{\perp} \in H^1(\Omega)$. For the weak equation, we replace the test and trial functions by their finite dimensional counterparts. The discretized system reads:

$$\begin{cases} \partial_t \boldsymbol{B}_h + M^p \beta^q \nabla^{\perp}(\Pi_0(\boldsymbol{a} \cdot \boldsymbol{B}_h^{\perp})) = -\frac{1}{R_m} \nabla^{\perp} h_h \\[2ex] \int_{\Omega} \boldsymbol{B}_h \cdot \nabla^{\perp} f_h - \int_{\Omega} h_h f_h = 0, \qquad \forall f_h \in V_0 \end{cases} \tag{3.5.97}$$

- The velocity equation: We refer to the velocity equation of model (3.5.83):

$$\partial_t \boldsymbol{u} + M^p \beta^q \boldsymbol{a} \cdot \nabla \boldsymbol{u} = \frac{M^p \beta^q}{R_e} (\Delta \boldsymbol{u} + k \nabla(\nabla \cdot \boldsymbol{u})) \tag{3.5.98}$$

We rewrite the term $\boldsymbol{a} \cdot \nabla \boldsymbol{u}$ using that $\boldsymbol{a} \cdot \nabla \boldsymbol{u} = rot(\boldsymbol{u})\boldsymbol{a}^{\perp} + \nabla(\boldsymbol{a} \cdot \boldsymbol{u})$. We also use that $\Delta \boldsymbol{u} = \nabla(\nabla \cdot \boldsymbol{u}) - \nabla^{\perp}(rot\boldsymbol{u})$, we obtain:

$$\partial_t \boldsymbol{u} + M^p \beta^q rot(\boldsymbol{u})\boldsymbol{a}^{\perp} + M^p \beta^q \nabla(\boldsymbol{a} \cdot \boldsymbol{u}) = \frac{M^p \beta^q}{R_e} \left( -\nabla^{\perp}(rot\boldsymbol{u}) + (1+k)\nabla(\nabla \cdot \boldsymbol{u}) \right). \tag{3.5.99}$$

We take $\boldsymbol{u} \in H(div; \Omega)$, and introduce an additional scalar field $q \in H^1(\Omega)$, where $q$ is defined as $q = rot\boldsymbol{u}$, as $rot\boldsymbol{u}$ is not defined strongly. This leads to rewriting Eq. (3.5.99) as the following system:

$$\begin{cases} \partial_t \boldsymbol{u} + M^p \beta^q rot(\boldsymbol{u})\boldsymbol{a}^{\perp} + M^p \beta^q \nabla(\boldsymbol{a} \cdot \boldsymbol{u}) = \frac{M^p \beta^q}{R_e} \left( -\nabla^{\perp} q + (1+k)\nabla(\nabla \cdot \boldsymbol{u}) \right) \\[2ex] rot\boldsymbol{u} - q = 0 \end{cases} \tag{3.5.100}$$

Where we have replaced $rot(\boldsymbol{u}) = q$ in the RHS of the first equation of Eq. (3.5.100). We introduce the test functions $\boldsymbol{v} \in H(div; \Omega)$ and $g \in H^1(\Omega)$. We take the dot product of the first equation of (3.5.100) with $\boldsymbol{v}$ and the

second equation of (3.5.100) with $g$, and we integrate both equations over the domain $\Omega$, we obtain:

$$
\begin{cases}
\partial_t \int_\Omega \boldsymbol{u} \cdot \boldsymbol{v} + M^p \beta^q \left( \int_\Omega rot\boldsymbol{u}(\boldsymbol{a}^\perp \cdot \boldsymbol{v}) + \int_\Omega \nabla(\boldsymbol{a} \cdot \boldsymbol{u}) \cdot \boldsymbol{v} \right) = \\
\dfrac{M^p \beta^q}{R_e} \left( - \int_\Omega \nabla^\perp q \cdot \boldsymbol{v} + (1+k) \int_\Omega \nabla(\nabla \cdot \boldsymbol{u}) \cdot \boldsymbol{v} \right) \\[4pt]
\int_\Omega (rot\boldsymbol{u})g - \int_\Omega qg = 0
\end{cases}
\tag{3.5.101}
$$

We use integration by parts using Green's formula for the following terms: $\int_\Omega rot\boldsymbol{u}(\boldsymbol{a}^\perp \cdot \boldsymbol{v}))$, $\int_\Omega \nabla(\boldsymbol{a} \cdot \boldsymbol{u}) \cdot \boldsymbol{v}$, $k \int_\Omega \nabla(\nabla \cdot \boldsymbol{u}) \cdot \boldsymbol{v}$ and $\int_\Omega (rot\boldsymbol{u})g$. We outline the integration by parts and the boundary terms for each of the above mentioned terms:

– Integration by part for $\int_\Omega rot\boldsymbol{u}(\boldsymbol{a}^\perp \cdot \boldsymbol{v}))$:

$$
\int_\Omega rot\boldsymbol{u}(\boldsymbol{a}^\perp \cdot \boldsymbol{v})) = \int_\Omega \boldsymbol{u} \cdot \nabla^\perp(\boldsymbol{a}^\perp \cdot \boldsymbol{v})) - \int_\Gamma (\boldsymbol{u} \cdot \boldsymbol{n}^\perp)(\boldsymbol{a}^\perp \cdot \boldsymbol{v})
\tag{3.5.102}
$$

in order to eliminate the boundary term, we choose to set $(\boldsymbol{u} \cdot \boldsymbol{n}^\perp) \mid_\Gamma = 0$.

– Integration by part for $\int_\Omega \nabla(\boldsymbol{a} \cdot \boldsymbol{u}) \cdot \boldsymbol{v}$:

$$
\int_\Omega \nabla(\boldsymbol{a} \cdot \boldsymbol{u}) \cdot \boldsymbol{v} = - \int_\Omega (\boldsymbol{a} \cdot \boldsymbol{u})\nabla \cdot \boldsymbol{v} - \int_\Gamma (\boldsymbol{a} \cdot \boldsymbol{u})(\boldsymbol{v} \cdot \boldsymbol{n})
\tag{3.5.103}
$$

in order to eliminate the boundary term, we set $(\boldsymbol{a} \cdot \boldsymbol{u}) \mid_\Gamma = 0$.

– Integration by part for $k \int_\Omega \nabla(\nabla \cdot \boldsymbol{u}) \cdot \boldsymbol{v}$:

$$
k \int_\Omega \nabla(\nabla \cdot \boldsymbol{u}) \cdot \boldsymbol{v} = -k \int_\Omega \nabla \cdot \boldsymbol{u}\nabla \cdot \boldsymbol{v} - \int_\Gamma \nabla \cdot \boldsymbol{u}(\boldsymbol{v} \cdot \boldsymbol{n})
\tag{3.5.104}
$$

in order to eliminate the boundary term, we need to set $\nabla \cdot \boldsymbol{u} \mid_\Gamma = 0$

– Integration by part for $\int_\Omega (rot\boldsymbol{u})g$:

$$
\int_\Omega (rot\boldsymbol{u})g = \int_\Omega \boldsymbol{u} \cdot \nabla^\perp g - \int_\Gamma (\boldsymbol{u} \cdot \boldsymbol{n}^\perp)g
\tag{3.5.105}
$$

in order to eliminate the boundary term, we set $\boldsymbol{u} \cdot \boldsymbol{n}^\perp \mid_\Gamma = 0$

We end up with the following system: Find $\boldsymbol{u}$ such that $\boldsymbol{u} \in H(div; \Omega)$:

$$\begin{cases} \partial_t \int_\Omega \boldsymbol{u} \cdot \boldsymbol{v} + M^p \beta^q \int_\Omega \boldsymbol{u} \cdot \nabla^\perp(\boldsymbol{a}^\perp \cdot \boldsymbol{v}) - M^p \beta^q \int_\Omega (\boldsymbol{a} \cdot \boldsymbol{u}) \nabla \cdot \boldsymbol{v} = \\ -\dfrac{M^p \beta^q}{R_e} \int_\Omega \nabla^\perp q \cdot \boldsymbol{v} - \dfrac{M^p \beta^q}{R_e}(1+k) \int_\Omega (\nabla \cdot \boldsymbol{u})(\nabla \cdot \boldsymbol{v}), \qquad \forall \boldsymbol{v} \in H(div; \Omega) \\ \\ \int_\Omega qg - \int_\Omega \boldsymbol{u} \cdot \nabla^\perp g = 0, \hspace{4cm} \forall g \in H^1(\Omega) \end{cases}$$
$$(3.5.106)$$

Discretizing the previous system by taking the discrete quantities: $\boldsymbol{u}_h, \boldsymbol{v}_h \in V_2$ and $g, q \in V_0$ and substituting these discrete quantities for their continuous counter parts, we get:

$$\begin{cases} \partial_t \int_\Omega \boldsymbol{u}_h \cdot \boldsymbol{v}_h + M^p \beta^q \int_\Omega \boldsymbol{u}_h \cdot \nabla^\perp \Pi_0(\boldsymbol{a}^\perp \cdot \boldsymbol{v}_h) - M^p \beta^q \int_\Omega (\boldsymbol{a} \cdot \boldsymbol{u}_h) \nabla \cdot \boldsymbol{v}_h = \\ -\dfrac{M^p \beta^q}{R_e} \int_\Omega \nabla^\perp q_h \cdot \boldsymbol{v}_h - \dfrac{M^p \beta^q}{R_e}(1+k) \int_\Omega (\nabla \cdot \boldsymbol{u}_h)(\nabla \cdot \boldsymbol{v}_h), \qquad \forall \boldsymbol{v}_h \in V_2 \\ \\ \int_\Omega q_h g_h - \int_\Omega \boldsymbol{u}_h \cdot \nabla^\perp g_h = 0, \hspace{4cm} \forall g_h \in V_0 \end{cases}$$
$$(3.5.107)$$

The spatial discretization for the convection-diffusion model (3.5.83) can be summarized in the following box:

Find $p_h$ such that $p_h \in V_3$, $\boldsymbol{y}_h \in V_2$ and $\boldsymbol{a}p_h \in H(div; \Omega)$ such that:

$$\begin{cases} \partial_t p_h + M^p \beta^q \nabla \cdot (\Pi_2(\boldsymbol{a}p_h)) = \frac{(\gamma-1)M^p\beta^q}{R_e P_r} \nabla \cdot \boldsymbol{y}_h \\[3mm] \int_\Omega p_h \nabla \cdot \boldsymbol{w}_h + \int_\Omega \boldsymbol{w}_h \cdot \boldsymbol{y}_h = 0, \quad \forall \boldsymbol{w}_h \in V_2 \end{cases}$$

Find $\boldsymbol{B}_h$ such that $\boldsymbol{B}_h \in V_2$, $h_h \in V_0$ and $\boldsymbol{a} \cdot \boldsymbol{B}_h^\perp \in H^1(\Omega)$ such that:

$$\begin{cases} \partial_t \boldsymbol{B}_h + M^p \beta^q \nabla^\perp(\Pi_0(\boldsymbol{a} \cdot \boldsymbol{B}_h^\perp)) = -\frac{1}{R_m} \nabla^\perp h_h \\[3mm] \int_\Omega \boldsymbol{B}_h \cdot \nabla^\perp f_h - \int_\Omega h_h f_h = 0, \quad \forall f_h \in V_0 \end{cases}$$

Find $\boldsymbol{u}_h$ such that $\boldsymbol{u}_h \in V_2$ and $q_h \in V_0$ such that:

$$\begin{cases} \partial_t \int_\Omega \boldsymbol{u}_h \cdot \boldsymbol{v}_h + M^p\beta^q \int_\Omega \boldsymbol{u}_h \cdot \nabla^\perp \Pi_0(\boldsymbol{a}^\perp \cdot \boldsymbol{v}_h) - M^p\beta^q \int_\Omega (\boldsymbol{a} \cdot \boldsymbol{u}_h) \nabla \cdot \boldsymbol{v}_h = \\[3mm] \quad -\frac{M^p\beta^q}{R_e} \int_\Omega \nabla^\perp q_h \cdot \boldsymbol{v}_h - \frac{M^p\beta^q}{R_e}(1+k) \int_\Omega (\nabla \cdot \boldsymbol{u}_h)(\nabla \cdot \boldsymbol{v}_h), \quad \forall \boldsymbol{v}_h \in V_2 \\[3mm] \int_\Omega q_h g_h - \int_\Omega \boldsymbol{u}_h \cdot \nabla^\perp g_h = 0, \quad \forall g_h \in V_0 \end{cases}$$

Due to a limitation that we have in our code implementation, we are not able to apply the projector $\Pi_0$ on the test functions as is required in terms such as $\int_\Omega \boldsymbol{u}_h \cdot \nabla^\perp \Pi_0(\boldsymbol{a}^\perp \cdot \boldsymbol{v}_h)$ where we use $\Pi_0 = \mathcal{I}$, where $\mathcal{I}$ is the identity matrix.

### 3.5.2 Discretization in Time

For convection-diffusion problems, one would use an explicit scheme for the convection term and an implicit scheme for the diffusion term [69]. We use the SBDF-2 scheme [3] to discretize the previous algorithm. We obtain the following system discretized in space and time:

We solve for $p_h^{n+1}$ such that $p_h \in V_3$, $\boldsymbol{y}_h \in V_2$ and $\boldsymbol{a}p_h \in H(div; \Omega)$ such that:

$$
\begin{cases}
\frac{1}{2\Delta t}(3p_h^{n+1} - 4p_h^n + p_h^{n-1}) + M^p\beta^q\nabla\cdot(\Pi_2(\boldsymbol{a}(2p_h^n - p_h^{n-1}))) = \\
\frac{(\gamma-1)M^p\beta^q}{R_e P_r}\nabla\cdot\boldsymbol{y}_h^{n+1} \\
\\
\int_\Omega p_h^{n+1}\nabla\cdot\boldsymbol{w}_h + \int_\Omega \boldsymbol{w}_h\cdot\boldsymbol{y}_h^{n+1} = 0, \quad \forall\boldsymbol{w}_h \in V_2
\end{cases}
$$

We solve for $\boldsymbol{B}_h^{n+1}$ such that $\boldsymbol{B}_h \in V_2$, $h_h \in V_0$ and $\boldsymbol{a}\cdot\boldsymbol{B}_h^\perp \in H^1(\Omega)$ such that:

$$
\begin{cases}
\frac{1}{2\Delta t}(3\boldsymbol{B}_h^{n+1} - 4\boldsymbol{B}_h^n + \boldsymbol{B}_h^{n-1}) + M^p\beta^q\nabla^\perp(\Pi_0(\boldsymbol{a}\cdot(2\boldsymbol{B}_h^{\perp n} - \boldsymbol{B}_h^{\perp n-1}))) = \\
-\frac{1}{R_m}\nabla^\perp h_h^{n+1} \\
\\
\int_\Omega \boldsymbol{B}_h^{n+1}\cdot\nabla^\perp f_h - \int_\Omega h_h^{n+1}f_h = 0, \quad \forall f_h \in V_0
\end{cases}
$$

We solve for $\boldsymbol{u}_h^{n+1}$ such that $\boldsymbol{u}_h \in V_2$ and $q_h \in V_0$ such that:

$$
\begin{cases}
\frac{1}{2\Delta t}\int_\Omega(3\boldsymbol{u}_h^{n+1} - 4\boldsymbol{u}_h^n + \boldsymbol{u}_h^{n-1})\cdot\boldsymbol{v}_h + M^p\beta^q\int_\Omega(2\boldsymbol{u}_h^n - \boldsymbol{u}_h^{n-1})\cdot\nabla^\perp(\boldsymbol{a}^\perp\cdot\boldsymbol{v}_h) \\
-M^p\beta^q\int_\Omega(\boldsymbol{a}\cdot(2\boldsymbol{u}_h^n - \boldsymbol{u}_h^{n-1}))\nabla\cdot\boldsymbol{v}_h = -\frac{M^p\beta^q}{R_e}\int_\Omega\nabla^\perp q_h^{n+1}\cdot\boldsymbol{v}_h \\
-\frac{M^p\beta^q}{R_e}(1+k)\int_\Omega\nabla\cdot\boldsymbol{u}_h^{n+1}\nabla\cdot\boldsymbol{v}_h, \quad \forall\boldsymbol{v}_h \in V_2 \\
\\
\int_\Omega q_h^{n+1}g_h - \int_\Omega \boldsymbol{u}_h^{n+1}\cdot\nabla^\perp g_h = 0, \quad \forall g_h \in V_0
\end{cases}
$$

### 3.5.3 Numerical Results

In this section, we introduce two test cases in order to test the numerical scheme that we have derived in the previous section. The first test case is a steady state manufactured solution and the second is a time dependent manufactured solution.

#### 3.5.3.1 Numerical Scheme for a Manufactured Solution

In this case, we choose a solution for the velocity, pressure and the magnetic field and derive a right hand side which corresponds to the assumed solution. This RHS acts like a source term for each respective equation of model (3.5.83). The

model could be written as:

$$
\begin{cases}
\partial_t p + M^p \beta^q \boldsymbol{a} \cdot \nabla p = \dfrac{(\gamma - 1)M^p \beta^q}{R_e P_r}\Delta p + S_p \\[4mm]
\partial_t \boldsymbol{u} + M^p \beta^q \boldsymbol{a} \cdot \nabla \boldsymbol{u} = \dfrac{M^p \beta^q}{R_e}\left(\Delta \boldsymbol{u} + k\nabla(\nabla \cdot \boldsymbol{u})\right) + \boldsymbol{S_u} \\[4mm]
\partial_t \boldsymbol{B} + M^p \beta^q \nabla^{\perp}(\boldsymbol{a} \cdot \boldsymbol{B}^{\perp}) = -\dfrac{1}{R_m}\nabla^{\perp}(rot\boldsymbol{B}) + \boldsymbol{S_b}
\end{cases}
\tag{3.5.108}
$$

We note that in order to have a commuting de Rham sequence, we need to have $\boldsymbol{S_b} \in H(div; \Omega)$, hence $\boldsymbol{S_{bh}} = \Pi_2 \boldsymbol{S_b}$, so $\boldsymbol{S_{bh}} \in V_2$. As for $\boldsymbol{S_u}$, we also need to have $\boldsymbol{S_u} \in H(div; \Omega)$, hence $\boldsymbol{S_{uh}} = \Pi_2 \boldsymbol{S_u}$ and it follows that $\boldsymbol{S_{uh}} \in V_2$. For the source term associated with the pressure equation, $S_p$, we need to have $S_p \in L^2(\Omega)$, so $S_{ph} = \Pi_3 S_p$ and hence $S_{ph} \in V_3$. For brevity, we outline the final formulation (discretized in space and time) that are used to solve model (3.5.108), the spatially and temporally discretized convection-diffusion model is as follows:

We solve for $p_h^{n+1}$ such that $p_h \in V_3$, $\boldsymbol{y}_h \in V_2$ and $\boldsymbol{a}p_h \in H(div;\Omega)$ such that:

$$\begin{cases} \frac{1}{2\Delta t}(3p_h^{n+1} - 4p_h^n + p_h^{n-1}) + M^p\beta^q\nabla \cdot (\Pi_2(\boldsymbol{a}(2p_h^n - p_h^{n-1}))) = \\ \frac{(\gamma-1)M^p\beta^q}{R_e P_r}\nabla \cdot \boldsymbol{y}_h^{n+1} + S_{ph}^n \\ \\ \int_\Omega p_h^{n+1}\nabla \cdot \boldsymbol{w}_h + \int_\Omega \boldsymbol{w}_h \cdot \boldsymbol{y}_h^{n+1} = 0, \quad \forall \boldsymbol{w}_h \in V_2 \end{cases}$$

We solve for $\boldsymbol{B}_h^{n+1}$ such that $\boldsymbol{B}_h \in V_2$, $h_h \in V_0$ and $\boldsymbol{a} \cdot \boldsymbol{B}_h^\perp \in H^1(\Omega)$ such that:

$$\begin{cases} \frac{1}{2\Delta t}(3\boldsymbol{B}_h^{n+1} - 4\boldsymbol{B}_h^n + \boldsymbol{B}_h^{n-1}) + M^p\beta^q\nabla^\perp(\Pi_0(\boldsymbol{a} \cdot (2\boldsymbol{B}_h^{\perp n} - \boldsymbol{B}_h^{\perp n-1}))) = \\ -\frac{1}{R_m}\nabla^\perp h_h^{n+1} + \boldsymbol{S_b}_h^n \\ \\ \int_\Omega \boldsymbol{B}_h^{n+1} \cdot \nabla^\perp f_h - \int_\Omega h_h^{n+1} f_h = 0, \quad \forall f_h \in V_0 \end{cases}$$

We solve for $\boldsymbol{u}_h^{n+1}$ such that $\boldsymbol{u}_h \in V_2$ and $q_h \in V_0$ such that:

$$\begin{cases} \frac{1}{2\Delta t}\int_\Omega(3\boldsymbol{u}_h^{n+1} - 4\boldsymbol{u}_h^n + \boldsymbol{u}_h^{n-1}) \cdot \boldsymbol{v}_h + M^p\beta^q\int_\Omega(2\boldsymbol{u}_h^n - \boldsymbol{u}_h^{n-1}) \cdot \nabla^\perp(\boldsymbol{a}^\perp \cdot \boldsymbol{v}_h) \\ -M^p\beta^q\int_\Omega(\boldsymbol{a} \cdot (2\boldsymbol{u}_h^n - \boldsymbol{u}_h^{n-1}))\nabla \cdot \boldsymbol{v}_h = -\frac{M^p\beta^q}{R_e}\int_\Omega \nabla^\perp q_h^{n+1} \cdot \boldsymbol{v}_h \\ -\frac{M^p\beta^q}{R_e}(1+k)\int_\Omega \nabla \cdot \boldsymbol{u}^{n+1}\nabla \cdot \boldsymbol{v} + \int_\Omega \boldsymbol{S_u}_h^n \cdot \boldsymbol{v}_h, \quad \forall \boldsymbol{v}_h \in V_2 \\ \\ \int_\Omega q_h^{n+1} g_h - \int_\Omega \boldsymbol{u}_h^{n+1} \cdot \nabla^\perp g_h = 0, \quad \forall g_h \in V_0 \end{cases}$$

The source terms are defined as: $\boldsymbol{S_u}_h^n = \frac{1}{\Delta t}\int_\Omega{}_{t_n}^{t_{n+1}}\boldsymbol{S_{uh}}dt$, $S_{ph}^n = \frac{1}{\Delta t}\int_\Omega{}_{t_n}^{t_{n+1}} S_{ph}dt$ and $\boldsymbol{S_b}_h^n = \frac{1}{\Delta t}\int_\Omega{}_{t_n}^{t_{n+1}}\boldsymbol{S_{bh}}dt$.

Due to a limitation that we have in our code implementation, we are not able to apply the projector $\Pi_0$ on products such as $(\boldsymbol{a} \cdot \boldsymbol{B})$ and the same goes for applying $\Pi_2$ on products such as $(\boldsymbol{a}p)$, and we replace both with $L^2$ projections appropriate for each corresponding space.

**Remark 3.5.1.** The $L_2$ projector into $V_0$ for a function f is defined in the following way:

$$\int_\Omega \Pi_0^{L2} f v dx = \int_\Omega f v dx \quad v \in V_0$$

so if F is the matrix of spline coefficients of $\Pi_0^{L2} f$, we have:

$$F = M_0^{-1} \begin{pmatrix} \int_\Omega f \phi_1^0 \\ \vdots \\ \int_\Omega f \phi_{N0}^0 \end{pmatrix}$$

where $M_0$ is the mass matrix defined on $V_0$ and $(\phi_i^0)_{1 \leq i \leq N_0}$ stands for the basis functions defined on $V_0$

**Remark 3.5.2.** The $L_2$ projector into $V_2$ for a function $\boldsymbol{f}$ is defined in the following way:

$$\int_\Omega \Pi_2^{L2} \boldsymbol{f} \cdot \boldsymbol{v} dx = \int_\Omega \boldsymbol{f} \cdot \boldsymbol{v} dx \quad \boldsymbol{v} \in V_2$$

so if F is the matrix of spline coefficients of $\Pi_2^{L2} \boldsymbol{f}$, we have:

$$F = M_2^{-1} \begin{pmatrix} \int_\Omega \boldsymbol{f} \cdot \boldsymbol{\phi}_1^2 \\ \vdots \\ \int_\Omega \boldsymbol{f} \cdot \boldsymbol{\phi}_{N2}^2 \end{pmatrix}$$

where $M_2$ is the mass matrix defined on $V_2$ and $(\boldsymbol{\phi}_i^2)_{1 \leq i \leq N_2}$ stands for the basis functions defined on $V_2$

### 3.5.3.2   Test Case 1: Steady State Solution

Considering that each of the systems of pressure, velocity and magnetic fields are decoupled, we tackle each field separately:

- **The Pressure Equation:** assuming that p has the form:

$$p = \sin(2\pi x) \sin(2\pi y), \quad (x, y) \in \Omega \tag{3.5.109}$$

  Plugging in (3.5.109) into the pressure equation of (3.5.108) and ignoring the constant coefficients (set all constants to 1), we get the source term for the pressure equation:

$$\begin{cases} S_p = 8\pi^2 \sin(2\pi x) \sin(2\pi y) + 2a_1 \pi \cos(2\pi x) \sin(2\pi y) \\ +2a_2 \pi \sin(2\pi x) \cos(2\pi y), \quad (x, y) \in \Omega \end{cases} \tag{3.5.110}$$

- **The Magnetic Field Equation:** assuming that the magnetic field has the following form:

$$\begin{cases} B_1 = \cos(2\pi x)\sin(2\pi y), & (x,y) \in \Omega \\ B_2 = -\sin(2\pi x)\cos(2\pi y), & (x,y) \in \Omega \end{cases} \tag{3.5.111}$$

and ignoring the constant coefficients (set all constants to 1), we get the source term for the magnetic equation:

$$\begin{cases} Sb_1 = 8\pi^2 \cos(2\pi x)\sin(2\pi y) + 2\pi a_1 \cos(2\pi x)\cos(2\pi y) \\ \quad +2\pi a_2 \sin(2\pi x)\sin(2\pi y), \quad (x,y) \in \Omega \\ Sb_2 = -8\pi^2 \sin(2\pi x)\cos(2\pi y) + 2\pi a_1 \sin(2\pi x)\sin(2\pi y) \\ \quad +2\pi a_2 \cos(2\pi x)\cos(2\pi y), \quad (x,y) \in \Omega \end{cases} \tag{3.5.112}$$

- **The Velocity Equation:** we consider here a test case for the advection and ignoring the diffusion terms of the velocity equation, an assumed solution that satisfies the needed BC conditions is:

$$\begin{cases} u_1 = \sin(2\pi x)\sin(2\pi y), & (x,y) \in \Omega \\ u_2 = \sin(2\pi x)\sin(2\pi y), & (x,y) \in \Omega \end{cases} \tag{3.5.113}$$

Then the corresponding source term ignoring the constant coefficients:

$$\begin{cases} Su_1 = 2\pi a_1 \cos(2\pi x)\sin(2\pi y) + 2\pi a_2 \sin(2\pi x)\cos(2\pi y), & (x,y) \in \Omega \\ Su_2 = 2\pi a_1 \cos(2\pi x)\sin(2\pi y) + 2\pi a_2 \sin(2\pi x)\cos(2\pi y), & (x,y) \in \Omega \end{cases} \tag{3.5.114}$$

Fig. (3.17), presents the convergence rates setting the diffusive component of the velocity equation to zero and considering $\boldsymbol{a} = (0.1, 0.1)$, where the numerical solutions are convergent with order 2 as expected. The assumed steady state solution is Eq. (3.5.109), Eq. (3.5.111) and Eq. (3.5.113).

(A) p      (B) $B_1$      (C) $B_2$



(D) $u_1$      (E) $u_2$
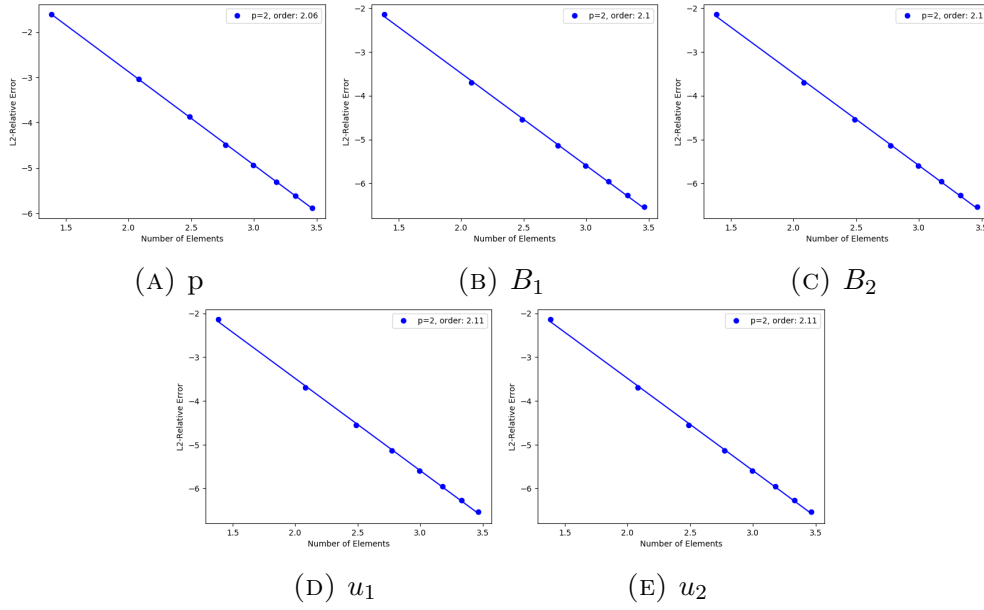
FIGURE 3.17: Convergence orders for the convection-diffusion system with a source term in steady state with $\boldsymbol{a} = (0.1, 0.1)$ and ignoring the diffusive component of the velocity equation and B-splines degree 2.

### 3.5.3.3 Test Case 1: Time Dependent Solution

In this section, we consider a time dependent solution:

- **The Pressure Equation:** assuming that the pressure has the form:

$$p = e^{-\pi t} \sin(2\pi x) \sin(2\pi y), \quad (x, y) \in \Omega, t \in [0, T] \tag{3.5.115}$$

Plugging in (3.5.115) into the pressure equation of (3.5.108) and ignoring the constant coefficients (set all constants to 1), we get the source term for the pressure equation:

$$\begin{cases} S_p = (-\pi + 8\pi^2)e^{-\pi t} \sin(2\pi x) \sin(2\pi y) + 2a_1\pi \cos(2\pi x) \sin(2\pi y)e^{-\pi t} \\ +2a_2\pi \sin(2\pi x) \cos(2\pi y)e^{-\pi t}, \quad (x, y) \in \Omega, t \in [0, T] \end{cases} \tag{3.5.116}$$

- **The Magnetic Field Equation:** assuming that the magnetic field has the following form:

$$\begin{cases} B_1 = \quad e^{-\pi t} \cos(2\pi x) \sin(2\pi y), \quad (x, y) \in \Omega, t \in [0, T] \\ B_2 = -e^{-\pi t} \sin(2\pi x) \cos(2\pi y), \quad (x, y) \in \Omega, t \in [0, T] \end{cases} \tag{3.5.117}$$

Then the corresponding source term ignoring the constant coefficients (set all constants to 1) for the magnetic equation:

$$
\begin{cases}
Sb_1 = (-\pi + 8\pi^2)e^{-\pi t}\cos(2\pi x)\sin(2\pi y) + 2\pi a_1\cos(2\pi x)\cos(2\pi y)e^{-\pi t} \\
+2\pi a_2\sin(2\pi x)\sin(2\pi y)e^{-\pi t}, \quad (x,y) \in \Omega, t \in [0,T] \\
Sb_2 = (\pi - 8\pi^2)e^{-\pi t}\sin(2\pi x)\cos(2\pi y) + 2\pi a_1\sin(2\pi x)\sin(2\pi y)e^{-\pi t} \\
+2\pi a_2\cos(2\pi x)\cos(2\pi y)e^{-\pi t}, \quad (x,y) \in \Omega, t \in [0,T]
\end{cases}
$$

$$(3.5.118)$$

- **The Velocity Equation:** we consider here a time dependent test case for the advection and ignoring the diffusion terms of the velocity equation, an assumed solution that satisfies the needed BC conditions is:

$$
\begin{cases}
u_1 = e^{-\pi t}\sin(2\pi x)\sin(2\pi y), \quad (x,y) \in \Omega, t \in [0,T] \\
u_2 = e^{-\pi t}\sin(2\pi x)\sin(2\pi y), \quad (x,y) \in \Omega, t \in [0,T]
\end{cases}
$$

$$(3.5.119)$$

Then the corresponding source term ignoring the constant coefficients

$$
\begin{cases}
Su_1 = (-\pi + 12\pi^2)e^{-\pi t}\sin(2\pi x)\sin(2\pi y) - e^{-\pi t}4\pi^2\cos(2\pi x)\cos(2\pi y) \\
+2\pi e^{-\pi t}(a_1\cos(2\pi x)\sin(2\pi y) + a_2\sin(2\pi x)\cos(2\pi y)), \quad (x,y) \in \Omega, t \in [0,T] \\
Su_2 = (-\pi + 12\pi^2)e^{-\pi t}\sin(2\pi x)\sin(2\pi y) - e^{-\pi t}4\pi^2\cos(2\pi x)\cos(2\pi y) \\
+2\pi e^{-\pi t}(a_1\cos(2\pi x)\sin(2\pi y) + a_2\sin(2\pi x)\cos(2\pi y)), \quad (x,y) \in \Omega, t \in [0,T]
\end{cases}
$$

$$(3.5.120)$$

Fig. (3.18) presents the convergence rates where one can see that the numerical solutions are convergent. The assumed time dependent solution is (3.5.115, 3.5.117, 3.5.119).

(A) p

(B) $B_1$

(C) $B_2$

(D) $u_1$

(E) $u_2$
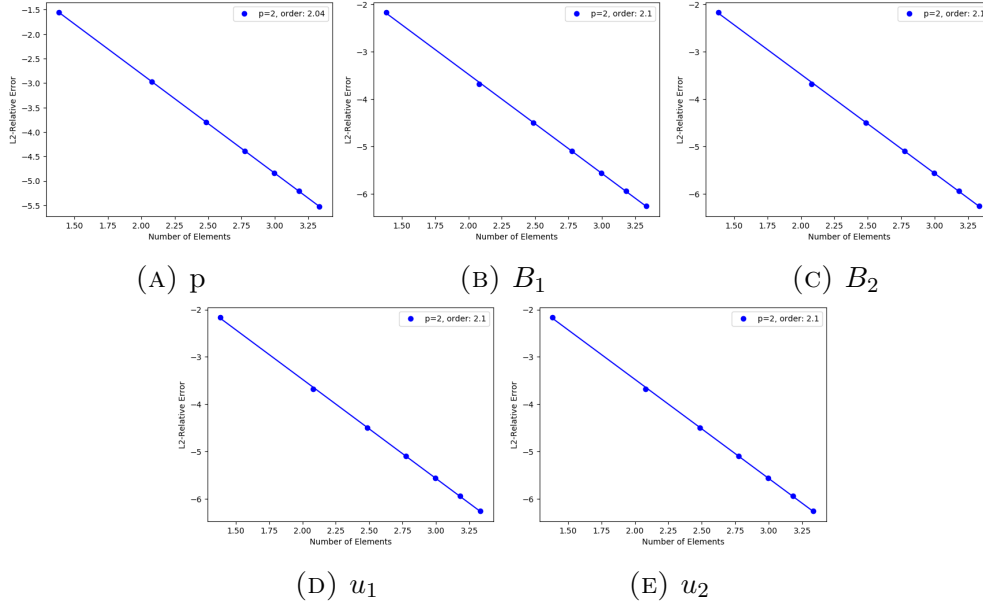
FIGURE 3.18: Convergence orders for the convection-diffusion system with a time dependent source term with ($\boldsymbol{a} = (0.1, 0.1)$) and ignoring the diffusive component of the velocity equation with B-splines degree 2.

For studying the divergence-free condition, we propose a different time dependent solution for the magnetic equation; one that doesn't have the decaying exponential temporal component but rather a sinusoidal time dependency in order to be able to track $\nabla \cdot B_h^n$ through a long time run. The choice of the assumed solution for the magnetic field is as follows:

$$\begin{cases} B_1 = \cos(t) \cos(2\pi x) \sin(2\pi y), & (x, y) \in \Omega, t \in [0, T] \\ B_2 = -\cos(t) \sin(2\pi x) \cos(2\pi y), & (x, y) \in \Omega, t \in [0, T] \end{cases} \quad (3.5.121)$$

Ignoring the constant coefficients, the corresponding source terms are:

$$\begin{cases} Sb_1 = (-\sin(t) + 8\pi^2 \cos(t)) \cos(2\pi x) \sin(2\pi y) + 2\pi a_1 \cos(2\pi x) \cos(2\pi y) \cos(t) \\ +2\pi a_2 \sin(2\pi x) \sin(2\pi y) \cos(t), & (x, y) \in \Omega, t \in [0, T] \\ Sb_2 = (\sin(t) - 8\pi^2 \cos(t)) \sin(2\pi x) \cos(2\pi y) + 2\pi a_1 \sin(2\pi x) \sin(2\pi y) \cos(t) \\ +2\pi a_2 \cos(2\pi x) \cos(2\pi y) \cos(t), & (x, y) \in \Omega, t \in [0, T] \end{cases} \quad (3.5.122)$$

Fig. (3.19) shows the divergence of the magnetic field at the discrete level considering a time dependent solution for the magnetic field as is shown in Eq. (3.5.121). The divergence of the magnetic field is preserved up to $1 \times 10^{-14}$.
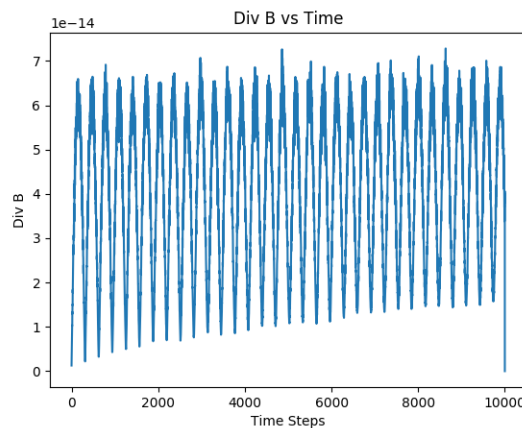
FIGURE 3.19: $\nabla \cdot B_h^n$ for a time dependent solution with B-splines' degree 2 and dt $= 0.01$ and 1000 time steps.

## 3.6 Numerical Results for Linear MHD

In order to test the splitting scheme introduced in section (3.2) for the linear MHD model (the combination of the acoustic, magnetic and convective steps), we use the method of manufactured solution to find a suitable test case as we don't have an exact solution in closed form of the set of equations. For that we use a first order in time splitting with a first order time scheme for each sub step, namely, the acoustic, magnetic and convective steps. We proceed by denoting the acoustic step by A, the magnetic step by M and the convection-diffusion step by C. The ordering of the steps used while solving the linear MHD model is as follows:

$$\psi(\Delta t) = M(\Delta t) \circ C(\Delta t) \circ A(\Delta t)$$

where $\psi$ is the full time scheme for the linear MHD. So we start by solving the acoustic step, where we have the pressure and the velocity coupled in model (3.3.23) with an appropriate initialization. The output of this step, is used as an input for the convection-diffusion step, model (3.5.83), but keeping in mind that the input for the magnetic equation of the convection-diffusion step is that of the initialization. Once we solve the convection-diffusion step, we use the output of the velocity and the magnetic fields as an input to the magnetic step. The output of this first time step is both the magnetic and velocity fields resulting from the magnetic step, and the pressure coming from the convection-diffusion step, and then we repeat for each time step. Note that the order of the steps is chosen randomly.

### 3.6.1 Test Case 1: Steady State Manufactured Solution

In this case, we assume a solution for the pressure, magnetic and velocity fields and compute the source terms as we did previously. For our splitting scheme, we also choose to have the source terms resulting from the three steps as a RHS for the convection-diffusion step. This way, we can insure that we are testing the splitting, rather than solving each step separately.

The exact solution for the pressure is:

$$p = \sin(2\pi x)\sin(2\pi y), \quad (x, y) \in \Omega \tag{3.6.123}$$

The exact solution for the magnetic field is:

$$\begin{cases} B_1 = \cos(2\pi x)\sin(2\pi y), & (x, y) \in \Omega \\ B_2 = -\sin(2\pi x)\cos(2\pi y), & (x, y) \in \Omega \end{cases} \tag{3.6.124}$$

While for the velocity, we consider a test case including the advection and excluding the diffusion component:

$$\begin{cases} u_1 = \sin(2\pi x)\sin(2\pi y), & (x, y) \in \Omega \\ u_2 = \sin(2\pi x)\sin(2\pi y), & (x, y) \in \Omega \end{cases} \tag{3.6.125}$$

We plug in (3.6.123), (3.6.124) and (3.6.125) into the linear MHD model (3.6.126) considering that we have source terms as follows:

$$\begin{cases} \partial_t p + M^p\beta^q \boldsymbol{a} \cdot \nabla p + \gamma M^p\beta^q \nabla \cdot \boldsymbol{u} - \dfrac{(\gamma-1)M^p\beta^q}{R_e P_r}\nabla \cdot (\nabla p) = S_p \\[2em] \partial_t \boldsymbol{u} + M^p\beta^q \boldsymbol{a} \cdot \nabla \boldsymbol{u} + \dfrac{\beta^q}{\gamma M^{2-p}}\nabla p - \dfrac{1}{M^{2-p}\beta^{1-q}}(rot\boldsymbol{B})\mathbf{b}^\perp \\ \quad - \frac{M^p\beta^q}{R_e}\left(\Delta \boldsymbol{u} + k\nabla(\nabla \cdot \boldsymbol{u})\right) = \boldsymbol{S_u} \\[2em] \partial_t \boldsymbol{B} + M^p\beta^q \nabla^\perp(\boldsymbol{a} \cdot \boldsymbol{B}^\perp) - M^p\beta^q \nabla^\perp(\boldsymbol{u} \cdot \mathbf{b}^\perp) + \dfrac{1}{R_m}\nabla^\perp(rot\boldsymbol{B}) = \boldsymbol{S_b} \end{cases} \tag{3.6.126}$$

We neglect the constant coefficients, and hence the corresponding source terms are:

$$\begin{cases} S_p = 2\pi \cos(2\pi x)\sin(2\pi y) + 2\pi \sin(2\pi x)\cos(2\pi y) + 8\pi^2 \sin(2\pi x)\sin(2\pi y) \\ +2a_1\pi \cos(2\pi x)\sin(2\pi y) + 2a_2\pi \sin(2\pi x)\cos(2\pi y), \quad (x, y) \in \Omega \end{cases} \tag{3.6.127}$$

$$\begin{cases} S_{B_1} = 2\pi(b_1 - b_2)\sin(2\pi x)\cos(2\pi y) + 8\pi^2\cos(2\pi x)\sin(2\pi y) \\ \quad +2\pi a_1\cos(2\pi x)\cos(2\pi y) + 2\pi a_2\sin(2\pi x)\sin(2\pi y), \quad (x,y) \in \Omega \\ S_{B_2} = -2\pi(b_1 - b_2)\cos(2\pi x)\sin(2\pi y) - 8\pi^2\sin(2\pi x)\cos(2\pi y) \\ \quad +2\pi a_1\sin(2\pi x)\sin(2\pi y) + 2\pi a_2\cos(2\pi x)\cos(2\pi y), \quad (x,y) \in \Omega \end{cases} \qquad (3.6.128)$$

$$\begin{cases} S_{u_1} = 2\pi\cos(2\pi x)\sin(2\pi y) - 4\pi b_2\cos(2\pi x)\cos(2\pi y) \\ \quad +12\pi^2\sin(2\pi x)\sin(2\pi y) - 4\pi^2\cos(2\pi x)\cos(2\pi y) \\ \quad +2\pi a_1\cos(2\pi x)\sin(2\pi y) + 2\pi a_2\sin(2\pi x)\cos(2\pi y), \quad (x,y) \in \Omega \\ S_{u_2} = 2\pi\sin(2\pi x)\cos(2\pi y) + 4\pi b_1\cos(2\pi x)\cos(2\pi y) \\ \quad +12\pi^2\sin(2\pi x)\sin(2\pi y) - 4\pi^2\cos(2\pi x)\cos(2\pi y) \\ \quad +2\pi a_1\cos(2\pi x)\sin(2\pi y) + 2\pi a_2\sin(2\pi x)\cos(2\pi y), \quad (x,y) \in \Omega \end{cases} \qquad (3.6.129)$$

Fig. (3.20) presents the convergence orders for the steady state case neglecting the diffusive component of the velocity equation. It is to note that we have used a first order splitting with a first order in time scheme, with $b^\perp = (1,1)$. We can see that the numerical solutions are convergent.



(A) p    (B) $B_1$    (C) $B_2$

(D) $u_1$    (E) $u_2$
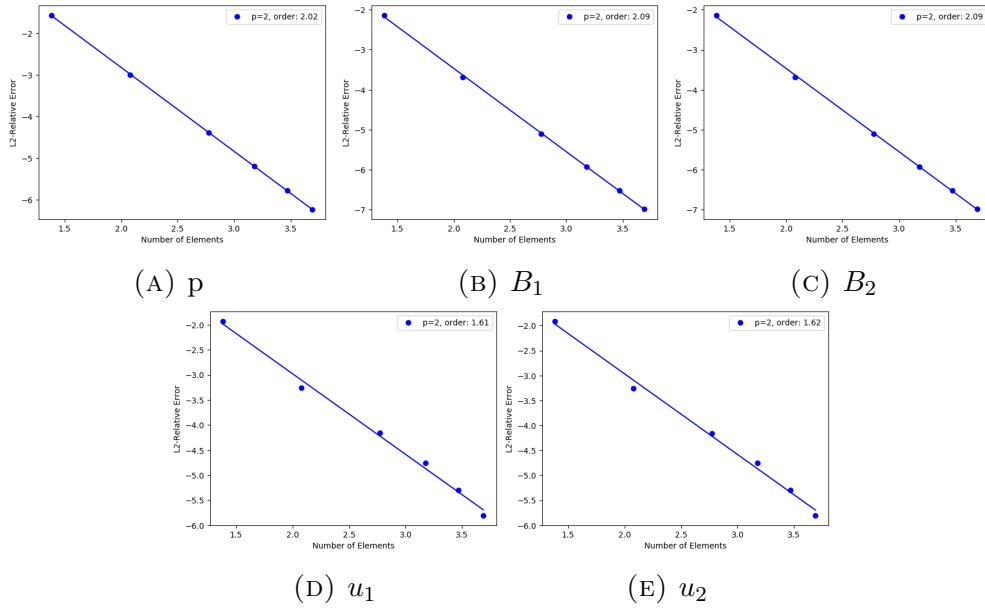
FIGURE 3.20: Convergence rates for the pressure, magnetic field and velocity for the linear MHD model considering advection for the velocity component and no diffusion for the velocity, with $b^\perp = (1,1)$

We include in Fig. (3.21) the plot for $\nabla \cdot B_h^n$ for the case of steady state manufactured solution with a background magnetic field of $\mathbf{b}^\perp = (1.0, 1.0)$ and $\mathbf{b}^\perp = (0.7, 0.3)$ and ignoring the diffusion component of the velocity equation, where we can see that the divergence of the magnetic field is preserved up to $10^{-13}$ in both cases.

(A) $b_\perp = (1.0, 1.0)$      (B) $b_\perp = (0.7, 0.3)$
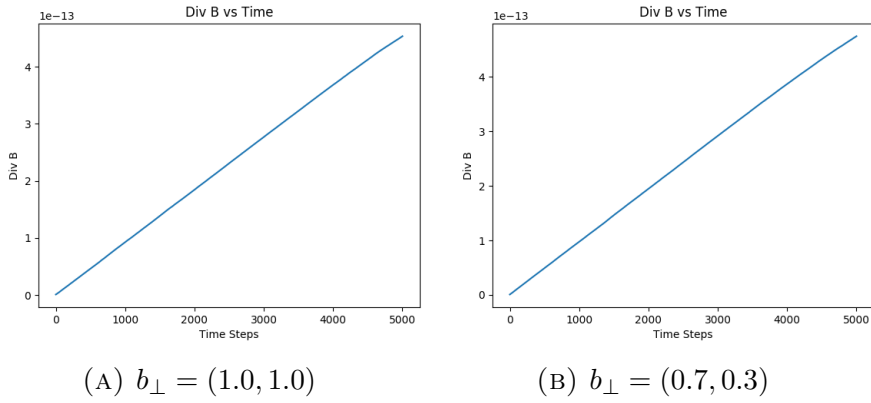
FIGURE 3.21: $\nabla \cdot \boldsymbol{B}_h^n$ over time considering a steady state solution for the linear MHD model with 8 elements in each direction, dt = 0.001 and final time 5s.

## 3.6.2 Test Case 2: Acoustic Wave Propagation

For this test case, we initialize the pressure with a gaussian:

$$p = \frac{1}{2\pi\sigma^2}exp(-\frac{(x - 0.5)^2 + (y - 0.5)^2}{2\sigma^2}), \quad (x, y) \in \Omega \tag{3.6.130}$$

where we take $\sigma = \frac{1}{\sqrt{200}}$ and initialize the velocity and the magnetic field to zero:

$$\boldsymbol{u} = \boldsymbol{B} = 0 \tag{3.6.131}$$

The goal of the test case is to inspect if the wave propagates as expected qualitatively and to observe the divergence-free condition. We start by presenting a contour plot of the pressure as can be seen in Fig. (3.22), starting from the initialization till the final time step. The contour plot is for the case of background magnetic field of $\mathbf{b}^\perp = (1.0, 1.0)$, and we can see that the "stretching" of the pulse is going diagonally according to what we expect from such a configuration.



FIGURE 3.22: A contour plot of the pressure profile evolution initialized as a gaussian pulse for the linear MHD model with $\mathbf{b}^\perp = (1.0, 1.0)$ and $\boldsymbol{a} = 0.1$.

We present in Fig. (3.23) the divergence of the magnetic field considering Test Case 2 (acoustic wave propagation) including advection and neglecting the diffusion in the velocity equation. Fig. (3.23a) and Fig. (3.23b) show the divergence for $b^\perp = (0.7, 0.3)$ and $b^\perp = (1.0, 1.0)$, respectively. We can see that in both cases that the divergence is preserved up to $10^{-15}$. Fig. (3.24) on the other hand, presents the results on the divergence of the magnetic field in the case of no advection and including the diffusion on the velocity. For both cases of the magnetic field configurations, $b^\perp = (0.7, 0.3)$ and $b^\perp = (1.0, 1.0)$, the divergence is preserved up to $10^{-14}$, as can be seen in Fig. (3.24a) and Fig. (3.24b), respectively.



(A) $b^\perp = (0.7, 0.3)$         (B) $b^\perp = (1.0, 1.0)$
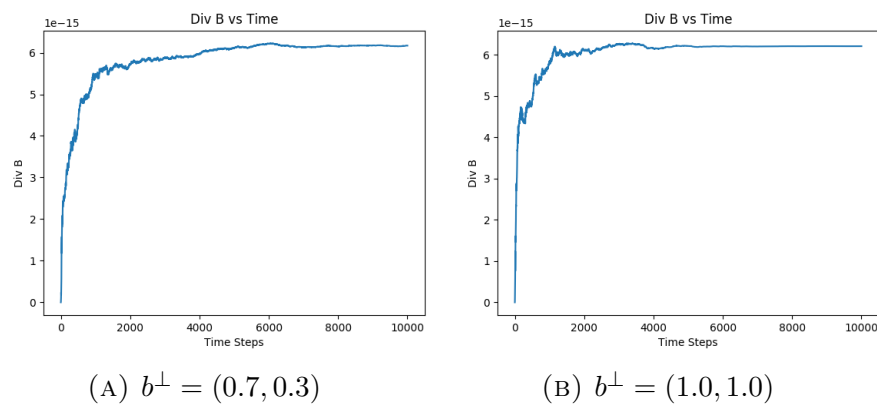
FIGURE 3.23: $\nabla \cdot \boldsymbol{B}_h^n$ over time considering the acoustic wave propagation test case for the linear MHD model with advection ($\boldsymbol{a} = (0.1, 0.1)$) and no diffusion for the velocity with 8 elements in each direction, dt = 0.001 and final time 5s.



(A) $b^\perp = (1.0, 1.0)$         (B) $b^\perp = (0.7, 0.3)$
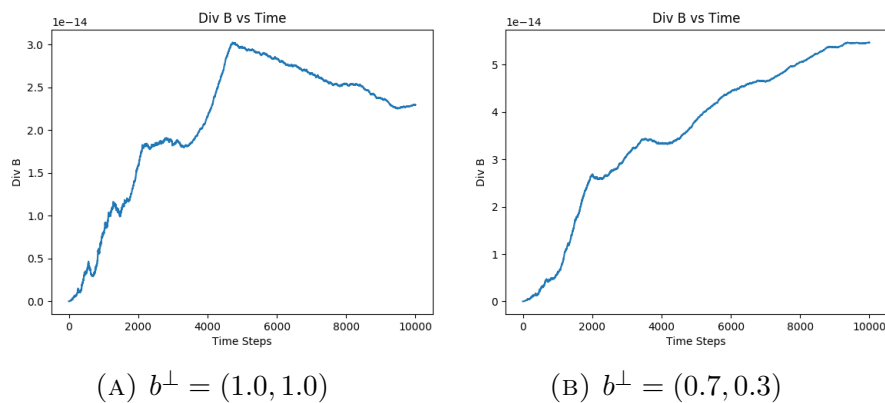
FIGURE 3.24: $\nabla \cdot \boldsymbol{B}_h^n$ over time considering the acoustic wave propagation test case for the linear MHD model without advection for the velocity and including the diffusive component with 8 elements in each direction, dt = 0.001 and final time 5s.

Fig. (3.25) shows how the pressure diffuses in the absence of advection, as the pressure is initialized with a gaussian pulse. We note the oval shape of the diffused

pulse has a diagonal axis, as we expect from the assumed background magnetic field configuration, namely $b_{\perp} = (1.0, 1.0)$. Looking at Fig. (3.26), we can also see how the diffusion is taking place, only in this case the axis of the oval shaped pulse is not diagonal, as the expected from the background magnetic field $b_{\perp} = (0.7, 0.3)$.
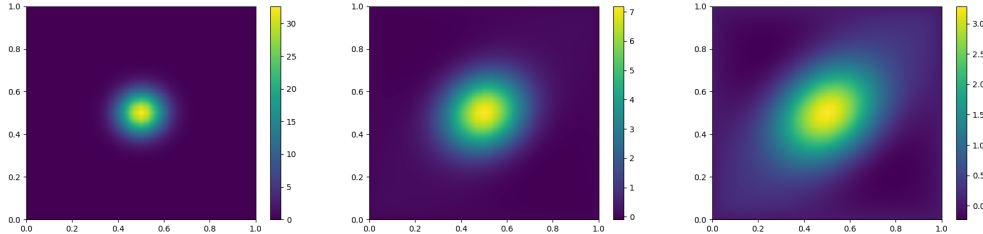


FIGURE 3.25: A contour plot of the pressure profile evolution initialized as a gaussian pulse for the linear MHD model with $\mathbf{b}^{\perp} = (1.0, 1.0)$ and $\boldsymbol{a} = 0.0$.
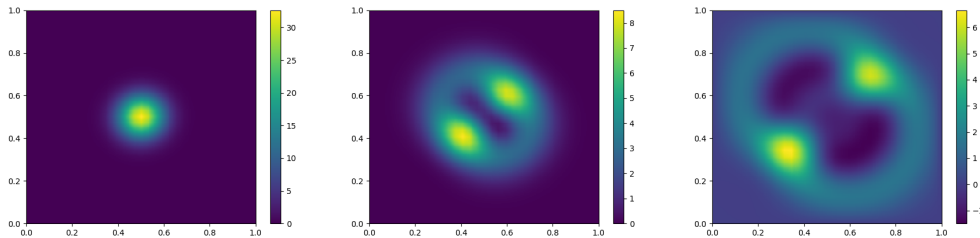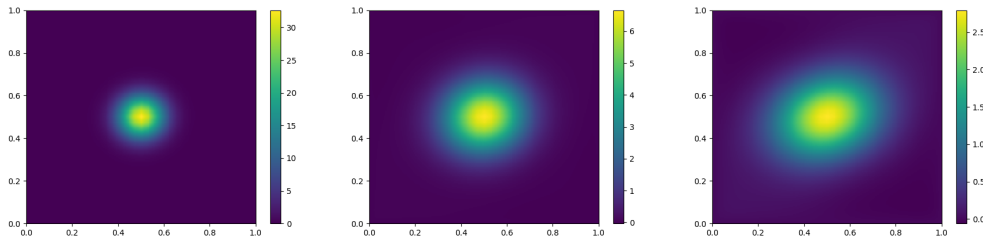


FIGURE 3.26: A contour plot of the pressure profile evolution initialized as a gaussian pulse for the linear MHD model with $\mathbf{b}^{\perp} = (0.7, 0.3)$ and $\boldsymbol{a} = 0.0$.

## 3.7 Conclusions

In this Chapter, we have derived the linear MHD model in a context simplified in comparison to the Tokamak context and analysed the different scales present in the model, as a result of the different propagating waves. This lead us to devise a three-way energy-preserving splitting; the acoustic step, the magnetic step and the convection-diffusion step.

For the acoustic step, we have suggested two set of choices for the spaces of the state variables, the pressure and the velocity. We discretized the system spatially

and temporally using compatible FE spaces in the framework of FEEC and presented the convergence rates, the energy preservation and the vorticity-free condition for two test cases. As one can see in section (3.3.5), the convergence rates adhere with what is expected theoretically. Also, the energy is preserved for the test cases analysed and the vorticity is preserved for formulation $H(rot; \Omega) - H^1(\Omega)$. We followed similar steps for the magnetic step, but make the case for resorting to an implementation that leads to the preservation of the divergence-free condition, but not the energy conservation. This comes as a result of a limitation in our code implementation, that doesn't allow us to apply the commuting projection on the test basis functions. The numerical results presented in section (3.4.4) do correspond to this theoretical foundation, where we have found that the divergence-free condition is preserved, but not the total energy. The convergence rates are included, and are what is expected from a theoretical point of view.
The convection-diffusion step has been treated in a similar manner to the acoustic and magnetic steps. The system was solved numerically with appropriate test cases, and the convergence rates found correspond to what we expect from theory. We also included the divergence of the magnetic field at the discrete level which was found to be preserved.

# Chapter 4

# Multigrid and GLT Preconditioning

## 4.1 Introduction

Discretizing systems of partial differential equations by classical discretization methods like FE, FV and FE leads to algebraic linear systems. Inverting and hence solving such systems can be a computationally expensive matter. Usually using an iterative solver is more favourable, due to the sparsity of the resultant matrix and taking into account that the system is usually of a large size. The convergence of iterative solvers is dependent on the condition number of the resultant matrix, and it is well understood that a large condition number leads to a bad convergence rate. The other criteria to take into account while choosing an iterative solver is the sensitivity of the solver to the spectral radius of the resultant matrix. Applying Fourier analysis on the discretized system shows that errors with high frequency are damped faster than the low frequency errors, and this leads to the slowing down of the convergence rate. Isogeometric analysis leads to large linear systems as a result of the Galerkin approximation based on B-splines [27].

In what follows, we give a quick introduction to Multigrid (MG) Methods and their use to solve the above mentioned problem of the slowing down of the convergence rate. We proceed to lay the ground to a newly developed theory, namely Generalized Locally Toeplitz Theory and its use as a preconditioner to remedy the pathologies arising from the discretization of d-dimensional elliptic problems. The final goal is to design an iterative algorithm with the following two properties:

- Optimality: that is the computational cost is linear with respect to the degrees of freedom of the resultant matrix.

- Robustness in the sense that the convergence rate is independent of the relevant parameters of the system (i.e., matrix size and spline degree)

The theoretical framework outlined for the GLT part is heavily reliant on the work presented in [61, 60, 66]. We end the chapter by presenting results of using MG and GLT applied to the Poisson equation where we see how using the GLT as a preconditionder for the MG reduces the computational cost significantly considering the number of cycles needed to reach convergence and the time required to invert the system. We include an eigenvalue analysis related to the anisotropic equation through the usage of GLT symbols.

## 4.2   Multigrid Methods

MG methods are a class of algorithms for solving PDEs and ODEs with a hierarchy of dicretizations. MG could be used both as solvers as well as preconditioners. The main idea of the MG as a preconditioner is to speed-up the convergence of basic iterative solvers, which manages to reduce high frequency error components. This is achieved by introducing a correction to the fine grid solution approximation through solving a system on the coarse grid. Although the linear system at the coarse level is cheaper to solve than the full problem, it bears the same property that it contains both high and low frequency components, so we can repeat the above mentioned process recursively till we reach a satisfactory problem size that we can solve directly and the problem of the high and low frequency components is resolved. A common application of MG is in the solution of elliptic PDEs and the advantages are seen mainly in 2D or 3D [49].

### 4.2.1   Two Grid Cycle

The first MG method that we consider here is the Two Grid Method (TGM), which involves, naturally, two grids. TGM starts with a classic smoother, like Jacobi's or Gauss-Seidel on the fine grid. This step leads to an approximation of the solution $\boldsymbol{u}$ where the high frequency error components are dealt with appropriately. After that the MG transfers the residual calculated on the fine grid to the coarse grid, solving the problem directly and creating a correction term that is then transferred back to the fine grid and this is used to correct the original approximation [49]. Let $A_{\boldsymbol{m}}\boldsymbol{u} = \boldsymbol{b}$ be the linear system we want to solve, with $\boldsymbol{u}, \boldsymbol{b} \in \mathbb{R}^N$ and $A_{\boldsymbol{m}} \in \mathbb{R}^{N \times N}$ symmetric positive definite matrix. An iterative method can be applied

either directly to this system, or to the error equation, what is also referred to in literature as the residual equation. Let $\tilde{u}$ be an approximation of $u$, then the error $e = u - \tilde{u}$ satisfies the residual equation:

$$A_m e = b - A_m \tilde{u} =: r \qquad (4.2.1)$$

Considering a fine and a coarse grid, an outline of a simple TGM algorithm:

---

**Algorithm**

1. **Iterate** on $A_f u = b_f$ to reach $u_f$ (in our case, 5 Gauss-Seidel steps).

2. **Restrict** the residual $r_f = b_f - A_f u_f$ to the coarse grid by $r_c = R r_f$

3. **Solve** $A_c e_c = r_c$ (or come close to $e_c$ by 5 iterations from $e = 0$).

4. **Interpolate** $e_c$ back to $e_f = P e_c$. Add $e_f$ to $u_f$.

5. **Iterate** 5 more times on $A_f u = b_f$ starting from the improved solution $u_f + e_f$.

We use the subscript "f" to indicate the fine grid, whereas we use the subscript "c" to indicate the coarse grid. R and P are the restriction and prolongation operators respectively.

---

More details on the construction of the prolongation and restriction operators and the choice of the smoothers in the context of the GLT preconditioner are found in section (4.3.5).

## 4.2.2 V-cycle and Computational Cost

The two grid cycle is not the only way to benefit from MGM. Actually, the advantages of MG become more apparent once we move to more levels. The low frequency components of the error are still low on the 2h grid (considering we are halving the fine grid, where h is the step size), and one can see that moving to a coarser grid (4h, 8h or 16h) would make that component of the error to decay faster. The advantage of MG becomes clearer when considering its computational cost.

MG often scales linearly with the size of the problem. The number of operations performed in the V-Cycle on each grid is proportional to the mesh size. This comes as a result that each process involved in the MG-relaxation, residual computation,

restriction and prolongation-scales linearly with the mesh size. The total number of operations per V-Cycle is greater than the number of operations performed on the finest grid by a constant factor, this is because the number of variables at each subgrid is a fraction of that of the finest grid. Thus the number of required operations is merely O(N) [49].

## 4.3 GLT

We begin by introducing some mathematical definitions that are necessary for understanding the GLT theory.

### 4.3.1 Unilevel and multilevel Toeplitz matrix-sequences

**Definition 4.1.** A (unilevel) Toeplitz matrix is a real/complex valued $n \times n$ matrix $T_n = [t_{ij}]_{i,j=0,\ldots,n-1}$, where $t_{ij} = t_{i-j}$, i.e.,

$$T_n = \begin{pmatrix} t_0 & t_{-1} & t_{-2} & \ldots & t_{-(n-1)} \\ t_1 & t_0 & t_{-1} & \ldots & \\ t_2 & t_1 & t_0 & \ldots & \vdots \\ \vdots & & & \ddots & \\ t_{n-1} & \ldots & & \ldots & t_0 \end{pmatrix}.$$

Any function $f \in L^1([-\pi,\pi])$ can be decomposed into a Fourier series:

$$f(\theta) = \sum_{j \in \mathbb{Z}} t_j e^{ij\theta}, \quad \forall \theta \in [-\pi,\pi],$$

where

$$t_j = \frac{1}{2\pi} \int_{-\pi}^{\pi} f(\theta) e^{-ij\theta} \, d\theta,$$

hence, the sequence $\{t_j\}_j$ determines uniquely the function $f$. Therefore, the function $f$, if it exists, is also uniquely determined by the sequence of the Toeplitz matrices $\{T_n(f)\}_n$ with

$$T_n(f) = [t_{i-j}]_{i,j=0,\ldots,n-1}.$$

When the function $f \in L^1([-\pi, \pi]^d)$, the associated sequence is made of the so called *multilevel Toeplitz matrices*, that is matrices which 'at each level' are Toeplitz matrices. For example, a 2-level matrix is a block Toeplitz whose blocks are still Toeplitz. Let $\boldsymbol{n} := (n_1, \ldots, n_d)$ be a multi-index in $\mathbb{N}^d$ and set $N(\boldsymbol{n}) := \prod_{i=1}^d n_i$. Note that the number of levels will be related to the dimensionality of the problem in the following applications. The formal definition of $d$-level Toeplitz sequence associated to $f$ is the following:

**Definition 4.2.** Let the Fourier coefficients of a given function $f \in L^1([-\pi, \pi]^d)$ be defined as

$$t_{\boldsymbol{j}} := \frac{1}{(2\pi)^d} \int_{[-\pi,\pi]^d} f(\boldsymbol{\theta}) \mathrm{e}^{-\mathrm{i}\langle \boldsymbol{j}, \boldsymbol{\theta} \rangle} \, d\boldsymbol{\theta}, \quad \boldsymbol{i} = (i_1, \ldots, i_d) \in \mathbb{Z}^d, \quad \boldsymbol{j} = (j_1, \ldots, j_d) \in \mathbb{Z}^d,$$

$$\boldsymbol{\theta} = (\theta_1, \ldots, \theta_d) \in [-\pi, \pi]^d,$$

where $\langle \boldsymbol{j}, \boldsymbol{\theta} \rangle = \sum_{r=1}^d j_r \theta_r$. Then, the $\boldsymbol{n}^{th}$ Toeplitz matrix associated with $f$ is the matrix of order $N(\boldsymbol{n})$ given by

$$T_{\boldsymbol{n}}(f) = [t_{\boldsymbol{i}-\boldsymbol{j}}]_{\boldsymbol{i},\boldsymbol{j}=1}^{\boldsymbol{n}} = \sum_{|j_1|<n_1} \cdots \sum_{|j_d|<n_d} t_{\boldsymbol{j}} \left[ J_{n_1}^{(j_1)} \otimes \cdots \otimes J_{n_d}^{(j_d)} \right]$$

where $\boldsymbol{i} = (i_1, \ldots, i_d) \in \mathbb{N}^d, \boldsymbol{j} = (j_1, \ldots, j_d) \in \mathbb{N}^d$. The term $J_m^{(l)}$ is the matrix of order $m$ whose $(i, j)$ entry equals 1 if $i - j = l$ and zero otherwise. The set $\{T_{\boldsymbol{n}}(f)\}_{\boldsymbol{n}}$ is called the family of $d$-level Toeplitz matrices generated by $f$, that in turn is referred to as the generating function or the symbol of $\{T_{\boldsymbol{n}}(f)\}_{\boldsymbol{n}}$. As a simple example, we consider the generating function $f(s) = 2 - 2cos(s)$, coming from $-u''(x) = G(x)$ defined on the boundary $(0,1)$ with Dirichlet boundary conditions. Then, the n-th Toeplits matrix, $T_n(f)$ is defined as:

$$T_n = \begin{pmatrix} 2 & -1 & & & \\ -1 & 2 & -1 & & \\ & -1 & \ddots & \ddots & \\ & & \ddots & \ddots & -1 \\ & & & -1 & 2 \end{pmatrix}.$$

## 4.3.2 Summary of the theory of GLT sequences

In what follows, we recall the basic properties of the GLT. More details can be found in the pioneering work by Tilli [66] focused on the spectrum of one-dimensional differential operators and in [61, 60] containing a generalization to multivariate differential operators.

As described in [61, 60], a GLT sequence $\{A_n\}_n$ is a sequence of matrices of increasing size. Each GLT sequence is *associated* to a *complex-valued* Lebesgue-measurable function $\kappa$, which is known as the *symbol* of the sequence $\{A_n\}_n$. In this case, we note $\{A_n\}_n \sim_{\text{GLT}} \kappa$. The domain of definition $D$ of the symbol is taken as $[0,1]^d \times [-\pi,\pi]^d$ while a point in $D$ is denoted as $(\boldsymbol{x}, \boldsymbol{\theta})$, where $\boldsymbol{x} = (x_1, \ldots, x_d)$ are the *physical variables* and $\boldsymbol{\theta} = (\theta_1, \ldots, \theta_d)$ are the *Fourier variables*.

**Proposition 4.3.** *We recall the following properties of a GLT sequence $\{A_n\}_n$ :*

1. *If $d_n$ is the size of the matrix $A_n$ and $\{\sigma_1(A_n), \ldots, \sigma_{d_n}(A_n)\}$ are the singular values of $A_n$, then $\forall F \in \mathcal{C}_c(\mathbb{C}, \mathbb{C})$, we have*

$$\lim_{n \to \infty} \frac{1}{d_n} \sum_{j=1}^{d_n} F(\sigma_j(A_n)) = \frac{1}{(2\pi)^d} \int_{[0,1]^d \times [-\pi,\pi]^d} F(|\kappa(\boldsymbol{x}, \boldsymbol{\theta})|) \, d\boldsymbol{x} \, d\boldsymbol{\theta},$$

*that is $\{A_n\}_n \sim_\sigma \kappa$. Furthermore, for a large enough $A_n$ and $\{\lambda_1(A_n), \ldots, \lambda_{d_n}(A_n)\}$ are the eigenvalues of $A_n$, then $\forall F \in \mathcal{C}_c(\mathbb{C}, \mathbb{C})$, we have*

$$\lim_{n \to \infty} \frac{1}{d_n} \sum_{j=1}^{d_n} F(\lambda_j(A_n)) = \frac{1}{(2\pi)^d} \int_{[0,1]^d \times [-\pi,\pi]^d} F(|\kappa(\boldsymbol{x}, \boldsymbol{\theta})|) \, d\boldsymbol{x} \, d\boldsymbol{\theta},$$

*that is $\{A_n\}_n \sim_\lambda \kappa$: finally the latter relation holds under the relaxed assumption that $A_n - A_n^*$ is 'small enough' (see Theorem 3.4 in [35]).*

2. *Any sequence of Toeplitz matrices $\{T_n(f)\}_n$ generated by a function $f \in L^1([-\pi,\pi]^d)$ is a GLT sequence of symbol $\kappa(\boldsymbol{x}, \boldsymbol{\theta}) = f(\boldsymbol{\theta})$.*

3. *Any sequence of diagonal sampling matrices $\{D_n(a)\}_n$ containing the evaluations of a Riemann-integrable function $a : [0,1]^d \to \mathbb{C}$ over a uniform grid is a GLT sequence with symbol $\kappa(\boldsymbol{x}, \boldsymbol{\theta}) = a(\boldsymbol{x})$.*

4. *If $\{A_n\}_n \sim_{\text{GLT}} \kappa$ then $\{A_n^*\}_n \sim_{\text{GLT}} \bar{\kappa}$.*

5. *For any $\alpha, \beta \in \mathbb{C}$ and*

$$\begin{cases} \{A_n\}_n \sim_{\mathrm{GLT}} \kappa_a \\ \{B_n\}_n \sim_{\mathrm{GLT}} \kappa_b \\ \{C_n\}_n \sim_{\mathrm{GLT}} \kappa_c \\ \{D_n\}_n \sim_{\mathrm{GLT}} \kappa_d \end{cases}$$

*then $\{\alpha A_n C_n + \beta B_n D_n\}_n$ is a sequence of GLT matrices and*

$$\alpha A_n C_n + \beta B_n D_n \sim_{\mathrm{GLT}} \alpha \kappa_a \kappa_c + \beta \kappa_b \kappa_d$$

We give now the definition of Cardinal B-splines (Uniform B-splines), for which the coming sections will be reliant on:

**Definition 4.4** (Cardinal B-spline). A cardinal B-spline of zero degree, denoted by $\phi_0$, is the characteristic function over the interval $[0, 1)$, i.e.,

$$\phi_0(t) := \begin{cases} 1, & t \in [0, 1) \\ 0, & \text{otherwise} \end{cases} \tag{4.3.2}$$

A cardinal B-spline of degree $p$, $p \in \mathbb{N}$, denoted by $\phi_p$, is defined by convolution as

$$\phi_p(t) = (\phi_{p-1} * \phi_0)(t) = \int_{\mathbb{R}} \phi_{p-1}(t - s)\phi_0(s)\, ds. \tag{4.3.3}$$

A cardinal B-spline of degree $p$, $p \in \mathbb{N}$, has the following properties

1. Minimal support: the support of $\phi_p$ is $[0, p + 1]$

2. $\phi_p \in \mathcal{C}^{p-1}$

3. $\phi_p$ is a piecewise-polynomial of degree $p$ at each interval $[i, i+1], \forall i \in \{0, 1, \ldots, p\}$

4. $\forall t \in [0, p+1]$ and $p \geq 1$, we have

$$\frac{d\phi_p}{dt}(t) = \phi_{p-1}(t) - \phi_{p-1}(t - 1) \tag{4.3.4}$$

5. $\forall t \in [0, p+1]$ and $p \geq 1$, we have

$$\phi_p(t) = \frac{t}{p}\phi_{p-1}(t) + \frac{p + 1 - t}{p}\phi_{p-1}(t - 1) \tag{4.3.5}$$

6. Symmetry: $\phi_p$ is symmetric on the interval $[0, p+1]$, i.e.,

$$\phi_p(t) = \phi_p(p + 1 - t), \quad \forall t \in [0, p+1] \tag{4.3.6}$$

7. Inner product:

$$\int_{\mathbb{R}} \phi_p^{(r)}(t)\phi_q^{(s)}(t + k) \, dt = (-1)^r \phi_{p+q+1}^{(r+s)}(p + 1 + k) = (-1)^s \phi_{p+q+1}^{(r+s)}(q + 1 - k) \tag{4.3.7}$$

8. Scaled and Translated Cardinal B-splines: considering that $h\mathbb{Z}$ is a uniform grid of width $h$. The scaled and translated Cardinal B-spline of degree $p$ is defined by

$$\phi_{k,h,p}(x) := \phi_p\left(\frac{x}{h} - k\right) \tag{4.3.8}$$

9. The support of $\phi_{k,h,p}$ is $[k, k + p + 1]h$.

### 4.3.3   Finite Elements based on Uniform B-splines

In the context of the FE based on uniform B-splines of degree p, we often deal with the following: mass, advection and stiffness matrices

$$M_{i_1 j_1} = \int_{\mathbb{R}} \phi_{i_1,h,p}(x) \, \phi_{j_1,h,p}(x) \, dx \tag{4.3.9}$$

$$A_{i_1 j_1} = \int_{\mathbb{R}} \frac{d\phi_{i_1,h,p}}{dx}(x) \, \phi_{j_1,h,p}(x) \, dx \tag{4.3.10}$$

$$S_{i_1 j_1} = \int_{\mathbb{R}} \frac{d\phi_{i_1,h,p}}{dx}(x) \, \frac{d\phi_{j_1,h,p}}{dx}(x) \, dx \tag{4.3.11}$$

we assume periodic boundary conditions.

**Remark 4.3.1.** In this case, these matrices are (multilevel) circulant matrices, which is a special case of (multilevel) Toeplitz matrices.

Using (4.3.8), the mass matrix $M_{i_1 j_1}$ (4.3.9) writes:

$$M_{i_1 j_1} = \int_{\mathbb{R}} \phi_p(\frac{x}{h} - i_1) \, \phi_p(\frac{x}{h} - j_1) \, dx \tag{4.3.12}$$

Referring to the inner product property of cardinal B-splines (4.3.7), where in this case $t = \frac{x}{h} - i_1$ and $k = (i_1 - j_1)$, we end up with:

$$M_{i_1 j_1} = h\ \phi_{2p+1}(p + 1 - (i_1 - j_1)). \tag{4.3.13}$$

Using the same two properties and apply them to the advection and stiffness matrices, (4.3.10) and (4.3.11) respectively, we get:

$$A_{i_1 j_1} = -\frac{d\phi_{2p+1}}{dx}(p + 1 - (i_1 - j_1)) \tag{4.3.14}$$

$$S_{i_1 j_1} = -h^{-1}\frac{d^2\phi_{2p+1}}{dx^2}(p + 1 - (i_1 - j_1)) \tag{4.3.15}$$

For better clarity we omit from now on the mesh step $h$ from the definition of the scaled and translated cardinal B-spline. We also consider the matrices $M_f, A_f, S_f$ where the value at the $i_1^{th}$ line and $j_1^{th}$ column are given, respectively, by

$$(M_f)_{i_1 j_1} = \int_{\mathbb{R}} f(x)\ \phi_{i_1,p}(x)\ \phi_{j_1,p}(x)\ dx$$

$$(A_f)_{i_1 j_1} = \int_{\mathbb{R}} f(x)\ \frac{d\phi_{i_1,p}}{dx}(x)\ \phi_{j_1,p}(x)\ dx$$

$$(S_f)_{i_1 j_1} = \int_{\mathbb{R}} f(x)\ \frac{d\phi_{i_1,p}}{dx}(x)\ \frac{d\phi_{j_1,p}}{dx}(x)\ dx$$

Finally, thanks to the results in section (4.3.2), the following theorems on the symbols of the mass, advection and stiffness matrices holds:

**Theorem 4.5.** *We have $\{h^{-1}M\} \sim_{\mathrm{GLT}} \mathfrak{m}_p$, where the symbol $\mathfrak{m}_p$ is given by*

$$\mathfrak{m}_p(x, \theta) := \mathfrak{m}_p(\theta) = \phi_{2p+1}(p + 1) + 2\sum_{k=1}^{p} \phi_{2p+1}(p + 1 - k)\cos(k\theta) \tag{4.3.16}$$

**Theorem 4.6.** *We have $\{-iA\} \sim_{\mathrm{GLT}} \mathfrak{a}_p$, where the symbol $\mathfrak{a}_p$ is given by*

$$\mathfrak{a}_p(x, \theta) := \mathfrak{a}_p(\theta) = -2\sum_{k=1}^{p} \phi'_{2p+1}(p + 1 - k)\sin(k\theta) \tag{4.3.17}$$

**Theorem 4.7.** *We have $\{hS\} \sim_{\mathrm{GLT}} \mathfrak{s}_p$, where the symbol $\mathfrak{s}_p$ is given by*

$$\mathfrak{s}_p(x, \theta) := \mathfrak{s}_p(\theta) = -\phi''_{2p+1}(2p + 1) - 2\sum_{k=1}^{p} \phi''_{2p+1}(p + 1 - k)\cos(k\theta) \tag{4.3.18}$$

We provide a proof for Theorem (4.5), and following similar steps allows us to proof Theorem (4.6) and Theorem (4.7).

*Proof.* Applying Fourier transform to $h^{-1}M$ via formula (4.3.12):

$$\mathfrak{m}_p(\theta) = \sum_{k \in \mathbb{Z}} \left( \int_{\mathbb{R}} \phi_p(t)\phi_p(t-k)dt \right) e^{-ik\theta},$$

and applying the convolution relation (4.3.7), we get:

$$\mathfrak{m}_p(\theta) = \sum_{k \in \mathbb{Z}} \phi_{2p+1}(p+1-k)e^{-ik\theta}$$

$$\mathfrak{m}_p(\theta) = 2 \sum_{k=0}^{p} \phi_{2p+1}(p+1-k)\cos(k\theta)$$

$$\mathfrak{m}_p(\theta) = \phi_{p+1}(p+1) + 2 \sum_{k=1}^{p} \phi_{2p+1}(p+1-k)\cos(k\theta)$$

$\square$

### 4.3.4 GLT-based Preconditioner for Elliptic Partial Differential Equations

Let us consider the following elliptic problem:

$$\begin{cases} -\nabla \cdot (A\nabla u) + (\boldsymbol{v} - \boldsymbol{w}) \cdot \nabla u + cu = f, & \text{in } \Omega \subset \mathbb{R}^d, \\ u = 0, & \text{on } \partial\Omega, \end{cases} \quad (4.3.19)$$

where $A : \Omega \to \mathbb{R}^{d\times d}$ is a symmetric matrix of functions $a_{hk} \in L^\infty(\Omega)$, $\boldsymbol{w}, \boldsymbol{v} : \Omega \to \mathbb{R}^d$ are vectors of functions $w_k, v_k \in L^\infty(\Omega)$, respectively, $c \in L^\infty(\Omega)$, $f \in L^2(\Omega)$. The $\boldsymbol{w}$ contribution is taken in the weak form, while the $\boldsymbol{v}$ part is taken in the strong form. This leads to the following weak formulation: find $u \in H_0^1(\Omega)$ such that

$$\int_\Omega (A\nabla u \cdot \nabla\phi + (\boldsymbol{v} \cdot \nabla u)\phi + u\boldsymbol{w} \cdot \nabla\phi + (c + \nabla \cdot \boldsymbol{w})u\phi)\, d\Omega = \int_\Omega f\phi\, d\Omega,$$

$$\forall \phi \in H_0^1(\Omega). \quad (4.3.20)$$

Now, suppose the physical domain $\Omega$ to be the unit hypercube $[0,1]^d$. For any pair of $d$-indexes $\boldsymbol{n} = (n_1, n_2, \ldots, n_d)$ and $\boldsymbol{p} = (p_1, p_2, \ldots, p_d)$ let us define the tensor

product B-splines as follows

$$\phi_{\boldsymbol{i},\boldsymbol{p}} : [0,1]^d \to \mathbb{R}, \quad \phi_{\boldsymbol{i},\boldsymbol{p}}(\boldsymbol{\theta}) = \prod_{j=1}^{d} \phi_{i_j,p_j}(\theta_j), \quad \boldsymbol{i} = 1, \ldots, \boldsymbol{n} + \boldsymbol{p}.$$

In the Isogeometric Galerkin approach we search for an approximation $u_{\mathcal{W}}$ of $u$ in the space $\mathcal{W} = \{\phi_{\boldsymbol{i+1},\boldsymbol{p}}\}_{i=1}^{n+p-2}$. Let

$$\mathcal{M}_{\boldsymbol{n}}^{[\boldsymbol{p}]} \boldsymbol{u} = \mathbf{b} \tag{4.3.21}$$

be the linear system resulting from this choice, where

$$\mathcal{M}_{\boldsymbol{n}}^{[\boldsymbol{p}]} = S_{\boldsymbol{n}}^{[\boldsymbol{p}]} + A_{\boldsymbol{n}}^{[\boldsymbol{p}]} + M_{\boldsymbol{n}}^{[\boldsymbol{p}]},$$

with

$$S_{\boldsymbol{n}}^{[\boldsymbol{p}]} = \left[ \int_{\Omega} A \nabla \phi_{\boldsymbol{j+1},\boldsymbol{p}} \cdot \nabla \phi_{\boldsymbol{i+1},\boldsymbol{p}} \ d\Omega \right]_{i,j=1}^{n+p-2},$$

$$A_{\boldsymbol{n}}^{[\boldsymbol{p}]} = \left[ \int_{\Omega} \left( \boldsymbol{v} \cdot \nabla \phi_{\boldsymbol{j+1},\boldsymbol{p}} \right) \phi_{\boldsymbol{i+1},\boldsymbol{p}} + \phi_{\boldsymbol{j+1},\boldsymbol{p}} \boldsymbol{w} \cdot \nabla \phi_{\boldsymbol{i+1},\boldsymbol{p}} \ d\Omega \right]_{i,j=1}^{n+p-2},$$

$$M_{\boldsymbol{n}}^{[\boldsymbol{p}]} = \left[ \int_{\Omega} (c + \nabla \cdot \boldsymbol{w}) \phi_{\boldsymbol{j+1},\boldsymbol{p}} \phi_{\boldsymbol{i+1},\boldsymbol{p}} \ d\Omega \right]_{i,j=1}^{n+p-2},$$

while $\boldsymbol{u}$ is the vector whose components are the coefficients of $u_{\mathcal{W}}$ with respect to the B-spline tensor basis generating $\mathcal{W}$, and

$$\mathbf{b} = \left[ \int_{\Omega} f \phi_{\boldsymbol{i+1},\boldsymbol{p}} \ d\Omega \right]_{i=1}^{n+p-2}.$$

In the following we recall some known results (see [32] for more details) concerning the spectral distribution of the matrices involved in the definition of the coefficient matrix $\mathcal{M}_{\boldsymbol{n}}^{[\boldsymbol{p}]}$. For the sake of simplicity, from now onward, we fix $\boldsymbol{n} = \boldsymbol{\mu} n$, $\boldsymbol{\mu} = (\mu_1, \ldots, \mu_d) \in \mathbb{Q}^d$, $n \in \mathbb{N}$ and define $N(\boldsymbol{\mu}) = \prod_{i=1}^{d} \mu_i$. Moreover, let us introduce the multivariate function $\mathfrak{m}_{\boldsymbol{p}}$, defined as

$$\mathfrak{m}_{\boldsymbol{p}}(\boldsymbol{\theta}) := \prod_{i=1}^{d} \mathfrak{m}_{p_i}(\theta_i),$$

and the following operators

$$\delta_{\boldsymbol{p}}^i(\boldsymbol{\theta}) := \mathfrak{a}_{p_i}(\theta_i) \prod_{\substack{j=1, \\ j \neq i}}^{d} \mathfrak{m}_{p_j}(\theta_j),$$

where $\mathfrak{m}_p(\theta)$, $\mathfrak{a}_p(\theta)$ are defined as in (4.3.16)–(4.3.17). We also introduce the following vector operator:

$$\boldsymbol{\delta_p}(\boldsymbol{\theta}) = \begin{pmatrix} \delta_{\boldsymbol{p}}^1(\boldsymbol{\theta}) \\ \vdots \\ \delta_{\boldsymbol{p}}^d(\boldsymbol{\theta}) \end{pmatrix},$$

and the following symmetric matrix $H_{\boldsymbol{p}} : [0,1]^d \to \mathbb{R}^{d \times d}$ of continuous functions defined by

$$(H_{\boldsymbol{p}}(\boldsymbol{\theta}))_{lk} = \begin{cases} \mathfrak{s}_{p_k}(\theta_k) \prod_{\substack{j=1 \\ j \neq k}}^{d} \mathfrak{m}_{p_j}(\theta_j), & l = k, \\ \mathfrak{a}_{p_l}(\theta_l) \mathfrak{a}_{p_k}(\theta_k) \prod_{\substack{j=1 \\ j \neq l,k}}^{d} \mathfrak{m}_{p_j}(\theta_j), & 1 \leq l < k \leq d \text{ or } 1 \leq k < l \leq d, \end{cases}$$

where $\mathfrak{s}_p(\theta)$ is defined as in (4.3.18).

**Theorem 4.8.** *The following distribution results hold*

$$\left\{ n^{d-2} S_{\boldsymbol{n}}^{[\boldsymbol{p}]} \right\}_n \sim_{\mathrm{GLT},\sigma,\lambda} \frac{1}{N(\boldsymbol{\mu})} \boldsymbol{\mu} \left( A(\boldsymbol{x}) \circ H_{\boldsymbol{p}}(\boldsymbol{\theta}) \right) \boldsymbol{\mu}^T,$$

$$\left\{ -i n^{d-1} A_{\boldsymbol{n}}^{[\boldsymbol{p}]} \right\}_n \sim_{\mathrm{GLT},\sigma,\lambda} \frac{1}{N(\boldsymbol{\mu})} \boldsymbol{\mu} \left( (\boldsymbol{v} - \boldsymbol{w})(\boldsymbol{x}) \circ \boldsymbol{\delta_p}(\boldsymbol{\theta}) \right),$$

$$\left\{ n^d M_{\boldsymbol{n}}^{[\boldsymbol{p}]} \right\}_n \sim_{\mathrm{GLT},\sigma,\lambda} \frac{1}{N(\boldsymbol{\mu})} (c + \nabla \cdot \boldsymbol{w}(\boldsymbol{x})) \mathfrak{m}_{\boldsymbol{p}}(\boldsymbol{\theta}),$$

*where $\circ$ denotes the component wise Hadamard (matrix or vector) product.*

Therefore, the asymptotic spectral behaviour of the coefficient matrix-sequence $\left\{ n^{d-2} \mathcal{M}_{\boldsymbol{n}}^{[\boldsymbol{p}]} \right\}_n$ is described both in terms of singular values and eigenvalues by the following function

$$\kappa^{[\boldsymbol{p}]}(\boldsymbol{x}, \boldsymbol{\theta}) = \frac{1}{N(\boldsymbol{\mu})} \boldsymbol{\mu} \left( A(\boldsymbol{x}) \circ H_{\boldsymbol{p}}(\boldsymbol{\theta}) \right) \boldsymbol{\mu}^T.$$

Furthermore, for each fixed $\boldsymbol{n} = \boldsymbol{\mu}n$ we have

$$
\begin{aligned}
\kappa_{\boldsymbol{n}}^{[\boldsymbol{p}]}(\boldsymbol{x}, \boldsymbol{\theta}) = \frac{1}{N(\boldsymbol{\mu})} &\left\{ \boldsymbol{\mu} \left( A(\boldsymbol{x}) \circ H_{\boldsymbol{p}}(\boldsymbol{\theta}) \right) \boldsymbol{\mu}^T + \frac{i}{n} \boldsymbol{\mu} \left( (\boldsymbol{v} - \boldsymbol{w})(\boldsymbol{x}) \circ \boldsymbol{\delta_p}(\boldsymbol{\theta}) \right) \right. \\
&+ \frac{1}{n^2} \left( c + \nabla \cdot \boldsymbol{w}(\boldsymbol{x}) \right) \mathfrak{m}_{\boldsymbol{p}}(\boldsymbol{\theta}).
\end{aligned}
\tag{4.3.22}
$$

Note that the problem (4.3.19) can be reformulated as follows

$$
\begin{cases}
-e^T (A \circ Hu)e + \boldsymbol{\eta} \cdot \nabla u + cu = f, & \text{in } \Omega \subset \mathbb{R}^d, \\
u = 0, & \text{on } \Omega,
\end{cases}
\tag{4.3.23}
$$

where $\boldsymbol{\eta}$ is such that $\eta_j = v_j - w_j - \sum_{i=1}^d \frac{\partial a_{ij}}{\partial x_i}$ and $\boldsymbol{e}^T = (1, ..., 1) \in \mathbb{R}^d$, while $Hu$ denotes the Hessian of $u$, i.e.,

$$
(Hu)_{ij} = \frac{\partial^2 u}{\partial x_i \partial x_j}.
$$

Starting from equation (4.3.23) and comparing it with (4.3.22), one can now understand the link between operator $\boldsymbol{\delta_p}(\boldsymbol{\theta})$ and the gradient, as well as the link between the matrix $H_{\boldsymbol{p}}(\boldsymbol{\theta})$ and the Hessian matrix.

## 4.3.5 Construction of the Preconditioner

In this subsection we recall the preconditioning strategy proposed in [27] for solving the linear system (4.3.21). To be precise, what is addressed is the normalized linear system

$$
n^{d-2} \mathcal{M}_{\boldsymbol{n}}^{[\boldsymbol{p}]} \boldsymbol{u} = n^{d-2} \mathbf{b}.
$$

The main steps of the above mentioned technique can be summarized in the following algorithm.

---

ALGORITHM 1: Preconditioning strategy for solving $n^{d-2}\mathcal{M}_{\boldsymbol{n}}^{[\boldsymbol{p}]}\boldsymbol{u} = n^{d-2}\mathbf{b}$

Step 1.     - if $\boldsymbol{v} - \boldsymbol{w} \neq \boldsymbol{0}$ (i.e., in the case $n^{d-2}\mathcal{M}_{\boldsymbol{n}}^{[\boldsymbol{p}]}$ is nonsymmetric), use as external solver: a Preconditioned Generalized Minimum Residual (PGMRES) whose preconditioner is given by $n^{d-2}\mathcal{M}_{\boldsymbol{n}}^{[\boldsymbol{p}]}$;

     - if $\boldsymbol{v} - \boldsymbol{w} = \boldsymbol{0}$ (i.e., in the case $n^{d-2}\mathcal{M}_{\boldsymbol{n}}^{[\boldsymbol{p}]}$ is symmetric), use as external solver: a Preconditioned Conjugate Gradient (PCG) with the same preconditioner as in previous item;

Step 2. solve the linear system associated with the preconditioner derived for the matrix $n^{d-2}\mathcal{M}_{\boldsymbol{n}}^{[\boldsymbol{p}]}$ by means of multigrid method consisting of:

   2.1 a V-cycle with standard linear interpolation prolongation operator at each level,

   2.2 a few post-smoothing iterations of a PCG at the finest level whose preconditioner is chosen as the multilevel Toeplitz matrix generated by $\mathfrak{m}_{\boldsymbol{p-1}}(\boldsymbol{\theta})$, and one Gauss-Seidel post-smoothing iteration at the other levels.

---

Note that, in the multigrid literature, a smoother is a stationary iterative solver[1], while PCG is a nonstationary iterative method (Krylov type solver), then the multigrid at Step 2. is not a multigrid in the classical sense (properly speaking, it is a multi-iterative solver [27]; see below for details).

Let us assume that $A(x) \equiv I$, $\boldsymbol{v} - \boldsymbol{w} = \boldsymbol{0}$, and $c = 0$. The steps of Algorithm 1 are strongly guided by the knowledge of the symbol, $\ell^{[\boldsymbol{p}]}$, of the matrix-sequence $\left\{ n^{d-2}\mathcal{M}_{\boldsymbol{n}}^{[\boldsymbol{p}]} \right\}_n$ given by

$$\ell^{[\boldsymbol{p}]}(\boldsymbol{\theta}) = \frac{1}{N(\boldsymbol{\mu})}\boldsymbol{\mu}\left(I \circ H_{\boldsymbol{p}}(\boldsymbol{\theta})\right)\boldsymbol{\mu}^T = \frac{1}{N(\boldsymbol{\mu})}\sum_{k=1}^{d}\mu_k^2 \mathfrak{s}_{p_k}(\theta_k)\prod_{\substack{j=1 \\ j \neq k}}^{d}\mathfrak{m}_{p_j}(\theta_j).$$

Without going into too much detail, we only recall the following two properties of $\ell^{[\boldsymbol{p}]}$ which have played a fundamental role in designing the optimal and robust strategy studied in [27] and which are then crucial for describing it accurately:

---

[1]A stationary iterative solver is solver for a linear system with an operator approximating the original problem and is based on a measurement of the error in the result (i.e, the residual), for which this process is repeated.

(*i*) $\ell^{[p]}$ has an analytic zero in $\boldsymbol{\theta} = \mathbf{0}$ of order 2 and possesses infinitely many numerical exponential zeros at the points $\boldsymbol{\theta}$ with $\theta_j = \pi$ when one of the $p_j$ becomes large;

(*ii*) because $\mathfrak{s}_p(\theta) = \mathfrak{m}_{p-1}(\theta)(2 - 2\cos(\theta))$ (see [26]), then $\ell^{[p]}$ can be rewritten as follows

$$\ell^{[\boldsymbol{p}]}(\boldsymbol{\theta}) = \frac{1}{N(\boldsymbol{\mu})}\mathfrak{m}_{\boldsymbol{p-1}}(\boldsymbol{\theta})\left[\sum_{k=1}^{d}\mu_k^2(2 - 2\cos(\theta_k))\prod_{\substack{j=1 \\ j \neq k}}^{d}\mathfrak{w}_{p_j}(\theta_j)\right],$$

where $\mathfrak{w}_p(\theta) = \frac{\mathfrak{m}_p(\theta)}{\mathfrak{m}_{p-1}(\theta)}$ is a function well-separated form zero, uniformly with respect to $\theta \in [0, \pi]$ and with respect to $p \geq 1$.

Property (*i*) implies the small eigenvalues of $n^{d-2}\mathcal{L}_n^{[\boldsymbol{p}]}$ to be related both with subspaces of low and high frequencies and then justifies the use at Step 2. of a so called *multi-iterative method* (see [27]), that is a method made up of different basic iterative solvers having complementary spectral behaviour. In particular, as already highlighted at items 2.1 and 2.2 of Algorithm 1, the one proposed in [27] consists of a V-cycle which is able to cope with the standard ill-conditioning in the low frequencies combined with a PCG post-smoothing at the finest level whose preconditioner works in the subspace of high frequencies. Indeed, because of property (*ii*), $\mathfrak{m}_{\boldsymbol{p-1}}^{-1}(\boldsymbol{\theta})\ell^{[\boldsymbol{p}]}(\boldsymbol{\theta})$ has only an actual zero in $\boldsymbol{\theta} = \mathbf{0}$, then choosing as a preconditioner for the PCG the multilevel Toeplitz matrix generated by $\mathfrak{m}_{\boldsymbol{p-1}}(\boldsymbol{\theta})$ the error in the high frequencies will be reduced.

In order to better explain Step 2. of Algorithm 1, we build on the concepts introduced in section (4.2). We denote by $l$ the level number, where $0 < l < N$ and N is the maximum number of levels we decide to use. To define a multigrid the following ingredients are needed:

1. appropriate smoothers $\mathcal{S}_i$, $\tilde{\mathcal{S}}_i$, and the corresponding smoothing steps $s_i$, $\tilde{s}_i$ for every level $i = 0, \ldots, l - 1$;

2. restriction operators $R_{\boldsymbol{m},i} : \mathbb{R}^{N_i} \to \mathbb{R}^{N_{i+1}}$ and prolongation operators $P_{\boldsymbol{m},i} : \mathbb{R}^{N_{i+1}} \to \mathbb{R}^{N_i}$ to transfer a quantity between levels $i$ and $i+1$, $i = 0, \ldots, l-1$;

3. a hierarchy of matrices at the coarser level $A_{\boldsymbol{m},i} \in \mathbb{R}^{N_i \times N_i}$, $i = 1, \ldots, l$ ($A_{\boldsymbol{m},0} = A_{\boldsymbol{m}}$).

One iteration of a multigrid in the *V-cycle version* consists of the following steps:

- $s_i$ pre-smoothing steps are performed using $\mathcal{S}_i$;

- The current iteration is corrected using the coarser level, a process which is known as *coarse grid correction*. More precisely, the residual $r_i \in \mathbb{R}^{N_i}$ is computed and restricted to the coarse grid obtaining $r_{i+1}$, which is used to solve the error equation on the coarse grid

$$A_{\boldsymbol{m},i+1}e_{i+1} = r_{i+1},$$

  by a recursive application of the multigrid method. The error $e_{i+1}$ is interpolated back to obtain the finer level error $e_i$ which is used to update the current iteration. The iteration matrix of the coarse grid correction is

$$CGC_i = I_{N_i} - P_{\boldsymbol{m},i}A_{\boldsymbol{m},i+1}^{-1}R_{\boldsymbol{m},i}A_{\boldsymbol{m},i};$$

- The iterate is improved by $\tilde{s}_i$ steps performed using $\tilde{\mathcal{S}}_i$.

In the V-cycle multigrid performed at Step 2. of Algorithm 1 the following choices have been made

- $A_{\boldsymbol{m},0} = n^{d-2}\mathcal{L}_{\boldsymbol{n}}^{[\boldsymbol{p}]}$;

- Pre-smoothing is not present;

- $R_{\boldsymbol{m},i} = P_{\boldsymbol{m},i}^T$ and $A_{\boldsymbol{m},i+1} = P_{\boldsymbol{m},i}^T A_{\boldsymbol{m},i} P_{\boldsymbol{m},i}$ (*Galerkin approach*), where for any $\boldsymbol{m} = (m_1, \ldots, m_d) \in \mathbb{N}^d$ with odd components

$$P_{\boldsymbol{m},i} = P_{m_1^{(i)}} \otimes \cdots \otimes P_{m_d^{(i)}}$$

  with $m_j^{(i)} = \frac{m_j - 2^i + 1}{2^i}$, $j = 1, \ldots, d$, $i = 0, \ldots, l-1$, and

$$P_m = \frac{1}{2}\begin{bmatrix} 1 & & & & \\ 2 & & & & \\ 1 & 1 & & & \\ & 2 & & & \\ & 1 & & & \\ & & & \ddots & \\ & & 1 & 1 & \\ & & & 2 & \\ & & & 1 & \end{bmatrix}_{m \times \frac{m-1}{2}}.$$

The prolongation operator $P_m$ is known as *linear interpolation operator* and the tensor prolongation operator $P_{\boldsymbol{m},i}$ is referred to as *d-linear interpolation operator* (where $d$ is the dimension of the domain). In the following we set $\boldsymbol{m} = (\mu_1 n + p_1 - 2, \ldots, \mu_d n + p_d - 2)$ and denote $P_{\boldsymbol{m},i} = P_{\boldsymbol{n},i}^{[\boldsymbol{p}]}$.

- One post-smoothing iteration by the Gauss-Seidel method (if $i \geq 1$), or a few, say $\tilde{s}$, iterations by the PCG with the preconditioner defined as the multilevel Toeplitz generated by $\mathfrak{m}_{\boldsymbol{p}-1}(\boldsymbol{\theta})$ (if $i = 0$).

The remaining part of this subsection is devoted to the construction of the multi-level Toeplitz preconditioner used at item 2.2 of Algorithm 1 and to the description of the strategy adopted for solving the associated linear system. Because of the properties of the Toeplitz matrices, the preconditioner generated by $\mathfrak{m}_{\boldsymbol{p}-1}(\boldsymbol{\theta})$ is given by

$$T_{\boldsymbol{n}}^{[\boldsymbol{p}]}(\mathfrak{m}_{\boldsymbol{p}-1}) = T_{\mu_1 n + p_1 - 2}(\mathfrak{m}_{p_1-1}) \otimes \cdots \otimes T_{\mu_d n + p_d - 2}(\mathfrak{m}_{p_d-1}). \qquad (4.3.24)$$

Such a preconditioner is easy to construct since we have that

$$(T_{\mu_k n + p_k - 2}(\mathfrak{m}_{p_k-1}))_{i,j} = \begin{cases} \phi_{2p_k-1}(p_k - i + j), & \text{if } |i - j| < p_k, \\ \\ 0, & \text{otherwise}, \end{cases}$$

i.e., its entries are nothing else than evaluations of cardinal B-splines. Moreover, due to its tensor product nature, the preconditioner (4.3.24) is easily solvable. For the sake of simplicity, let us fix $d = 2$. By the properties of Kronecker product

$$\left(T_{\boldsymbol{n}}^{[\boldsymbol{p}]}(\mathfrak{m}_{\boldsymbol{p}-1})\right)^{-1} = T_{\mu_1 n + p_1 - 2}^{-1}(\mathfrak{m}_{p_1-1}) \otimes T_{\mu_2 n + p_2 - 2}^{-1}(\mathfrak{m}_{p_2-1}).$$

If we denote by $\boldsymbol{y} = \text{vec}(Y)$ the vector obtained stacking the columns of the matrix $Y \in \mathbb{R}^{(\mu_1 n + p_1 - 2) \times (\mu_2 n + p_2 - 2)}$, the linear system

$$\left(T_{\boldsymbol{n}}^{[\boldsymbol{p}]}(\mathfrak{m}_{\boldsymbol{p}-1})\right)^{-1} \boldsymbol{x} = \boldsymbol{y}$$

can be solved by

$$\boldsymbol{x} = \text{vec}\left(T_{\mu_1 n + p_1 - 2}^{-1}(\mathfrak{m}_{p_1-1}) Y T_{\mu_2 n + p_2 - 2}^{-T}(\mathfrak{m}_{p_2-1})\right) \qquad (4.3.25)$$

which requires to solve $\mu_2 n + p_2 - 2$ linear systems with banded Toeplitz matrix $T_{\mu_1 n + p_1 - 2}(\mathfrak{m}_{p_1-1})$ plus $\mu_1 n + p_1 - 2$ linear systems with banded Toeplitz matrix

$T_{\mu_2 n + p_2 - 2}^T(\mathfrak{m}_{p_2-1})$. Each of these systems can be solved by means of an LU factorization which is optimal for banded matrices, i.e., linear in the matrix size (and quadratic in the bandwidth). Therefore, the computational cost for solving a linear system with coefficient matrix (4.3.24) is linear in the matrix size $\prod_{k=1}^d (\mu_k n + p_k - 2)$.

In the following flowchart (see Fig. (4.1)) we summarize the "recipe" for the multi-iterative solver proposed in [27].
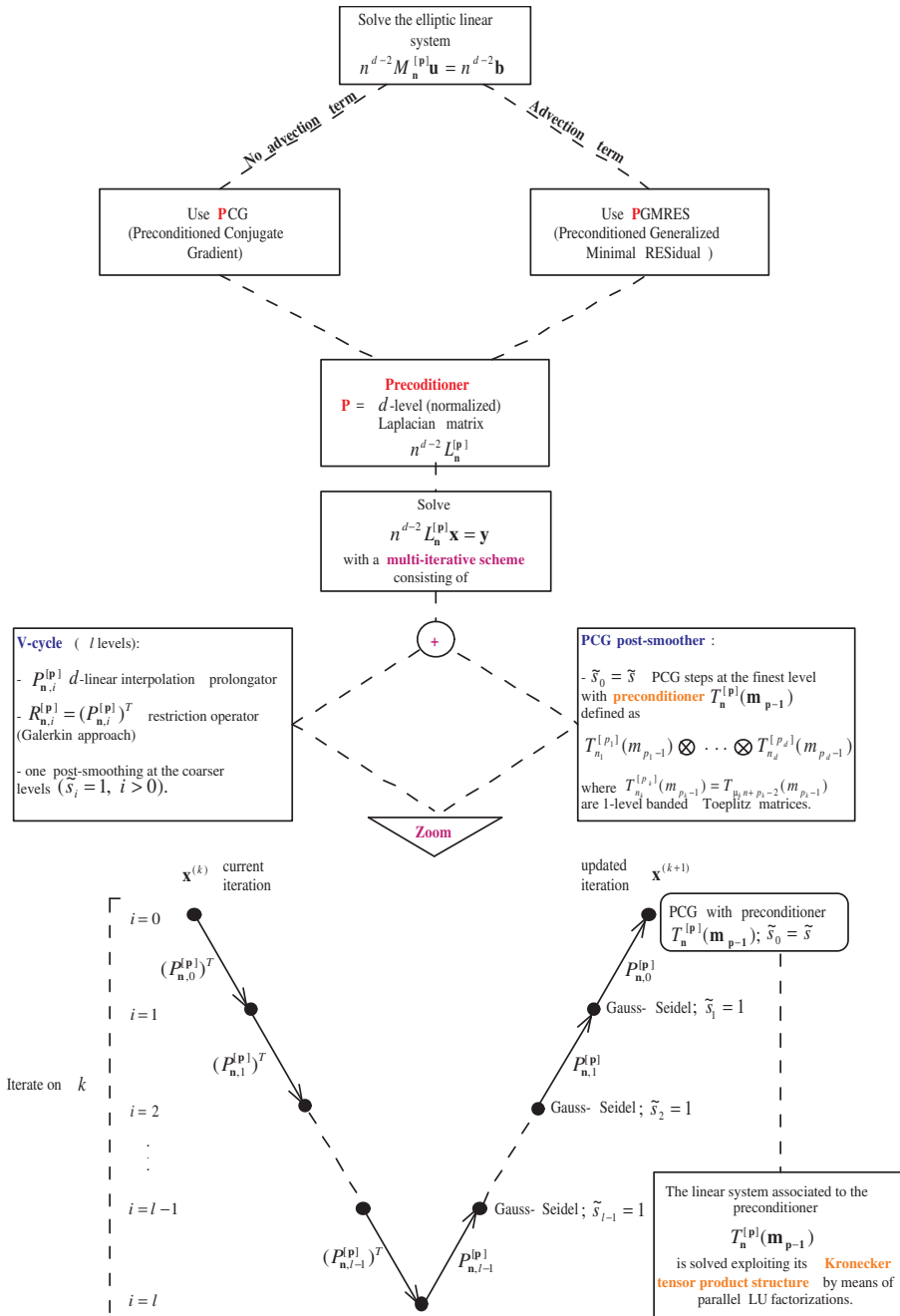


FIGURE 4.1: Flow chart explaining the steps needed to choose a solver and a preconditioner for an elliptic linear system. Courtesy of Dr. Mariarosa Mazza

## 4.4   Poisson's Equation

In order to benchmark our solver with the state of the art, we use the Poisson equation in $2D$ and on a square. Let $\Omega = [0,1] \times [0,1]$ denotes the computational domain. We consider the Poisson problem with dirichlet boundary condition. Let us consider Poisson's equation:

$$\begin{cases} -\nabla \cdot (\nabla u) = f, & \text{in } \Omega, \\ u = 0, & \text{on } \Omega, \end{cases} \tag{4.4.26}$$

multiplying Eq. (4.4.26) with a test function $\phi \in H_0^1(\Omega)$, the weak formulation reads: find $u \in H_0^1(\Omega)$ such that

$$\int_\Omega \nabla u \cdot \nabla \phi \, d\Omega = \int_\Omega f\phi \, \Omega, \quad \forall \phi \in H_0^1(\Omega). \tag{4.4.27}$$

Looking at the general form introduced in (4.3.19) and using the general algorithm that can be seen in Fig. (4.1). We aim to precondition our MG solver with the toeplitz matrix $T_n(m_{p-1})$ and exploit the Kronecker product for the inversion. Where the symbol $m_p$ is given by:

$$\mathfrak{m}_p(x,\theta) := \mathfrak{m}_p(\theta) = \phi_{2p+1}(p+1) + 2\sum_{k=1}^{p} \phi_{2p+1}(p+1-k)\cos(k\theta),$$

and $\phi_q(x)$ is the cardinal B-spline.

We present in Fig. (4.3b) the results obtained from solving Poisson's equation in 2D on a square $[0,1] \times [0,1]$. The figure demonstrates that using the MG solver solely without the ad-hoc GLT preconditioner requires more cycles in order to achieve the desired tolerance in comparison to using MG + GLT. We can also see that the difference between the two becomes more and more apparent, as we increase the degree of the B-spline. This could lead to the question, if using a GLT preconditioner makes sense from a computational point of view, as the GLT machinery might be more expensive even for a smaller number of required cycles to achieve convergence. For that, we refer the reader to Table (4.1), where we compare the time required to reach convergence both with and without GLT as a preconditioner for different B-spline degrees, where we can see that using MG + GLT is computationally cheaper than using MG as stand alone and even a lot cheaper comparatively for higher degree splines.
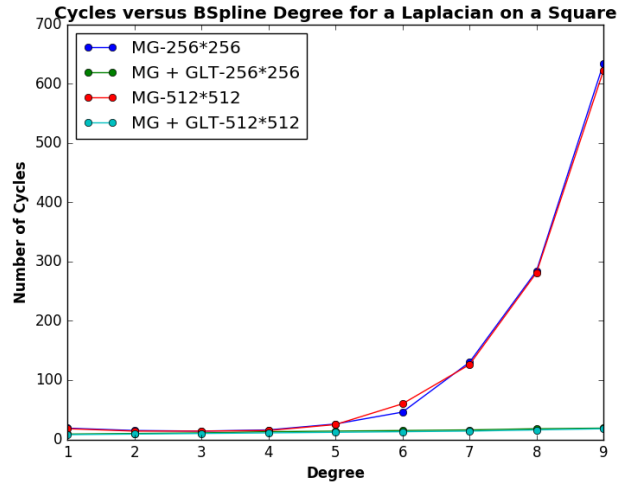
FIGURE 4.2: Required MG cycles till convergence with and without GLT as a preconditioner for Poisson on a square domain with 256 and 512 elements in each direction.

| Spline Degree | MG + GLT | MG |
|---|---|---|
| 1 | 1.32s | 1.76s |
| 2 | 2.56s | 2.75s |
| 3 | 2.58s | 4.42s |
| 4 | 3.42s | 21.62s |
| 5 | 6.35s | 170.48s |

TABLE 4.1: Time required to invert the Poisson equation using MG with and without GLT as a preconditioner with respect to the spline degree.

## 4.5   Anisotropic Diffusion

Now we propose to extend our study to a more challenging model: the anisotropic diffusion equation. We aim in this section to demonstrate the usage of the GLT theory as a tool to study the spectral distribution of different systems. The anisotropic diffusion problem is singular when the anisotropy of the diffusion tends to infinity. This singularity leads to an ill-posed problem and generates numerical issues like ill-conditioning and lack of accuracy. In this section, we are interested in the solution of the steady state anisotropic diffusion problem that writes

$$\nabla \cdot (\mathbf{K}\nabla u) = f, \quad \mathbf{x} \in \Omega, \tag{4.5.28}$$

where $\Omega$ is the domain, $u$ describes the temperature inside a Tokamak, the conductivity $\mathbf{K} = \kappa_\parallel \mathbf{K}_\parallel + \kappa_I \mathbf{I}$ is a 3 by 3 tensor. The later is a sum of two contributions,

the first component is the parallel component and is given by:

$$\kappa_\| \mathbf{K}_\| = \kappa_\| \frac{\mathbf{B}\mathbf{B^T}}{\|\boldsymbol{B}\|^2}. \tag{4.5.29}$$

In the case of Tokamak geometries, the prescribed magnetic field is of the form $\mathbf{B} = \nabla\varphi \times \nabla\psi + g\nabla\varphi$ (with $\varphi$ the toroidal angle), $\kappa_\|$ is a parallel diffusion coefficient. The second component $\kappa_I \mathbf{I}$ is a standard isotropic diffusion. We are interested in highly anisotropic configurations with $\frac{\kappa_\|}{\kappa_I} \simeq 10^6 \gg 1$.

Multiplying Eq. (4.5.28) by the basis function $\phi_i$ and integrating by parts leads to

$$\int_\Omega \frac{\kappa_\|}{\|\mathbf{B}\|^2}(\boldsymbol{B}\cdot\nabla u)(\boldsymbol{B}\cdot\nabla\phi_i) + \kappa_I \nabla u \cdot \nabla\phi_i d\Omega = \int_\Omega f\phi_i d\Omega. \tag{4.5.30}$$

Using the expansion $u = \sum_{j=1}^N u_j\phi_j$ with $N$ the total number of degrees of freedom, we get

$$\sum_{j=1}^N u_j \left( \int_\Omega \frac{\kappa_\|}{\|\mathbf{B}\|^2}(\boldsymbol{B}\cdot\nabla\phi_j)(\boldsymbol{B}\cdot\nabla\phi_i) + \kappa_I \nabla\phi_j \cdot \nabla\phi_i \right) d\Omega = \int_\Omega f\phi_i d\Omega, \tag{4.5.31}$$

which leads to the linear system $\mathcal{M}\mathbf{U} = \mathbf{F}$ where

$$\mathcal{M}_{ij} = \int_\Omega \frac{\kappa_\|}{\|\mathbf{B}\|^2}(\boldsymbol{B}\cdot\nabla\phi_j)(\boldsymbol{B}\cdot\nabla\phi_i) + \kappa_I \nabla\phi_j\cdot\nabla\phi_i d\Omega, \text{ and } F_i = \int_\Omega f\phi_i d\Omega, \quad \forall i,j \in [1,n]. \tag{4.5.32}$$

Let's define

$$\boldsymbol{B}(\mathbf{x}) = \begin{pmatrix} b^x(x,y) \\ b^y(x,y) \end{pmatrix} \tag{4.5.33}$$

and we consider the case where: $b^x(x,y) = b_1^x(x)b_2^x(y)$ and $b^y(x,y) = b_1^y(x)b_2^y(y)$. To simplify the notation, we will simply denote $b_1^x(x)$ by $b_1^x$, $b_1^y(x)$ by $b_1^y$, $b_2^x(y)$ by $b_2^x$ and $b_2^y(y)$ by $b_2^y$.

Taking that $\phi_i(x,y) = N_{i1}(x)N_{i2}(y)$, we expand $\boldsymbol{B}\cdot\nabla\phi_i$ and $\boldsymbol{B}\cdot\nabla\phi_j$:

$$\boldsymbol{B}\cdot\nabla\phi_i = (b_1^x N_{i1}') \cdot (b_2^x N_{i2}) + (b_1^y N_{i1}) \cdot (b_2^y N_{i2}') \tag{4.5.34}$$

$$\boldsymbol{B}\cdot\nabla\phi_j = (b_1^x N_{j1}') \cdot (b_2^x N_{j2}) + (b_1^y N_{j1}) \cdot (b_2^y N_{j2}') \tag{4.5.35}$$

Therefore,

$$(\boldsymbol{B} \cdot \nabla \phi_i)(\boldsymbol{B} \cdot \nabla \phi_j) = ((b_1^x)^2 N_{i1}' N_{j1}') \cdot ((b_2^x)^2 N_{i2}' N_{j2}') + ((b_1^x b_1^y) N_{i1}' N_{j1}) \cdot ((b_2^x b_2^y N_{i2} N_{j2}')$$

$$+ ((b_1^x b_1^y) N_{i1} N_{j1}') \cdot ((b_2^x b_2^y N_{i2}' N_{j2}) + ((b_1^y)^2 N_{i1} N_{j1}) \cdot ((b_2^y)^2 N_{i2}' N_{j2}')$$

$$(4.5.36)$$

Using the symbols of every $1D$ matrix, and the $*-$algebra structure of the GLT sequences, for the first term of Eq. (4.5.32), we get:

$$\int_\Omega \frac{\kappa_\|}{\|\mathbf{B}\|^2} (\boldsymbol{B} \cdot \nabla \phi_j)(\boldsymbol{B} \cdot \nabla \phi_i) \approx \frac{\kappa_\|}{\|\mathbf{B}\|^2} \{ (b_1^x)^2 (b_2^x)^2 \mathfrak{s}_p(\theta_1) \cdot \mathfrak{m}_p(\theta_2)$$

$$+ b_1^x b_1^y b_2^x b_2^y a_1^* \cdot a_2 + b_1^x b_1^y b_2^x b_2^y a_1 \cdot a_2^* + (b_1^y)^2 (b_2^y)^2 \mathfrak{m}_p(\theta_1) \cdot \mathfrak{s}_p(\theta_2) \}$$

$$(4.5.37)$$

$$\int_\Omega \frac{\kappa_\|}{\|\mathbf{B}\|^2} (\boldsymbol{B} \cdot \nabla \phi_j)(\boldsymbol{B} \cdot \nabla \phi_i) \approx \frac{\kappa_\|}{\|\mathbf{B}\|^2} \{ (b^x)^2 \mathfrak{s}_p(\theta_1) \cdot \mathfrak{m}_p(\theta_2) + (b^x b^y) \{ a_1^* \cdot a_2 + a_1 \cdot a_2^* \}$$

$$+ (b^y)^2 \mathfrak{m}_p(\theta_1) \mathfrak{s}_p(\theta_2) \}$$

$$(4.5.38)$$

where we used:

$$\int N_{i1}' N_{j1} = a_1^*, \quad \int N_{i1} N_{j1}' = a_1, \quad \int N_{i2}' N_{j2} = a_2^*, \quad \int N_{i1} N_{j1}' = a_2.$$

Since:

$$a_1 + a_1^* = 0, \quad a_2 + a_2^* = 0,$$

and assuming that $\|\boldsymbol{B}\| = 1$, we get:

$$\int_\Omega \frac{\kappa_\|}{\|\mathbf{B}\|^2} (\boldsymbol{B} \cdot \nabla \phi_j)(\boldsymbol{B} \cdot \nabla \phi_i) \approx \kappa_\| \{ (b^x)^2 \mathfrak{s}_p(\theta_1) \cdot \mathfrak{m}_p(\theta_2) - 2 b^x b^y a_1 \cdot a_2 + (b^y)^2 \mathfrak{m}_p(\theta_1) \cdot \mathfrak{s}_p(\theta_2) \}.$$

As for the second term of Eq. (4.5.32), we get:

$$\kappa_I \nabla \phi_j \cdot \nabla \phi_i d\Omega \approx \kappa_I \{ \mathfrak{s}_p(\theta_1) \mathfrak{m}_p(\theta_2) + \mathfrak{m}_p(\theta_1) \mathfrak{s}_p(\theta_2) \}.$$

We denote by $\mathfrak{L}$ the symbol of Eq. (4.5.28), and from the above analysis, it is given by:

$$\mathfrak{L} \sim_{\text{GLT}} \kappa_\| \{ (b^x)^2 \mathfrak{s}_p(\theta_1) \mathfrak{m}_p(\theta_2) - 2 b^x b^y \mathfrak{a}_p(\theta_1) \mathfrak{a}_p(\theta_2) + (b^y)^2 \mathfrak{m}_p(\theta_1) \mathfrak{s}_p(\theta_2) \}$$

$$+ \kappa_I \{ \mathfrak{s}_p(\theta_1) \mathfrak{m}_p(\theta_2) + \mathfrak{m}_p(\theta_1) \mathfrak{s}_p(\theta_2) \}.$$

$$(4.5.39)$$

### 4.5.1 The Bounds of the Symbol:

Finding the bounds of the symbol allows us to determine the range at which the eigenvalues are distributed, without having the need to evaluate the symbol for each eigenvalue. Starting from the symbol:

$$\mathfrak{L} \sim_{\mathrm{GLT}} \kappa_{||}\{(b^x)^2\mathfrak{s}_p(\theta_1)\mathfrak{m}_p(\theta_2) - 2b^xb^y\mathfrak{a}_p(\theta_1)\mathfrak{a}_p(\theta_2) + (b^y)^2\mathfrak{m}_p(\theta_1)\mathfrak{s}_p(\theta_2)\}$$
$$+\kappa_I\{\mathfrak{s}_p(\theta_1)\mathfrak{m}_p(\theta_2) + \mathfrak{m}_p(\theta_1)\mathfrak{s}_p(\theta_2)\}, \tag{4.5.40}$$

taking into account that: $\mathfrak{m}\mathfrak{s} \geq \mathfrak{a}^2$, it follows that then:

$$-\sqrt{\mathfrak{s}_1\mathfrak{m}_1} \leq \mathfrak{a}_1 \leq \sqrt{\mathfrak{s}_1\mathfrak{m}_1}$$

and

$$-\sqrt{\mathfrak{s}_2\mathfrak{m}_2} \leq \mathfrak{a}_2 \leq \sqrt{\mathfrak{s}_2\mathfrak{m}_2}.$$

So,

$$\mathfrak{L}_+ = (\kappa_{||}(b^x)^2\mathfrak{s}_p(\theta_1)\mathfrak{m}_p(\theta_2) + 2\kappa_{||}b^xb^y\sqrt{\mathfrak{s}_p(\theta_1)\mathfrak{m}_p(\theta_1)\mathfrak{s}_p(\theta_2)\mathfrak{m}_p(\theta_2)}$$
$$+\kappa_{||}(b^y)^2\mathfrak{m}_p(\theta_1)\mathfrak{s}_p(\theta_2)) + \kappa_I\{\mathfrak{s}_p(\theta_1)\mathfrak{m}_p(\theta_2) + \mathfrak{m}_p(\theta_1)\mathfrak{s}_p(\theta_2)\} \tag{4.5.41}$$

$$\mathfrak{L}_- = (\kappa_{||}(b^x)^2\mathfrak{s}_p(\theta_1)\mathfrak{m}_p(\theta_2) - 2\kappa_{||}b^xb^y\sqrt{\mathfrak{s}_p(\theta_1)\mathfrak{m}_p(\theta_1)\mathfrak{s}_p(\theta_2)\mathfrak{m}_p(\theta_2)}$$
$$+\kappa_{||}(b^y)^2\mathfrak{m}_p(\theta_1)\mathfrak{s}_p(\theta_2)) + \kappa_I\{\mathfrak{s}_p(\theta_1)\mathfrak{m}_p(\theta_2) + \mathfrak{m}_p(\theta_1)\mathfrak{s}_p(\theta_2)\} \tag{4.5.42}$$

$$\mathfrak{L}_+ = \kappa_{||}(b^x\sqrt{\mathfrak{s}_p(\theta_1)\mathfrak{m}_p(\theta_2)} + b^y\sqrt{\mathfrak{m}_p(\theta_1)\mathfrak{s}_p(\theta_2)})^2 + \kappa_I\{\mathfrak{s}_p(\theta_1)\mathfrak{m}_p(\theta_2) + \mathfrak{m}_p(\theta_1)\mathfrak{s}_p(\theta_2)\} \tag{4.5.43}$$

$$\mathfrak{L}_- = \kappa_{||}(b^x\sqrt{\mathfrak{s}_p(\theta_1)\mathfrak{m}_p(\theta_2)} - b^y\sqrt{\mathfrak{m}_p(\theta_1)\mathfrak{s}_p(\theta_2)})^2 + \kappa_I\{\mathfrak{s}_p(\theta_1)\mathfrak{m}_p(\theta_2) + \mathfrak{m}_p(\theta_1)\mathfrak{s}_p(\theta_2)\} \tag{4.5.44}$$

$\mathfrak{L}_+$ and $\mathfrak{L}_-$ are the upper and lower bounds of the symbol.

## 4.5.2 Finding the roots:

We derive in what follows, at which points the symbol evaluates to zero. Starting from the symbol:

$$\mathfrak{L} \sim_{\text{GLT}} \kappa_{||}\{(b^x)^2 \mathfrak{s}_p(\theta_1)\mathfrak{m}_p(\theta_2) - 2b^x b^y \mathfrak{a}_p(\theta_1)\mathfrak{a}_p(\theta_2) + (b^y)^2 \mathfrak{m}_p(\theta_1)\mathfrak{s}_p(\theta_2)\}$$
$$+\kappa_I\{\mathfrak{s}_p(\theta_1)\mathfrak{m}_p(\theta_2) + \mathfrak{m}_p(\theta_1)\mathfrak{s}_p(\theta_2)\} \tag{4.5.45}$$

Taking into account that: $\mathfrak{m}\mathfrak{s} \geq \mathfrak{a}^2$, then:

$$\mathfrak{L} \geq \kappa_{||}\{(b^x)^2 \mathfrak{s}_p(\theta_1)\mathfrak{m}_p(\theta_2) - 2b^x b^y \sqrt{\mathfrak{m}_p(\theta_1)\mathfrak{s}_p(\theta_1)}\sqrt{\mathfrak{m}_p(\theta_2)\mathfrak{s}_p(\theta_2)} + (b^y)^2 \mathfrak{m}_p(\theta_1)\mathfrak{s}_p(\theta_2)\}$$
$$+\kappa_I\{\mathfrak{s}_p(\theta_1)\mathfrak{m}_p(\theta_2) + \mathfrak{m}_p(\theta_1)\mathfrak{s}_p(\theta_2)\} \tag{4.5.46}$$

$$\mathfrak{L} \geq \{\kappa_{||}(b^x)^2 + \kappa_I\}\mathfrak{s}_p(\theta_1)\mathfrak{m}_p(\theta_2) - 2b^x b^y \sqrt{\mathfrak{m}_p(\theta_1)\mathfrak{s}_p(\theta_1)}\sqrt{\mathfrak{m}_p(\theta_2)\mathfrak{s}_p(\theta_2)}$$
$$+ \{\kappa_{||}(b^y)^2 + \kappa_I\}\mathfrak{m}_p(\theta_1)\mathfrak{s}_p(\theta_2). \tag{4.5.47}$$

Defining the following:

$$A = \{\kappa_{||}(b^x)^2 + \kappa_I\}, \quad B = -b_x b_y, \quad C = \{\kappa_{||}(b^y)^2 + \kappa_I\}, \quad \alpha = \frac{\mathfrak{s}_p(\theta_1)\mathfrak{m}_p(\theta_2)}{\mathfrak{m}_p(\theta_1)\mathfrak{s}_p(\theta_2)}.$$

Given that, we end up with:

$$\mathfrak{L} \geq \mathfrak{m}_p(\theta_1)\mathfrak{s}_p(\theta_2)(A\alpha^2 + B\alpha + C).$$

The roots of which are:
$$\alpha = \frac{-B \pm \sqrt{B^2 - 4AC}}{2A}.$$

This leads to:

$$\alpha_+ = \frac{2b_x b_y + \sqrt{4b_x^2 b_y^2 - (\kappa_{||}b_x^2 + \kappa_I)(\kappa_{||}b_y^2 + k_I)}}{2(k_{||}b_x^2 + k_I)}.$$

## 4.5.3 Spectral Distribution

In what follows, we present results that plots the spectral distribution obtained from using an eigenvalue solver directly applied to the anisotropic diffusion model and that was obtained from using the evaluation of the symbol. Fig. (4.3) shows the results obtained for different combinations of the parameters. For example, Fig. (4.3a) demonstrates the eigenvalues for the case of B-splines of degree 2,

with $b_x = 1, b_y = 0$, a ratio between the parallel diffusion coefficient and the perpendicular diffusion coefficient of 10, indicated as r = 10. The problem is solved on a 2D grid of 32 elements in each direction. We can see a good agreement between the results obtained via using the symbol and those of using directly the model. We note that the only bottleneck in terms of the effort needed is to do the analytical derivation of the associated symbol to the anisotropic diffusion (as done above) and this is to be done once, all the further results are obtained by direct evaluation of the derived symbol, which is very cheap on the computational level. Whereas to obtain the spectral distribution from the model, we need to invert a matrix every time to account for the different parameters of the system. The advantage of GLT is apparent in its cost efficiency.

(A) $p = 2, b_{x,y} = [1,0], r = 10$

(B) $p = 7, b_{x,y} = [1,0], r = 10$

(C) $p = 2, b_{x,y} = [1,0], r = 10^6$

(D) $p = 7, b_{x,y} = [1,0], r = 10^6$

(E) $p = 2, b_{x,y} = \frac{1}{\sqrt{2}}, r = 10^6$

(F) $p = 7, b_{x,y} = \frac{1}{\sqrt{2}}, r = 10^6$

(G) $p = 2, b_{x,y} = \frac{1}{\sqrt{2}}, r = 10$

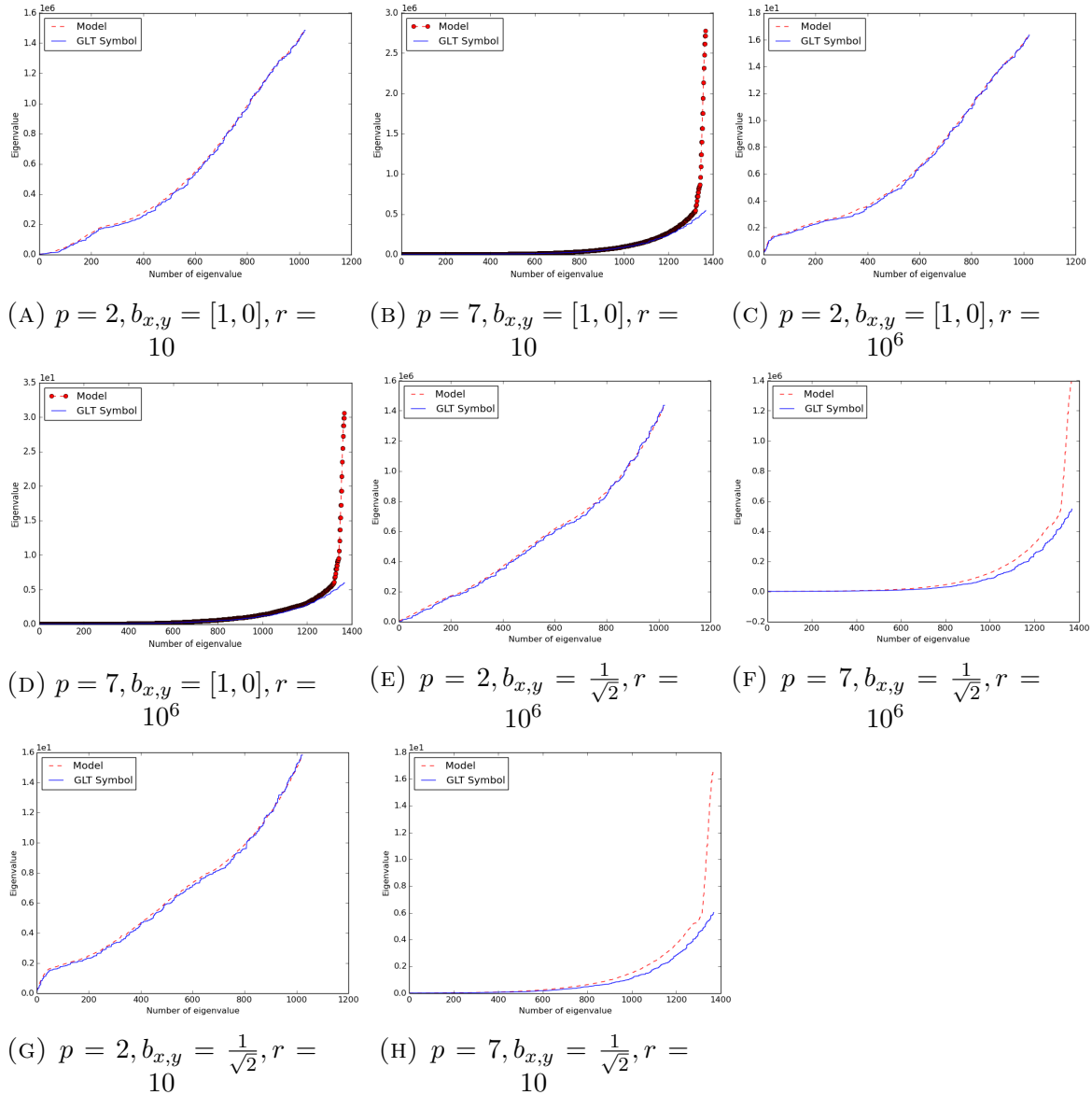(H) $p = 7, b_{x,y} = \frac{1}{\sqrt{2}}, r = 10$

FIGURE 4.3: Spectral distribution given different configurations for the anisotropic diffusion model comparing the results obtained due to using an eigenvalue solver on the model directly on the one hand and evaluating the symbol on the other. Both cases are evaluated on 2D Grid of 32 elements in each direction.

By further inspecting Fig. (4.3), we can notice that there are some eigenvalues that the GLT symbol does not manage to predict. It is to be noted that these outliers are identified according to [60] and it is expected that the number of outliers is infinitesimal in the size of the problem $(n^2)$. Table (4.2) shows that this is the case with regard to our numerical results.

| Grid | outliers | outliers/$n^2$ |
|------|----------|----------------|
| 16×16 | 16 | 0.0625 |
| 32×32 | 28 | 0.0273 |

TABLE 4.2: Number of outliers with respect to the grid size.

## 4.6 Code Development

The following has been developed in relation to this chapter:

- A MG solver prototype written in Python.

- A prototype for the GLT mass, advection and stiffness preconditioners written in Fortran.

## 4.7 Conclusions

In this chapter, we gave a general overview of the MG method and laid the foundations of the GLT theory and its usage as a preconditioner. We applied the MG solver with a GLT preconditioner for the Poisson equation and confirmed the gain obtained from using such an ad-hoc preconditioner that is able to tackle problem-specific pathologies. We ended the chapter with a study for the Anisotropic Diffusion problem and used the GLT as a spectral analysis tool, where we found that the GLT theory allows us to predict the spectral distribution of the Anisotropic Diffusion problem. The initial goal of the inclusion of the GLT study in this work was to use ad-hoc preconditioners for the various operators present in the linear MHD model. The involved coefficient matrices can have large condition numbers and hence standard iterative solvers perform badly. Unfortunately, we have only managed to reach a stage where we have implemented a GLT preconditioner for the Poisson problem. We refer the reader to [51] where an extensive study for 2D and 3D curl-div problems is carried out in the context of MHD models.

# Conclusions and Future Prospects

## Summary of the Work

In this work, we explored using compatible discretizations in the context of Isogeometric Analysis for the linear MHD model.

All the code development for the numerical simulations conducted in this work is implemented within the Jorek-Django framework, which is a FE library for nonlinear MHD that has been developed in the Max Planck Institute for Plasma Physics for the purpose of applying IgA techniques to solving PDEs numerically. The role of the author was to validate and verify the various implemented tools in the library while implementing a solver for the linear MHD model. The source code is hosted on two gitlabs: INRIA Sophia-Antipolis and MPCDF [2].

After the introduction of the numerical and mathematical tools that we rely on for the implementation of our models, we presented results related to the implementation of Maxwell's equations in 2D. We use the test case presented in [16][17] as a verification of the code machinery that we have built in our code implementation. This can be found in section (2.5.2), where we demonstrate the appropriate convergence rates using Issautier's 2D test case and present a comparison between the usage of commuting projection for the current density source term associated with Ampere's equation versus using the classical $L^2$ projection. The results confirm the previous findings in literature, that using the commuting projection leads to an exact preservation of the charge density. For this part, we have implemented the subroutines needed for the weak formulation in Jorek-Django, corrected the implementation of the discrete differential operators provided in the library, verified the implementation of the commuting projectors and coded Maxwell's equations in the Python package of Jorek-Django. The verification of the different developed tools within Jorek-Django for the implementation of Maxwell's equations laid the

---

[2]For the documentation, we refer the reader to http://jorek.gforge.inria.fr/install.html

foundations to move forward with the work and apply similar ideas to solve the linear MHD model.

In Chapter (3) we derived the linear MHD model with an appropriate scaling for Tokamaks in 2D and proposed a three way energy preserving splitting. The three steps that we proposed are what we call: the linear acoustic step, the linear magnetic step and the linear convection-diffusion step. This splitting has been done on the basis of the different scales present in the linear MHD model and aims at separating these different scales in order to reduce the complexity of solving the full system at once.

For each of the steps, we derived a spatial discretization which adheres to the associated de Rham sequence and ensures that the geometrical structures at the continuous level are being exactly mimicked at the discrete level as well. We then moved to supplementing the spatial discretization with a time discretization and run test cases to verify the derived numerical schemes. The following points have been implemented within the Jorek-Django Framework:

- The implementation of the different weak formulations in the finite element assemblers library of Jorek-Django in the form of subroutines written in Fortran.

- The implementation of the linking between the Python package and the Fortran finite element assemblers library using f2py[3].

- The implementation of the different models (the acoustic step, the magnetic step and the convection-diffusion step) and the relevant test cases in the Python package of Jorek-Django.

We ended Chapter (3) with two test cases relying on the suggested three-way splitting for the linear MHD model and implemented these test cases in Jorek-Django's Python package. We found that the solutions are convergent with the expected theoretical convergence order. All the while preserving the divergence of the magnetic field at the discrete level.

For all the test cases provided, the numerical solutions are convergent and verify the numerical schemes for the respective models. We have also shown that the energy is conserved in the case of the linear acoustic step and we found that the numerical vorticity is also preserved. For the linear magnetic step, we presented the preservation of the divergence-free condition for the provided test cases, but

---

[3]Fortran to Python interface generator.

we found that the energy is not conserved. This comes as no surprise, as we have used the $L^2$ projection for some terms in the numerical scheme rather than the derived commuting projection, due to the limitation of our code implementation. From a theoretical point of view, this indeed insures the preservation of the divergence-free condition, but not the energy conservation. The third and last step that we studied, is the linear convection-diffusion step, where we presented appropriate convergence rates with a test case neglecting the diffusion component of the velocity equation, due to the limitations imposed by the boundary conditions.

In Chapter (4) we quoted and elaborated on several newly developed concepts in the GLT theory drawing from literature on the field. We presented the results for using the GLT as a preconditioner for a MG solver in the case of Poisson's equation, and indeed established the numerical and computational advantages of using the GLT as a preconditioner. We ended the chapter with a spectral analysis done on the anisotropic diffusion problem using the GLT as a way to determine the associated eigenvalues of the system.

# Outlook

The results presented in this work establish promising steps towards using compatible discretizations for the linear MHD problem, where we preserved the divergence-free condition at the discrete level. That said, there is plenty of work to be done and room for numerous improvements. To start with, and one of the major limitations which are present in our implementation, is the inability of using commuting projections on the test functions, and rather using the classical $L^2$ projections. This leads to the break of symmetry between certain terms which was needed in order for the energy conservation condition to be held. Another major point is the constrains that we have imposed due to the unavailability of a functionality to impose boundary conditions on the test functions, and hence, we have resorted to using solutions which are vanishing on the boundaries to avoid this issue.

It is also worth noting that the GLT theory offers a valuable tool to study the spectral properties of the different operators and in turn finding ah-hoc preconditioners. The work provided is only related to preconditioning Poisson's equation. It would be interesting to apply the GLT preconditioner to the various operators present in the linear MHD system.

# Bibliography

[1] D. Arnold, R. Falk, and R. Winther. Finite element exterior calculus, homological techniques, and applications. *Acta Numerica*, pages 1–155, 2006.

[2] D. Arnold, R. Falk, and R. Winther. Finite element exterior calculus: From hodge theory to numerical stability. *Bulletin of the American Mathematical Society*, 2010.

[3] U. Ascher, S. Ruuth, and B. Wetton. Implicit-Explicit Methods for Time-Dependent Partial Differential Equations. *Society for Industrial and Applied Mathematics*, 32(3):797–823, 1995.

[4] F. Auricchio, L. da Veiga, A. Buffa, C. Lovadina, A. Reali, and G. Sangalli. A fully "locking-free" isogeometric approach for plane linear elasticity problems: A stream function formulation. *Computer Methods in Applied Mechanics and Engineering*, 2007.

[5] B. Balet, P. Stubberfield, D. Borba, M. Keilhacker, A. Gibson, and C. Gormezano. Fusion energy production from a deuterium-tritium plasma in the JET tokamak. Technical report, 1992.

[6] D. Balsara and J. Kim. A Comparison between Divergence Cleaning and Staggered Mesh Formulations for Numerical Magnetohydrodynamics. *The Astrophysical Journal*, 2004.

[7] T. Barker. Climate Change 2007: An Assessment of the Intergovernmental Panel on Climate Change. *Change*, 2007.

[8] L. Beirão da Veiga, A. Buffa, J. Rivas, and G. Sangalli. Some estimates for h-p-k-refinement in Isogeometric Analysis. *Numerische Mathematik*, 2011.

[9] H. Bijl, M. Carpenter, V. Vatsa, and C. Kennedy. Implicit Time Integration Schemes for the Unsteady Compressible Navier Stokes Equations: Laminar Flow. *Journal of Computational Physics*, 179(1):313–329, 6 2002.

[10] A. Bossavit. Discretization of Electromagnetic Problems: The "Generalized Finite Differences" Approach. *Handbook of Numerical Analysis*, 2005.

[11] J. Brackbill. Fluid modeling of magnetized plasmas. *Space Science Reviews*, 1985.

[12] J. Brackbill and D. C. Barnes. The effect of nonzero divergence condition on the numerical solution of the magnetohydrodynamic equations. *Journal of Computational Physics*, 1980.

[13] A. Buffa, J. Rivas, G. Sangalli, and R. Vázquez. Isogeometric Discrete Differential Forms in Three Dimensions. *SIAM Journal on Numerical Analysis*, 2011.

[14] A. Buffa, G. Sangalli, and R. Vázquez. Isogeometric analysis in electromagnetics: B-splines approximation. *Comput. Methods Appl. Mech. Engrg*, 2009.

[15] M. Campbell and R. Mccrory. Progress toward ignition and burn propagation in inertial confinement fusion. *Physics Today*, 1992.

[16] M. Campos Pinto and E. Sonnendrücker. Compatible Maxwell solvers with particles I : conforming and non-conforming 2D schemes with a strong Ampere law. *SMAI Journal of Computational Mathematics*, 3:53–89, 2017.

[17] M. Campos Pinto and E. Sonnendrücker. Compatible Maxwell solvers with particles II: conforming and non-conforming 2D schemes with a strong Faraday law. *SMAI Journal of Computational Mathematics*, Vol. 3:91–116, 2017.

[18] L. Chacón, D.A. Knoll, and J.M. Finn. An Implicit, Nonlinear Reduced Resistive MHD Solver. *Journal of Computational Physics*, 178(1):15–36, 5 2002.

[19] F. Chen. *Introduction to Plasma Physics and Controlled Fusion*. Springer International Publishing, Cham, 2016.

[20] O. Czarny and G. Huysmans. Bézier surfaces and finite elements for MHD simulations. *Journal of Computational Physics*, 2008.

[21] J.-P. Cioni D. Issautier, F. Poupaud and L. Fezoui. A 2-D Vlasov-Maxwell solver on unstructured meshes. *Third international conference on mathematical and numerical aspects of wave propagation*, pages 355–371, 1995.

[22] W. Dai and P. Woodward. On the Divergence Free Condition and Conservation Laws in Numerical Simulations for Supersonic Magnetohydrodynamical Flows. *The Astrophysical Journal*, 2002.

[23] A. Dedner, F. Kemm, D. Kröner, C. Munz, T. Schnitzer, and M. Wesenberg. Hyperbolic divergence cleaning for the MHD equations. *Journal of Computational Physics*, 2002.

[24] L. Demkowicz. Polynomial exact sequences and projection-based interpolation with application to maxwell equations. *Lecture Notes in Mathematics*, 2008.

[25] L. Demkowicz and A. Buffa. H1, H(curl) and H(div)-conforming projection-based interpolation in three dimensions Quasi-optimal p-interpolation estimates. *Computer Methods in Applied Mechanics and Engineering*, 194(2-5 SPEC. ISS.):267–296, 2005.

[26] M. Donatelli, C. Garoni, C. Manni, S. Serra-Capizzano, and H. Speleers. Robust and optimal multi-iterative techniques for IgA collocation linear systems. *Comput. Methods Appl. Mech. Engrg.*, 284:1120–1146, 2015.

[27] M. Donatelli, C. Garoni, C. Manni, S. Serra-Capizzano, and H. Speleers. Robust and optimal multi-iterative techniques for IgA Galerkin linear systems. *Comput. Methods Appl. Mech. Engrg.*, 284:230–264, 2015.

[28] J. Eastwood. The virtual particle electromagnetic particle-mesh method. *Computer Physics Communications*, 1991.

[29] C. Evans and J. Hawley. Simulation of magnetohydrodynamic flows - A constrained transport method. *The Astrophysical Journal*, 2002.

[30] J. Evans, Y. Bazilevs, I. Babuška, and T. Hughes. n-Widths, sup-infs, and optimality ratios for the k-version of the isogeometric finite element method. *Computer Methods in Applied Mechanics and Engineering*, 2009.

[31] E. Franck, M. Hölzl, A. Lessig, and E. Sonnendrücker. Energy conservation and numerical stability for the reduced MHD models of the non-linear JOREK code. Technical report, 2018.

[32] C. Garoni and S. Serra-Capizzano. Generalized Locally Toeplitz sequences: A spectral analysis tool for discretized differential equations. In *Lecture Notes in Mathematics*. 2018.

[33] V. Girault and Pa. Raviart. Finite element methods for Navier-Stokes equations: theory and algorithms. Technical report, 1986.

[34] J. P. Goedbloed, R. Keppens, and S. Poedts. *Advanced magnetohydrodynamics: With applications to laboratory and astrophysical plasmas.* 2010.

[35] L. Golinskii and S. Serra-Capizzano. The asymptotic properties of the spectrum of nonsymmetrically perturbed Jacobi matrix sequences. *Journal of Approximation Theory*, 2007.

[36] H. Gómez, V. Calo, Y. Bazilevs, and T. Hughes. Isogeometric analysis of the Cahn-Hilliard phase-field model. *Computer Methods in Applied Mechanics and Engineering*, 2008.

[37] H. Guillard. The mathematical theory of reduced MHD models for fusion plasmas. Technical report, 2015.

[38] J. Hesthaven and T. Warburton. Nodal High-Order Methods on Unstructured Grids. *Journal of Computational Physics*, 2002.

[39] R. Hiptmair. Canonical construction of finite elements. *Mathematics of Computation*, 1999.

[40] R. Hiptmair. Finite elements in computational electromagnetism. *Acta Numerica*, pages 237–339, 2002.

[41] R. Hiptmair. Maxwell's Equations: Continuous and Discrete. In *Computational Electromagnetism: Cetraro, Italy 2014*, pages 1–58. Springer International Publishing, Cham, 2015.

[42] R. Hiptmair and J. Xu. Nodal auxiliary space preconditioning in H(curl) and H(div) spaces. *SIAM Journal on Numerical Analysis*, 45(6):2483–2509, 2007.

[43] J. Holdren. Population and the Energy Problem. Technical report, 1991.

[44] Q. Huang, S. Hu, and R. Martin. Fast degree elevation and knot insertion for B-spline curves. *Computer Aided Geometric Design*, 22:183–197, 2005.

[45] International Atomic Energy Agency. ITER Documentation Series No. 21 ITER Physics. Technical report, Vienna, 1991.

[46] G. B. Jacobs and Jan S. Hesthaven. High-order nodal discontinuous Galerkin particle-in-cell method on unstructured grids. *Journal of Computational Physics*, 2006.

[47] N. Krishnamurthy. Finite element method. In *Advanced Topics in Science and Technology in China*. 2008.

[48] D. Lee and H. Choi. Magnetohydrodynamic turbulent flow in a channel at low magnetic Reynolds number. *J. Fluid Mech*, 439:367–394, 2019.

[49] O. Livne and A. Brandt. *Multigrid Techniques: 1984 Guide with Applications to Fluid Dynamics*. Classics in Applied Mathematics, revised edition, 2011.

[50] D. MacIsaac. Sustainable Energy without the Hot Air. *The Physics Teacher*, 2009.

[51] M. Mazza, C. Manni, A. Ratnani, S. Serra-Capizzano, and H. Speleers. Isogeometric analysis for 2D and 3D curl-div problems: Spectral symbols and fast iterative solvers. *Computer Methods in Applied Mechanics and Engineering*, 344:970–997, 2019.

[52] P. Monk. Analysis of a Finite Element Method for Maxwells Equations. *SIAM Journal on Numerical Analysis*, 2005.

[53] V. Mukhovatov, V. Shafranov, and La IV. Artsimovich Kurchatov. Tokamak devices. Technical report, 1972.

[54] J. Ongena, R. Koch, R. Wolf, and H. Zohm. Magnetic-confinement fusion. *Nature Physics*, 12, 2016.

[55] F. Orain, M. Bécoulet, J. Morales, G T A Huijsmans, G. Dif-Pradalier, M. Hoelzl, X. Garbet, S. Pamela, E. Nardon, C. Passeron, G. Latu, A. Fil, and P. Cahyna. Non-linear {MHD} modeling of edge localized mode cycles and mitigation by resonant magnetic perturbations. *Plasma Physics and Controlled Fusion*, 57(1):14020, 11 2014.

[56] A. Palha, P. Rebelo, R. Hiemstra, J. Kreeft, and M. Gerritsma. Physics-compatible discretization techniques on single and dual grids, with application to the Poisson equation of volume forms. *Journal of Computational Physics*, 257:1394–1422, 2004.

[57] A. Quarteroni, R. Sacco, and F. Saleri. *Numerical Mathematics*. Springer-Verlag Berlin Heidelberg, 2 edition, 2007.

[58] P. Roberts. *An Introduction to Magnetohydrodynamics*. LONGMANS, London, 1967.

[59] S. Depeyre and D. Issautier. A new constrained formulation of the Maxwell system. *Rairo- Mathematical Modelling and Numerical Analysis-Modelisation Mathematique Et Analyse Numerique*, 31(3):327357, 1997.

[60] S. Serra-Capizzano. Generalized locally Toeplitz sequences: Spectral analysis and applications to discretized partial differential equations. *Linear Algebra and Its Applications*, 2003.

[61] S. Serra-Capizzano. The GLT class as a generalized Fourier analysis and applications. *Linear Algebra and Its Applications*, 419:180–233, 2006.

[62] S. Smolentsev, S. Badia, R. Bhattacharyay, L. Bühler, L. Chen, Q. Huang, H.-G. Jin, D. Krasnov, D.-W. Lee, E. Mas de les Valls, C. Mistrangelo, R. Munipalli, M.-J. Ni, D. Pashkevich, A. Patel, G. Pulugundla, P. Satyamurthy, A. Snegirev, V. Sviridov, P. Swain, T. Zhou, and O. Zikanov. An approach to verification and validation of MHD codes for fusion applications. *Fusion Engineering and Design*, 100:65–72, 11 2015.

[63] L. Spitzer. The Stellarator Concept. *The Physics of Fluids*, 1:253, 1958.

[64] Stephen C. MHD Simulations for Fusion Applications. Technical report, 2010.

[65] L. Tiller and W. Piegl. *The NURBS book*. Springer-Verlag, Berlin, Heidelberg, second edition, 2013.

[66] P. Tilli. Locally Toeplitz sequences: Spectral properties and applications. *Linear Algebra and Its Applications*, 1998.

[67] G. Tóth. The Div B = 0 Constraint in Shock-Capturing Magnetohydrodynamics Codes. *Journal of Computational Physics*, 2000.

[68] J. Wesson, R. Gill, M. Hugon, M. Nave, and M. Turner. Transport, instability and disruptions in tokamaks. *Nucl. Fusion*, 22:1069, 1982.

[69] D. Yan, M. Pugh, and F. Dawson. Adaptive Time-stepping Schemes for the Solution of the Poisson-Nernst-Planck Equations. Technical report, 2019.